On the Balanced Response of the Troposphere to variability in the Extratropical Stratosphere

By
Jason C. Furtado

Department of Atmospheric Science
Colorado State University
Fort Collins, Colorado

Colorado State University

Department of Atmospheric Science

Paper No. 775

ON THE BALANCED RESPONSE OF THE TROPOSPHERE TO VARIABILITY IN THE EXTRATROPICAL STRATOSPHERE

Submitted by

Jason C. Furtado

Department of Atmospheric Science

In partial fulfillment of the requirements

For the Degree of Master of Science

Colorado State University

Fort Collins, Colorado

Summer 2005

ABSTRACT

ON THE BALANCED RESPONSE OF THE TROPOSPHERE TO VARIABILITY IN THE EXTRATROPICAL STRATOSPHERE

Variability in the extratropical stratosphere arises primarily through wave-mean flow interactions, with the source of these waves lying in the troposphere. However, recent evidence suggests that the troposphere also responds to variability in the extratropical stratosphere, with persistent anomalies in the stratospheric circulation accompanying same-signed anomalies at tropospheric levels. The balanced response of the atmosphere to anomalous stratospheric wave breaking and heating qualitatively describes how the troposphere should respond to stratospheric variability. However, the balanced response has been viewed as incapable of explaining the observed tropospheric anomalies because of the relative small mass of the stratosphere compared to the troposphere. Hence, studies have looked at tropospheric eddy feedbacks and internal tropospheric wave dynamics as ways to explain the amplitude of the observed tropospheric response.

This thesis demonstrates that the balanced response is, in fact, capable of explaining the amplitude of the observed tropospheric response to anomalous forcing in the stratosphere. First, we examine observations of stratosphere/troposphere dynamical coupling in two frameworks: the Eulerian mean (EM) and transformed Eulerian mean (TEM) frameworks. Each framework offers its own interpretation of the dynamics of the

coupled system, but only the TEM framework allows us to investigate stratosphere/troposphere dynamical coupling directly in terms of wave-mean flow interactions. The observational analyses suggest relationships between the observed changes in the stratosphere and troposphere and also which terms in the governing equations in each framework dominate the observed zonal-mean zonal wind and temperature fields.

Then, we use a simple numerical model to quantify the balanced response of the atmosphere to prescribed anomalous stratospheric wave drag, anomalous stratospheric radiative cooling, and friction. The results of the model demonstrate that the balanced response sufficiently accounts for the amplitude of the observed tropospheric response to stratospheric anomalies. Hence, tropospheric eddy feedbacks are not required to explain the observed anomalies, contrary to previous studies. Moreover, the results show that persistent positive temperature anomalies in the lower stratosphere contribute to the persistence of the attendant tropospheric zonal-mean zonal wind anomalies by countering the restoring effects of friction. The results suggest parameterizations of radiative cooling used in modeling experiments are important in capturing these persistent anomalies.

Jason C. Furtado
Department of Atmospheric Science
Colorado State University
Fort Collins, CO 80523
Summer 2005

TABLE OF CONTENTS

CHAPTER 1

INTRODUCTION AND BACKGROUND

The atmosphere is comprised of four layers defined on the basis of variations in the vertical thermal structure of the atmosphere. The troposphere, the lowermost layer, receives the most attention in the atmospheric literature simply because weather changes rapidly in this layer and impacts the daily lives of humans. The troposphere is characterized generally by decreasing temperature with height. 80-90% of the mass in the atmosphere resides in the troposphere. Above this layer lies the stratosphere, appropriately named because the layer includes a temperature inversion and thus is stably stratified. The temperature profile in the stratosphere is maintained mainly through a balance between radiative effects and dynamical heating (Andrews et al. 1987). The radiative heating of the stratosphere comes from the high amounts of ozone in the layer. Ozone absorbs ultraviolet radiation from the sun, heating the stratosphere and protecting the surface of Earth from this dangerous radiation. Above the stratosphere are the mesosphere, a region where temperature quickly decreases with height due to low ozone concentrations and hence less solar absorption, and the thermosphere, which has high temperatures but little mass.

The differences in composition and thermal properties of the troposphere and the stratosphere do not preclude the two layers from interacting with each other. Interactions between the two layers can involve actual transport of constituents between the two layers or dynamical interactions through wave breaking. Waves that cross into the stratosphere from the troposphere originate from a variety of sources – from gravity waves emitted atop convective towers in the tropics to topographically-forced quasi-stationary planetary waves to smaller scale baroclinic waves in the extratropical atmosphere. Upon breaking, these waves impose primarily a mechanical force on the stratospheric circulation and alter the circulation locally and remotely. Interactions like these just described are collectively covered under the subject of *stratosphere/troposphere dynamical coupling*.

This thesis examines the dynamics of stratosphere/troposphere dynamical coupling and a possible explanation for the observed and simulated behavior of the coupled system. This chapter offers introductory material on the theory of stratosphere/troposphere dynamical coupling and reviews previous studies on the topic. First we examine the theory of wave-mean flow interaction, the primary way the troposphere interacts with the stratosphere. Then, we present a brief climatology and a review of variability in the extratropical stratosphere. Next, previous works on stratosphere/troposphere dynamical coupling in both observations and modeling are discussed. We conclude the chapter with the objectives and the outline for the thesis.

1.1 Wave-Mean Flow Interaction: Theory

1.1.1 Vertically Propagating Waves and the Quasi-Geostrophic Index of Refraction

Despite the large number of wave energy sources in the troposphere, not all waves can vertically propagate and interact with the stratospheric flow. Properties of the surrounding atmosphere dictate whether waves may or may not propagate through the medium. This idea is similar to the propagation of electromagnetic waves, which requires an index of refraction to be positive definite in order for the waves to propagate. We can derive a similar criterion for vertically propagating Rossby waves (VPWs) in the terrestrial atmosphere. A convenient form of the quasi-geostrophic (QG) index of refraction (n^2) for atmospheric waves is

$$n^2 = \frac{N^2}{f_o^2}\left[\frac{\beta}{\bar{u}-c} - k^2\right] - \frac{1}{4H^2}, \tag{1.1}$$

where N^2 is the square of the Brunt-Väisällä frequency, f_o is a constant value of the Coriolis parameter (usually $\sim 10^{-4}\ s^{-1}$ in QG theory), $\beta \equiv \frac{df}{dy}$, c is the phase speed of the wave, k is the zonal wavenumber, and H is the scale height. (1.1) is nearly identical to the form of n^2 derived in Holton (1992) except here we neglect meridional wavenumbers.

From (1.1), $n^2 > 0$ when

$$0 < \bar{u} - c < \beta\left[k^2 + \frac{f_o^2}{4N^2H^2}\right]^{-1} \equiv U_c \tag{1.2}$$

for real c. The term on the far right hand side (RHS) of (1.2) is the upper limit of the velocity of the ambient flow through which atmospheric waves can propagate. This velocity is referred to as the *critical Rossby velocity* (U_c).

From (1.2), two basic criteria are set for VPWs:

- The zonal-mean zonal flow must be westerly, but the flow (minus the phase speed of the wave) cannot exceed U_c; and
- Long waves (waves with small k) are more likely to propagate in westerlies than short waves (waves with large k). This conclusion arises because of the inverse relation between k and U_c.

In an influential paper on wave-mean flow interactions, Charney and Drazin (1961) examined n^2 in the context of waves interacting with the stratospheric flow. Figure 1.1 illustrates the variation of n^2 with height, averaged 30°-60°N, for the Northern Hemisphere (NH) summer and winter months and for 3 different wavelengths. In the winter months, the longest waves (the solid line in Fig. 1.1) exhibit $n^2 > 0$ throughout most of the troposphere and the middle stratosphere (~ 30 km), while the shortest waves (short-dashed line in Fig. 1.1) only have $n^2 > 0$ in the troposphere, with $n^2 < 0$ throughout most of the stratosphere (above ~10 km). During the summer months, the stratosphere is shielded from virtually all tropospheric wave energy because $n^2 < 0$ throughout the entire stratosphere. This figure also hints at the interseasonal changes in wave-mean flow interaction in the stratosphere during the winter and summer months. VPWs can interact with the stratospheric flow in the NH during the boreal winter, while in the summer months the troposphere and stratosphere do not readily interact in terms of wave-mean flow interactions. This seasonality of the extratropical stratosphere will be explored in more detail later in this chapter.

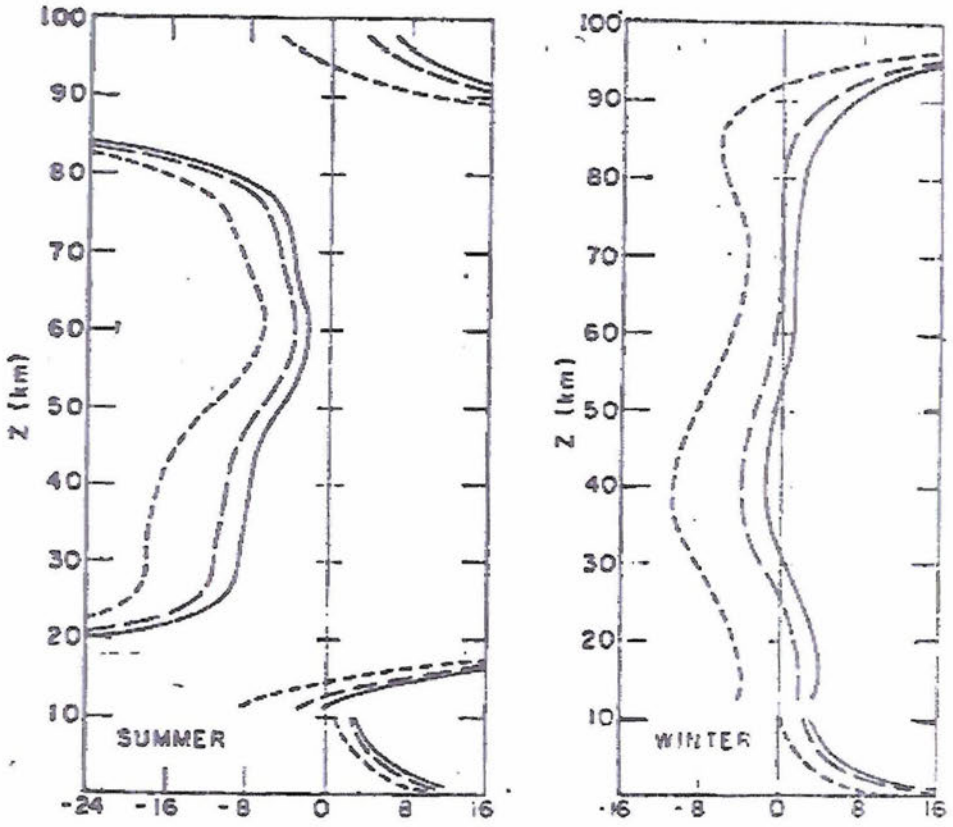

FIG. 1.1. Vertical profiles of the QG index of refraction averaged 30-60°N over the boreal summer (left) and boreal winter (right). Different lines correspond to different wavelengths (L). Solid line is L = 14,000 km, long-dashed line is L = 10,000 km, and short-dashed line is L = 6,000 km. The discontinuity represents the tropopause where N^2 also has discontinuity. Adapted from Charney and Drazin (1961).

1.1.2 How Do Vertically Propagating Waves Change the Mean State of the Stratosphere?

Assuming the criteria for wave propagation are met, tropospheric waves can vertically propagate through the troposphere and enter into the stratosphere. If a wave is steady with no frictional or diabatic effects acting on it, then as the wave propagates, the surrounding atmosphere is not changed in terms of momentum or thermal properties - the wave merely displaces the fluid, similar to ocean waves (e.g., Boyd 1976). Only when an atmospheric wave *breaks* do mixing and interactions take place between the wave and the ambient flow. Wave breaking occurs in regions no longer suitable for wave propagation. From the perspective of n^2, wave breaking occurs at the level where $\bar{u} - c = 0$ or the *critical level.* When waves break, the wave energy is deposited into the surrounding environment *at the critical level only.* Westward acceleration of the zonal-mean zonal flow at other levels is accomplished through an induced mean meridional circulation that works to redistribute momentum changes throughout the column.

To better understand the role of wave breaking on the mean flow, consider the QG zonal momentum equation in the transformed Eulerian mean framework:

$$\frac{\partial \bar{u}}{\partial t} - f\bar{v}^* = \left(\rho_o a \cos\varphi\right)^{-1} \nabla \cdot \mathbf{F} + \bar{F}, \qquad (1.3)$$

where an overbar $\left(\bar{}\right)$ denotes a zonal average, u is the zonal wind, $\bar{v}^*$ is the residual meridional wind, f is the Coriolis parameter ($= 2\Omega \sin\varphi$, where $\Omega = 7.292 \times 10^{-5} s^{-1}$, the angular speed of rotation of Earth), ρ_o is density, a is the radius of Earth, φ is latitude, F represents the frictional force, and $\nabla \cdot \mathbf{F}$ is the divergence of the Eliassen-Palm (EP) flux ($\mathbf{F}$; Eliassen and Palm 1961), defined as:

$$\mathbf{F} = \left(0, F_{\varphi}, F_{z}\right) = \left(0, -\rho_0 a\cos\varphi\overline{u'v'}, \rho_0 fa\cos\varphi\frac{\overline{v'\theta'}}{\partial\overline{\theta}/\partial z}\right). \quad \textbf{(1.4)}$$

where θ is potential temperature, $\overline{u'v'}$ is the eddy momentum flux and $\overline{v'\theta'}$ is the eddy heat flux. (1.3) states that the zonal-mean zonal flow can be changed locally through the eddy forcing terms in $\nabla\cdot\mathbf{F}$. Edmon et al. (1980) showed that $\mathbf{F}$ represents motion of atmospheric waves, and consequently $\nabla\cdot\mathbf{F}$ represents regions where wave energy diverges or converges (i.e., areas where waves break). Therefore, wave breaking ($\nabla\cdot\mathbf{F} < 0$) in the stratosphere applies a westward acceleration on the stratospheric zonal-mean circulation.

Along with changing the zonal-mean flow of the stratosphere, wave breaking also changes the mean thermal profile of the stratosphere. Through thermal wind balance, westward acceleration of the zonal-mean zonal flow by wave breaking implies a warming (cooling) of the extratropical stratosphere poleward (equatorward) and below the anomalous wave forcing. Once the zonal-mean zonal flow becomes easterly at a certain level, VPWs cannot penetrate beyond that level. With the absence of wave breaking above the critical level, radiative cooling then restores the stratospheric temperature profile back to equilibrium and consequently restores westerly flow to the region.

1.2 Variability in the Extratropical Stratosphere

1.2.1 Seasonal and Hemispheric Differences

Wave-mean flow interactions between VPWs and the circumpolar westerlies drive variability in the extratropical stratosphere. The primary source of waves that

interact with the stratospheric circulation differs depending on the hemisphere. In the NH, quasi-stationary waves (long waves) and baroclinic eddies (short waves) in the troposphere serve as sources of VPWs that interact with the stratospheric circulation (e.g., Andrews et al. 1987). In the Southern Hemisphere (SH), however, the lack of significant land-sea contrasts greatly reduces the quasi-stationary wave source. Therefore, the troposphere only provides relatively short waves to interact with the SH extratropical stratosphere.

Figures 1.2 and 1.3 further highlight the seasonal and hemispheric differences in the extratropical stratosphere. Fig. 1.2 shows the mean NH zonal-mean zonal winds from 1958-2001 averaged over four seasons: December – February (DJF; boreal winter), March – May (MAM; boreal spring), June – August (JJA; boreal summer) and September – November (SON; boreal autumn). During DJF, the extratropical stratosphere exhibits westerlies that amplify with height. The region in the extratropical stratosphere consisting of the maximum westerlies is called the polar night jet. This jet serves as the outer boundary for the stratospheric polar vortex, a region of relatively low geopotential heights generated by strong radiative cooling during the long polar night. The polar vortex resides primarily over the North Pole except when disturbed by wave-mean flow interactions. Also during DJF, strong baroclinicity in the middle and high latitudes and quasi-stationary waves provide amplified sources of tropospheric wave activity during the boreal winter. Hence, along with the presence of westerly winds, the NH extratropical stratosphere is particularly susceptible to wave breaking from VPWs during DJF. This time period is appropriately termed the "active season" for wave-mean flow interactions in the stratosphere. By contrast, in the summer months (JJA), the

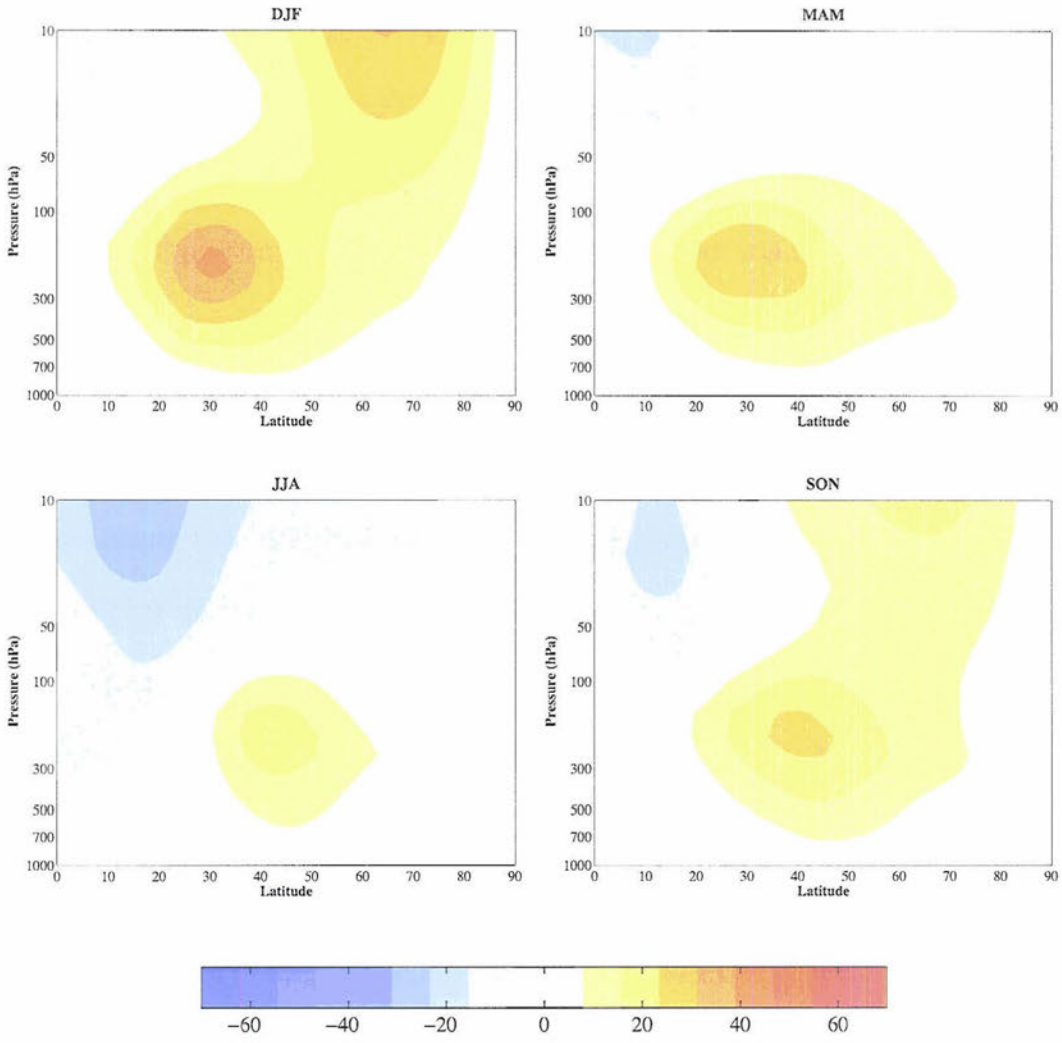

FIG. 1.2. Latitude-height plots of mean NH zonal-mean zonal winds from 1958-2001 and averaged over the four seasons: winter (DJF; upper left), spring (MAM; upper right), summer (JJA; lower left), and autumn (SON; lower right). Data from the European Centre for Medium-Range Weather Forecasts 40-year Reanalysis Project (ERA-40). Units are m/s. Colorbar denotes shaded contour values.

extratropical stratospheric flow is predominantly easterly, closing the stratosphere to substantial wave-mean flow interactions.

The SH zonal-mean zonal winds in the stratosphere (Fig. 1.3) are not symmetric to their NH counterparts in the respective seasons. During JJA (austral winter), the polar night jet is much stronger than the NH polar night jet (exceeding 70 m s^{-1}) and also located further equatorward. Despite strong baroclinicity and numerous baroclinic waves in the SH extratropical troposphere, the SH polar vortex is well protected from the influences of wave breaking because of these strong circumpolar winds. In turn, the SH circumpolar winds are stronger than their NH counterparts because of the lack of long waves in the SH troposphere. The combination of the strong wind speeds and the high wavenumber tropospheric wave source yields $\bar{u} - c > U_c > 0$ and hence $n^2 < 0$ from (1.1). Instead, the austral spring (SON) is the time when the SH polar stratosphere is most susceptible to wave-mean flow interactions. During this time, extratropical stratospheric winds are westerly but not as strong as during JJA; hence, the condition $0 < \bar{u} - c < U_c$ can be met even for high wavenumber waves. The austral summer is the quietest time for the SH extratropical stratosphere in terms of wave-mean flow interactions, with easterlies spanning the SH polar stratosphere.

Based on the interpretations of Figs. 1.2 and 1.3, the NH polar stratosphere should experience much more variability during the NH winter while the SH polar stratosphere should experience more variability during the SH spring. To explicitly illustrate this variability, Figure 1.4 shows daily geopotential height anomalies at 50 hPa over the NH and SH polar regions. The large scatter of the geopotential height anomalies in the NH during the boreal winter and in the SH during the austral spring demonstrates the large

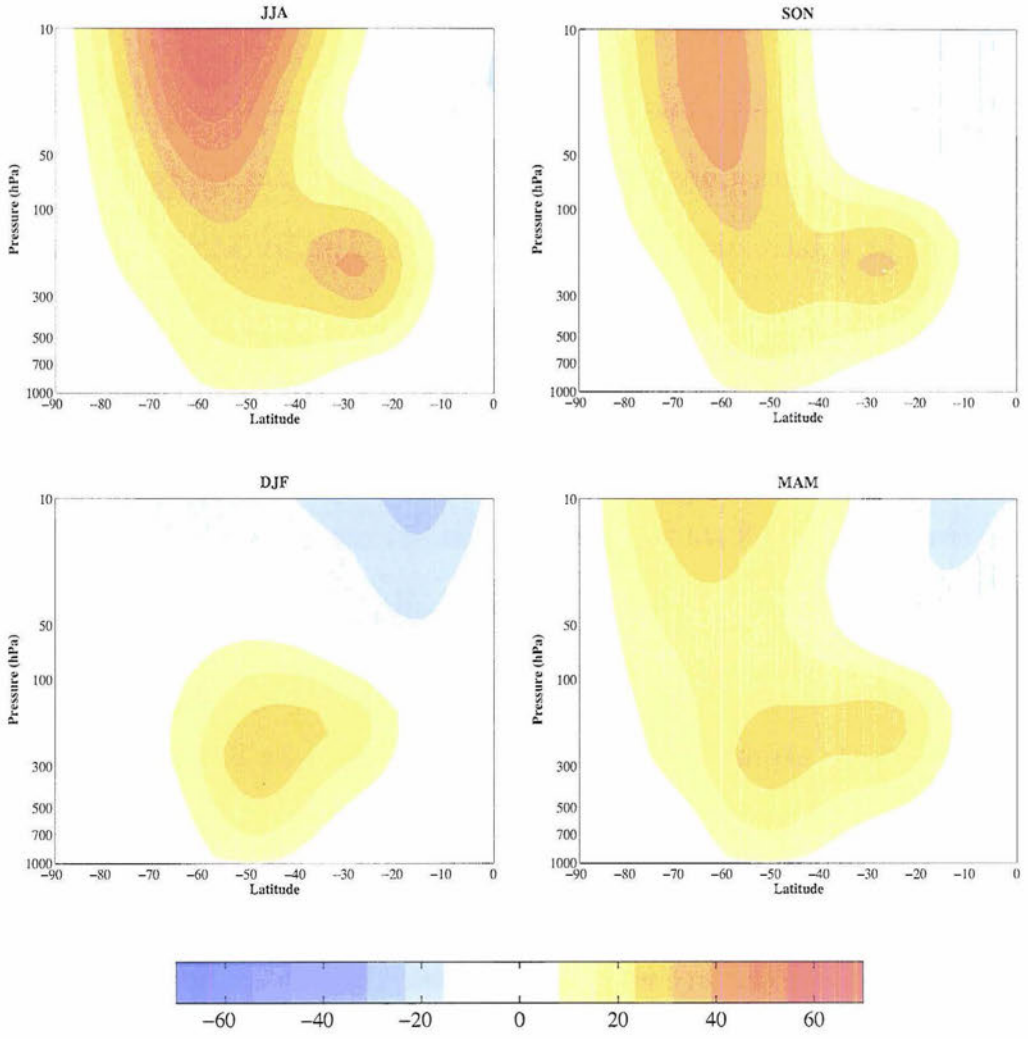

FIG. 1.3. Same as Fig. 1.2 except for the SH. Panels arranged in same seasonal order as Fig. 1.2: winter (JJA; upper left), spring (SON; upper right), summer (DJF; lower left), and autumn (MAM; lower right).

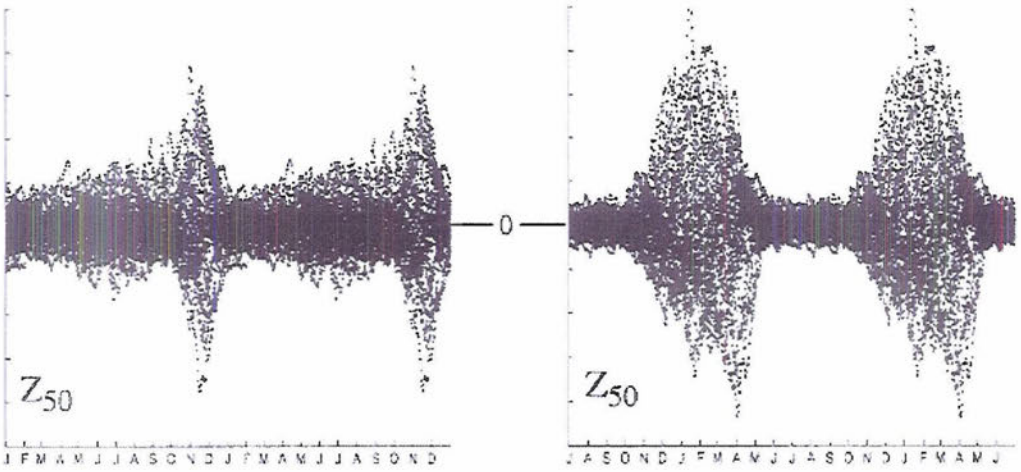

FIG. 1.4. Daily-mean 50 hPa geopotential height anomalies (i.e., the climatological mean is removed) from 1958-1997 averaged poleward of 70°. Left panel is for the SH; right panel for NH. Tick marks every 200 m with the zero line marked. Ordinate axes are lagged 6 months between both panels, and the annual cycle is repeated. Units are m. Adapted from Thompson and Wallace (2000).

variability in those seasons. The figure also shows that the NH stratosphere exhibits higher amplitude variability over the SH during the active season in each hemisphere.

1.2.2 Sudden Stratospheric Warmings

The climatology of the NH and SH polar stratosphere illustrates the general properties and mean profiles of the stratosphere in each hemisphere. In this section, however, we focus more on variability in the polar stratosphere. In particular, there are times when wave-mean flow interactions in the polar stratosphere can be so strong that the mean state of the stratosphere is completely altered. Continuous bombardment of the polar vortex by waves may actually stimulate a complete destruction or displacement of the polar vortex and consequently alter the stratospheric circulation. These disruptions are known as *sudden stratosphere warmings* (SSWs).

The lifecycle of a SSW occurs over the span of weeks to even months. Before a SSW, large pulses of wave activity occur at the polar vortex edge, peeling away the tight potential vorticity gradient guarding the polar vortex (e.g., McIntyre 1982; McIntyre and Palmer 1983). As wave breaking continues, the convergence of eddy heat fluxes warms the polar stratosphere and weakens the westerly winds. Sometimes the wave breaking may be so intense that westerly winds in the polar stratosphere actually reverse direction and become easterly. If easterlies replace the westerlies in the stratosphere, the SSW is termed a major SSW (e.g., Andrews et al. 1987). Otherwise, the SSW is termed a minor warming. Significant warming of the polar stratosphere accompanies a major SSW, with temperature increases as large as 40 K over a few days. Changes in momentum and heating in the polar stratosphere are redistributed throughout the atmospheric column via

an induced mean meridional circulation. Once wave breaking subsides, the polar vortex recovers over a timescale of weeks to months, as the stratospheric temperatures relax to radiative equilibrium. More details on the lifecycle of SSWs can be found in, for example, Limpasuvan et al. (2004).

In a pioneering effort to dynamically understand SSWs, Matsuno (1971) used a simple QG numerical model to simulate a major SSW in the NH. His findings suggested that anomalous wave breaking in the stratosphere initiates SSWs. Further experiments identified waves 1 and 2 (i.e., the scale of quasi-stationary waves) as drivers for both the simulated SSW and a NH SSW in January 1969. Hence, long waves serve as the primary drivers for SSWs, with wave 2 events rarer than wave 1 events (McIntyre 1982).

SSWs occur approximately once per season in the NH, excluding the "final warming" in the spring, when stratospheric winds switch to easterlies for the summer months (Andrews et al. 1987). Until 2002, major SSWs were not thought to occur in the SH because of the lack of significant quasi-stationary wave forcing to impact the stratospheric polar vortex. However, in September 2002, the SH polar stratosphere experienced an unprecedented major SSW. The event coincided with changes in the Antarctic ozone hole, triggering renewed interest in studying stratosphere/troposphere dynamical coupling in terms of climate prediction and climate change. Studies of this unprecedented SH SSW are compiled in Volume 62, Issue 3 of the *Journal of the Atmospheric Sciences*.

1.3 Stratosphere/Troposphere Dynamical Coupling in Observations and Models

So far, we have investigated wave-mean flow interactions in theory and applied the theory to understanding extratropical stratospheric variability. In this section we explore previous observational and numerical modeling studies on dynamical coupling of the stratosphere and troposphere. By looking at these studies, we will obtain a sense of the current level of understanding of the coupled system and motivate the work to be presented in this thesis.

1.3.1 Observational Studies of Stratosphere/Troposphere Dynamical Coupling

During the late 1960s and through the 1970s, most studies on extratropical stratosphere/troposphere dynamical coupling focused on tropospheric wave driving and its impacts on the stratospheric flow. Beginning in the late 1970s, however, observational evidence surfaced that suggested the tropospheric circulation could be impacted by stratospheric anomalies. Quiroz (1977) showed that as a major SSW unfolded, zonal-mean zonal winds and temperatures changed in both the stratosphere and troposphere. Later, Quiroz (1979) demonstrated that a major warming in January 1979 was associated with amplifications of geopotential height perturbations for wave 1 and wave 2 in both the stratosphere and the troposphere. O'Neill and Youngblut (1982) further elaborated on changes in tropospheric wave activity associated with a major SSW in January 1979. The authors showed that tropospheric waves propagated anomalously poleward prior to a SSW and argued that this change in wave propagation led to a feedback on the zonal-mean zonal flow in the troposphere.

For the remainder of the 1980s, observational studies on stratosphere/troposphere dynamical coupling scarcely appeared in the climate literature. Recently, however, renewed interest in the impacts of stratospheric anomalies on the tropospheric circulation has emerged in the climate literature, primarily in response to implications of stratosphere/troposphere coupling on weather prediction and climate change. Baldwin et al. (1994) and Perlwitz and Graf (1995) suggested that month-to-month variations in the extratropical stratospheric circulation are associated with distinct wave-like circulation anomalies in the troposphere. Later, Baldwin and Dunkerton (1999, 2001) also argued that changes in the stratospheric circulation can affect the weather of the troposphere some time after the initial perturbation in the stratosphere. To illustrate this idea, Figure 1.5 shows composites of the temporal evolution of downward propagating signals of the Northern Annular Mode (NAM), the dominant pattern of variability in the NH extratropics (Thompson and Wallace 1998), during weak (e.g., SSWs) and strong stratospheric polar vortex events. After day 0, both cases show same-signed anomalies in the NAM traverse between the stratosphere and the troposphere. Since the NAM describes changes in the position of the zonal jets and consequently the storm tracks (Thompson and Wallace 2000; Thompson et al. 2002; Baldwin et al. 2002), observing daily changes in the NAM at stratospheric levels may prove beneficial for improving weather prediction skills. Thompson and Wallace (2000) further linked fluctuations in the tropospheric annular modes in both hemispheres to fluctuations in strength of the stratospheric polar vortex.

Observational studies have also examined impacts of the coupled system on climate prediction and climate change. Hartmann et al. (2000) argued that ozone

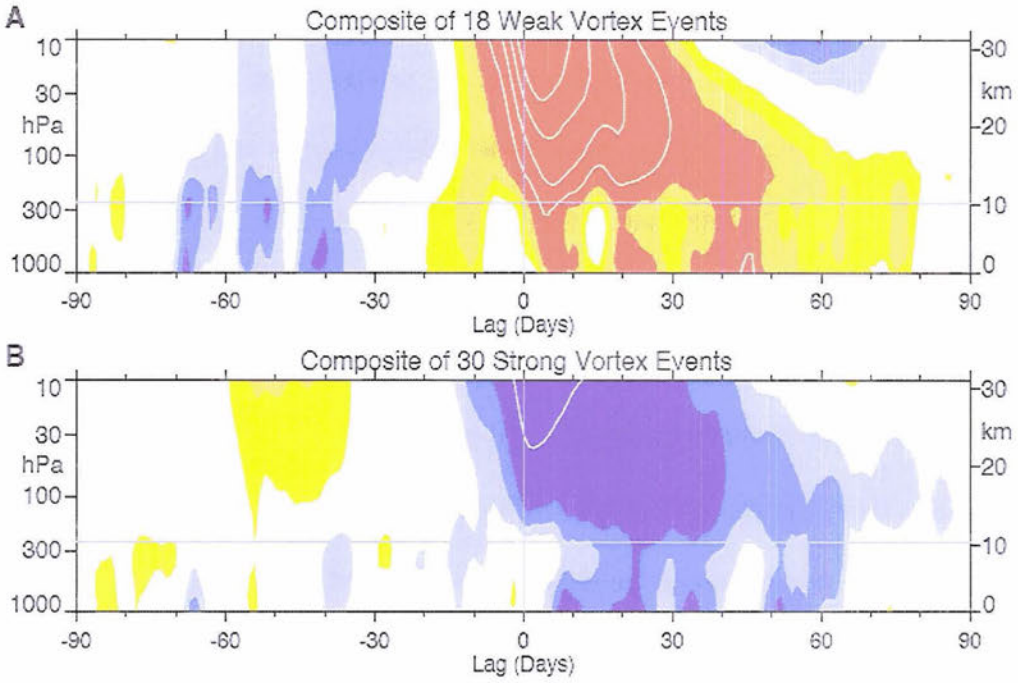

FIG. 1.5. Composites of the time-height evolution of the NAM for 18 weak vortex events (A; top) and 30 strong vortex events (B; bottom). Contour interval every 0.25 for shading; 0.5 for line contours. Values are dimensionless. Horizontal gray lines denote the approximate location of the tropopause. Adapted from Baldwin and Dunkerton (2001). See their paper for more details on the composite criteria.

depletion in the NH can lead to a stronger polar vortex which in turn deflects planetary waves from the troposphere at high latitudes more equatorward, making SSWs less frequent. The result is a positive feedback in which as the NH polar vortex strengthens, ozone depletion rates accelerate and the tropospheric and polar night jets move further poleward, reducing wave activity at high latitudes and reinforcing the stronger polar vortex (see Thompson et al. 2000 for more on trends in the NAM). Thompson and Solomon (2002) found analogous trends in the SH. Figure 1.6 shows the thirty-year linear trends in geopotential height averaged near 70°S. Not only has geopotential height significantly lowered in the polar stratosphere, but significant geopotential height changes (more than one standard deviation) are also observed in the troposphere, especially during the austral spring (i.e., the SH active season).

1.3.2 Modeling Studies of Stratosphere/Troposphere Dynamical Coupling

Numerical modeling studies readily simulate the dynamic coupling between large amplitude anomalies in the stratospheric and tropospheric circulations as seen in observations. Boville (1984) found that the structure of the polar night jet in his general circulation model (GCM) influenced the structure of planetary waves and transient eddies in the troposphere. Hence, a well-resolved stratosphere is a key factor in accurate predictions of tropospheric weather. Using a GCM with perpetual January conditions, Christiansen (2000) illustrated that downward propagation of the Holton and Mass (1976) stratospheric vacillation cycles constitutes much of the stratospheric variability in his GCM. The author further noted that the downward propagation of the vacillation cycles has a significant correlation with upper tropospheric winds in the high latitudes.

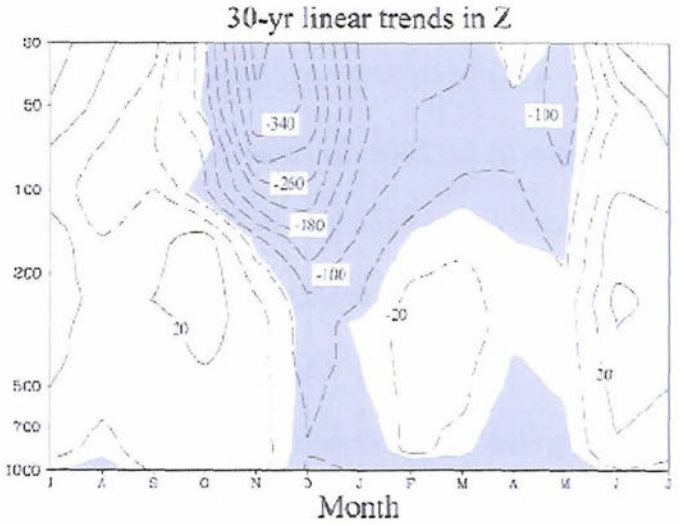

FIG. 1.6. Thirty-year (1969-1998) linear trends in geopotential height for radiosonde stations near 70°S. Contour interval every 40 m/(30 years) [...-60 -20 20 60...]. Solid contours denote positive values; dashed negative. Shading indicates where trends exceed 1 standard deviation of their respective monthly time series. Adapted from Thompson and Solomon (2002).

Polvani and Kushner (2002) offered model results consistent with the findings in Christiansen (2000) and Baldwin and Dunkerton (2001). In their model, the troposphere served only as a source of waves that vertically propagate and interact with the stratospheric polar vortex. The results suggested that the extratropical troposphere is sensitive to the strength of the polar vortex. Figure 1.7 shows the Polvani and Kushner (2002) model solutions for zonal-mean zonal wind, integrated over 25 model years, for five different thermal profiles of the polar stratosphere. The figure demonstrates that the larger the lapse rate in the stratosphere (i.e., the stronger the polar vortex), the stronger and more poleward the tropospheric zonal jet is. In later work, Kushner and Polvani (2004) expanded on the Polvani and Kushner (2002) results and explored the dynamics of the enhanced tropospheric jet. These results demonstrated that perturbations in stratospheric mechanical forcing profiles trigger tropospheric circulation anomalies, but these tropospheric anomalies cannot be maintained without eddy feedbacks included in the model.

1.4 Stratosphere/Troposphere Dynamical Coupling Mechanisms

While previous literature shows some relationship between variability in the extratropical stratosphere and troposphere, the dynamics of this coupling remains debatable within the community. Some theories attribute the apparent tropospheric response to the direct impact of anomalous stratospheric forcing via the induced mean meridional circulation (Haynes et al. 1991), the rearrangement of potential vorticity in the stratosphere (Hartley et al. 1998, Black et al. 2002), or wave reflection in the upper

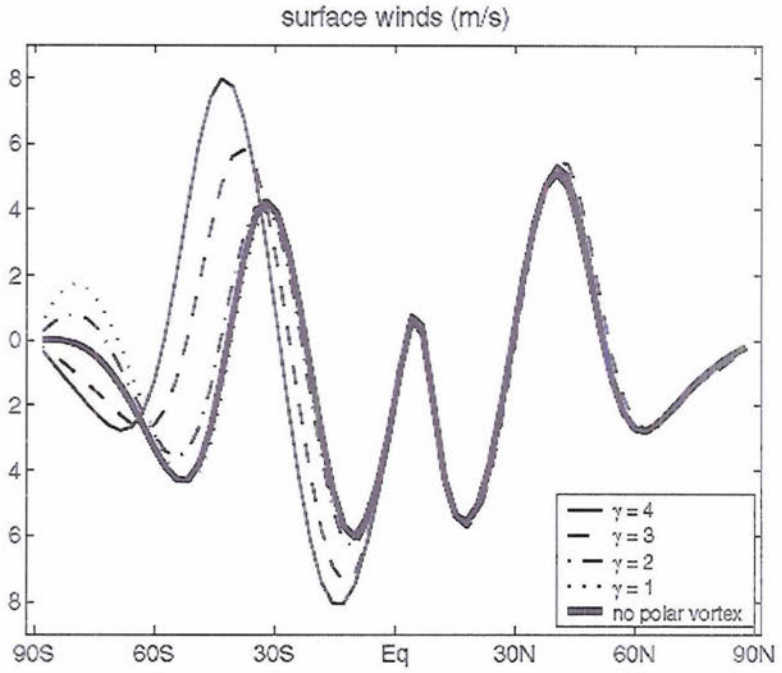

FIG. 1.7. Zonal-mean zonal wind averaged over 25 years of simulations in the Polvani and Kushner (2002) model for five different experiments. The experiments vary by the strength of the polar vortex. In the legend, γ denotes a parameter which measures the strength of the polar vortex; the larger the value of γ, the stronger the vortex. Units are m/s. Adapted from Polvani and Kushner (2002).

stratosphere (Perlwitz and Harnik 2003). Other theories explain the response of the tropospheric circulation through induced changes in tropospheric wave propagation and tropospheric eddy feedbacks (Robinson 2000; Kushner and Polvani 2004; Song and Robinson 2004). In this section we detail two proposed mechanisms of stratosphere/troposphere dynamical coupling: the balanced response to anomalous stratospheric forcing and the impact of the stratospheric circulation on tropospheric wave activity.

1.4.1 The Balanced Response

One way of creating a tropospheric response from anomalies in the stratosphere is through the balanced response to anomalous stratospheric forcing as described in Eliassen (1951), Dickinson (1968), and Haynes et al. (1991). The latter study investigated the transient and steady state response of the extratropical atmosphere to imposed mechanical forcing in the stratosphere. The authors argued that momentum forcing in the stratosphere is transmitted to the surface via an induced mean meridional circulation. The mechanism goes as follows. Suppose that an area of EP flux convergence exists in the lower stratosphere. Locally, the region of EP flux convergence acts as an easterly body force on the stratospheric flow and applies an easterly acceleration to the zonal-mean zonal wind there. This easterly acceleration will induce anomalous poleward motion across the axis of forcing due to the Coriolis torque. In the transient case, convergence of mass poleward of the forcing will then generate a sinking branch below and a rising branch above the airflow there. These vertical motions will adiabatically warm the air poleward and below the forcing but cool the air poleward and

above the axis of forcing. By continuity, equatorward flows above and below the forcing form two stacked meridional cells. The upper cell enhances the equator-to-pole temperature gradient, and the lower cell mitigates the thermal gradient. The equatorward motions above and below the forcing are affected by the Coriolis torque, inducing easterly acceleration of the zonal-mean zonal wind above and below the forcing. Hence, the entire column of air experiences an easterly acceleration resulting from a discrete area of wave breaking. In the steady state case, the upper meridional overturning cell vanishes as the vertical shear of the zonal-mean zonal wind approaches zero. Yet, in both the transient and steady state cases, the lower cell transports easterly momentum downward into the troposphere, altering the tropospheric zonal-mean flow.

In this text, we examine only the near-instantaneous response of the atmosphere to anomalous forcing (e.g., Eliassen 1951). This response is herein referred to simply as the "balanced response." "Balanced" refers to both geostrophic and hydrostatic balance.

1.4.2 Impact of the Stratospheric Circulation on Tropospheric Wave Activity

Another way that the stratosphere may affect the circulation of the troposphere is through impact of the zonal flow in the lower stratosphere on the flux of wave activity at the tropopause level. Chen and Robinson (1992) and Hu and Tung (2002) suggested that anomalous zonal wind shear near the tropopause has a significant effect on increasing the QG index of refraction and consequently enhancing vertical wave propagation. Upper stratospheric winds (e.g., the polar night jet), though, appear to have little to no effect on wave activity (Chen and Robinson 1992).

The impact of the stratosphere on the tropospheric circulation may also be enhanced by internal tropospheric variability via a feedback mechanism described by Robinson (2000). In this case, anomalous tropospheric zonal-mean zonal winds can act to organize tropospheric wave activity in a way that reinforces the present anomaly. For example, suppose westerly anomalies are generated in the extratropical upper troposphere by an area of EP flux divergence in the lower stratosphere. By thermal wind balance the enhanced jet implies a stronger meridional temperature gradient, favoring enhanced baroclinic eddy growth in the underlying region. However, the stronger westerly winds also serve as a more effective wave deflector as winds speeds increase and approach U_c. Waves will tend to be deflected equatorward, which will pump eddy momentum fluxes poleward into the jet and reinforce the wind anomalies. Hence, Robinson's theory implies baroclinic waves indirectly excited by stratospheric anomalies maintain the induced tropospheric wind anomalies.

1.5 Objectives and Outline for the Thesis

Current work on stratosphere/troposphere dynamical coupling aims to learn how variations in stratospheric wave drag impact the tropospheric circulation. Although the balanced response must operate in the coupled system, previous studies have viewed the balanced response as inadequate in explaining the observed amplitude of the tropospheric response. A major reason for this viewpoint is because a relatively small fraction of the total mass of the atmosphere resides above the tropopause (roughly 10%). This thesis refutes this viewpoint – that is, we argue that the balanced response is more than capable

of explaining the observed tropospheric response to stratospheric wave drag and radiative cooling. We thus suggest that the tropospheric eddy feedbacks advocated by other studies are not required to account for the amplitude of the tropospheric response.

The thesis is organized as follows. Chapter 2 provides an overview of the data used in this study and the statistical tools used to analyze relationships between stratospheric anomalies and the tropospheric circulation. Chapter 3 examines observations of stratosphere/troposphere dynamical coupling in the Eulerian mean and transformed Eulerian mean frameworks. By examining the coupling in two frameworks, we gain a sense of the different physical processes in the governing equations that may generate the observed responses in the stratosphere and troposphere. Then, in Chapter 4, we employ a simple numerical model to quantify the effects of the balanced response of the atmosphere to anomalous forcing in the stratosphere. The model results are compared to observations of the tropospheric anomalies to determine the effectiveness of the model in describing the observed tropospheric variability. Finally, Chapter 5 provides a summary of the results along with ideas for future work.

CHAPTER 2

DATA AND METHODOLOGY

2.1 Data

The dataset used in this thesis is the European Centre for Medium-Range Weather Forecasts (ECMWF) 40-year reanalysis project (hereafter referred to as ERA-40; Simmons and Gibson 2000). The data span from 1948 through part of 2002, but for this study, we will only use the subset of data from 1958-2001. The choice of 1958 is set to coincide with the International Geophysical Year, when major improvements to atmospheric observing systems were made worldwide (Simmons and Gibson 2000), while 2001 is the last full year of data available when this study began. The data are a hybrid of *in-situ* and remotely-sensed measurements synthesized through a data assimilation system. The data assimilation program constructs analysis fields every six hours along with intermediate three-hour forecast fields. The standard model grid for ERA-40 consists of 125 km grid spacing in the horizontal and 60 vertical levels between the surface and ~65 km. The data can then be interpolated onto a variety of other grids. For this study, we use the ERA-40 dataset with a 2.5° by 2.5° horizontal grid spacing and 23 vertical pressure levels, ranging non-uniformly from 1000 hPa to 1 hPa.

ERA-40 contains 11 atmospheric variables available for download from either the ERA-40 data archive directly from ECMWF or from the National Center of Atmospheric

Research (NCAR) Data Support Section (DSS). These 11 variables are geopotential height, temperature, the three wind components (u, v, and ω), relative humidity, specific humidity, vorticity, potential vorticity, divergence, and ozone mass mixing ratio. In this study, we will only use geopotential height, temperature, and the three wind components, deriving all other quantities from those variables[1].

2.2 Methodology

This study focuses on extratropical stratosphere/troposphere dynamical coupling in the NH only. All data are first daily and zonally averaged, and then the long-term daily means for each grid point and day are subtracted to obtain the anomaly fields. Because stratosphere/troposphere dynamical coupling in the NH is most active during boreal winter, we restrict our analyses between November – April, with a bulk of the results using only January – March (JFM) data.

We now provide a brief description on the statistical methods used in this study.

2.2.1 Linear Regression Analysis

For two arbitrary time series $x(t)$ and $y(t)$, the approximation of $y(t)$, using $x(t)$ as a linear predictor, can be written as

$$y(t) = \hat{y}(t) + \varepsilon = a_o + a_1 x(t) + \varepsilon, \qquad \textbf{(2.1)}$$

---

[1] In late 2004, the NCAR DSS discovered errors in u and v supplied with the original ERA-40 dataset. The DSS corrected these wind components and supplied the corrected versions for download. All observations and derived fields shown in this thesis will use the corrected u and v winds.

where $\hat{y}(t) = a_o + a_1 x(t)$ denotes a linear approximation between $x(t)$ and $y(t)$, and ε is the error in this approximation (e.g., Wilks 1995; Hartmann 2005). ε can be minimized in the least-squares sense with proper choices for a_o and a_1. The optimal choices for a_o and a_1 in order to minimize ε^2 are

$$a_1 = \frac{\overline{x'y'}}{\overline{x'^2}}, \tag{2.2}$$

$$a_o = \overline{y} - a_1 \overline{x}, \tag{2.3}$$

where overbars denote means; i.e.,

$$\overline{(\,)} = \frac{\sum_{i=1}^{N} (\,)_i}{N} \tag{2.4}$$

(N is the total number of samples), and primes denote departures from the mean; i.e.,

$$(\,)' = (\,) - \overline{(\,)}. \tag{2.5}$$

a_1 is called the *regression coefficient* and describes the slope of the linear relationship between the two variables (i.e., the change in y per unit change in x). If x is standardized, then the units of the regression coefficient are the units of y per standard deviation in x.

2.2.2 Statistical Significance

(2.1) provides an estimate for predicting $y(t)$ linearly based only on $x(t)$. However, deriving (2.1) does not necessarily mean the relationship is "statistically significant." That is, (2.1) could describe a relationship between two time series that occurs simply by chance. In order to determine the statistical significance of the linear

relationship between $x(t)$ and $y(t)$, the t-statistic is used. We define the t-statistic in relation to the correlation coefficient, r, as

$$t = \frac{r\sqrt{N_{eff} - 2}}{\sqrt{1 - r^2}}, \tag{2.6}$$

where

$$r = a_1 \frac{\sqrt{\overline{x'^2}}}{\sqrt{\overline{y'^2}}}, \tag{2.7}$$

and N_{eff} is the effective sample size. The square of r tells us the fraction of the total variance of $y(t)$ explained by (2.1). N_{eff} is used instead of the total sample size, N, to account for persistence in the dataset. The larger the difference between N and N_{eff}, the more persistence the dataset contains. To calculate N_{eff}, we use the formulation derived by Bretherton et al. (1999):

$$N_{eff} = N \frac{1 - r_1 r_2}{1 + r_1 r_2}, \tag{2.8}$$

where r_1 and r_2 are the lag-one autocorrelations of $x(t)$ and $y(t)$, respectively.

2.2.3 Empirical Orthogonal Function Analysis

Empirical orthogonal function (EOF) analysis (or principal component (PC) analysis) is used to calculate the NAM time series, which we use as the base index for our linear regression analysis. The primary purpose of EOF analysis is to break a large dataset with many state vectors into a smaller set of state vectors that explains a large fraction of the variability in the original dataset (Wilks 1995).

In this study, we perform EOF analysis via singular value decomposition (SVD) of the data matrix. Consider a data matrix $\mathbf{A}_{MXN}$, where M represents the number of temporal points and N the number of spatial points. $\mathbf{A}$ can be factored into three distinct matrices as demonstrated below:

$$\mathbf{A}_{MXN} = \mathbf{U}_{MXM}\Sigma_{MXN}\mathbf{V}_{NXN}{}^{T}, \tag{2.9}$$

where the columns of $\mathbf{U}$ are the eigenvectors of $\mathbf{AA}^T$, the columns of $\mathbf{V}$ are the eigenvectors of $\mathbf{A}^T\mathbf{A}$ ($\mathbf{U}$ and $\mathbf{V}$ are orthogonal), and the diagonal of Σ contains the square roots of the nonzero eigenvalues of $\mathbf{A}^T\mathbf{A}$ and $\mathbf{AA}^T$. In terms of EOF analysis, the columns of $\mathbf{U}$ represent the normalized PC time series (i.e., temporal eigenvectors), and the columns of $\mathbf{V}$ are the spatial eigenvectors associated with each PC time series. The first EOF (i.e., the first column is $\mathbf{V}$) is called the leading EOF and is the spatial pattern that explains the largest fraction of variability in the dataset. Subsequent EOFs explain successively lower fractions of variability. The PC time series represents the temporal evolution of each individual EOF pattern. For example, the first column of $\mathbf{U}$ (the leading PC time series) describes the temporal evolution of the leading EOF.

Before EOF analysis is performed, we must prepare the original data for SVD. First, the seasonal mean is removed from the data because we are interested in intrinsic patterns of variability in the dataset outside of the seasonal cycle. The data matrix is set up like $\mathbf{A}$, so that the state vectors reside in the row space and time in the column space. All grid points are weighted by the square root of the cosine of latitude to account for the different sizes of grid boxes between tropical and polar latitudes. The square root of the cosine of latitude is used rather than the cosine of latitude because the eigenvectors in $\mathbf{U}$ and $\mathbf{V}$ are found through analysis of $\mathbf{AA}^T$ and $\mathbf{A}^T\mathbf{A}$, respectively.

EOFs and PCs alone have arbitrary amplitude and are dimensionless. A convenient way to present EOFs is by regressing the original data matrix onto standardized values of the respective PC time series. The spatial pattern that emerges then has units of the original data and illustrates a pattern of variability in the dataset. For this discussion, we will refer to these presentation maps as "EOF-like maps." A similar procedure can be done for the PC time series. To develop a time series that measures the time evolution of a particular EOF-like pattern in the original dataset, we project individual spatial maps from the original dataset at each time step onto a particular EOF-like map (weighting the projection as necessary). This time series is known as the expansion coefficient time series.

The NAM time series is defined and calculated at every pressure level as follows. First, the leading PC time series of the November – April monthly mean geopotential height fields from 20 – 90°N at a pressure level is calculated using SVD analysis. Then, we construct an EOF-like map by regressing the November – April monthly mean geopotential height anomalies from 20 – 90°N at that level onto the standardized leading PC time series. Finally, daily geopotential height anomaly maps (weighted by the cosine of latitude) from 1958 – 2001 at that pressure level are projected onto the leading EOF-like map to construct the NAM time series, or NAM index. Thus, the NAM index is the expansion coefficient time series of the leading EOF-like pattern. The NAM index is standardized at each level, and the sign of the value of the index is set to conform to the convention set forth by Thompson and Wallace (1998) (i.e., a positive value of the NAM time series indicates lower heights over the pole and an annular ring of higher heights in the sub-polar latitudes).

CHAPTER 3

OBSERVATIONS OF STRATOSPHERE/TROPOSPHERE DYNAMICAL COUPLING IN THE EULERIAN MEAN AND TRANSFORMED EULERIAN MEAN FRAMEWORKS

In this chapter, we explore observational evidence of stratosphere/troposphere dynamical coupling in ERA-40. To explore this coupling, we examine the individual terms in the QG zonal momentum equation and the QG thermodynamic equation in both the Eulerian mean (EM) and transformed Eulerian mean (TEM) frameworks. While the tendencies in zonal-mean zonal wind and temperature are identical in both frameworks, interpreting these tendencies and why they occur differs. Specifically, we address the following questions:

(1) To what extent are changes in the stratospheric circulation associated with anomalies in the circulation of the troposphere and lower stratosphere?

(2) Which terms in the QG zonal momentum equation and the QG thermodynamic equation dominate the observed tendencies in the zonal-mean zonal wind and temperature fields in the stratosphere? In the troposphere?

(3) How do physical interpretations of the resulting coupling differ between the EM and TEM frameworks?

To examine how the terms in the momentum and thermodynamic equations relate throughout the atmospheric column to changes in the stratospheric circulation, we use standardized and inverted JFM values of the NAM time series at 10 hPa (NAM_{10}) as the base index for the linear regression analyses. Physically, the NAM describes a meridional seesaw in atmospheric mass between the polar and sub-polar latitudes, with a node located at ~45°N. In the stratosphere, the NAM also describes fluctuations in the strength and position of the polar vortex and hence can be used as a measure of the stratospheric circulation. NAM_{10} explains nearly 50% of the observed variability in the NH 10 hPa geopotential height field, making it a useful index for stratospheric circulation changes. Furthermore, JFM corresponds to the period when the stratospheric flow is susceptible to VPWs from the underlying troposphere (Thompson and Wallace 2000).

Figure 3.1 shows the regression of the NAM time series at every pressure level onto standardized and inverted JFM values of NAM_{10}. Shading indicates where corresponding correlations exceed the 95% confidence interval. Most of the signal in the stratosphere is significant between days -10 and +20, with longer persistence of significant signals in the lowermost stratosphere. Same-signed anomalies cross the tropopause before day -20 but do not impact the surface until about day -10 and then persist after that. Thus, Fig. 3.1 suggests changes in the stratospheric circulation (e.g., changes in NAM_{10}) have significant impacts on the tropospheric circulation (e.g.,

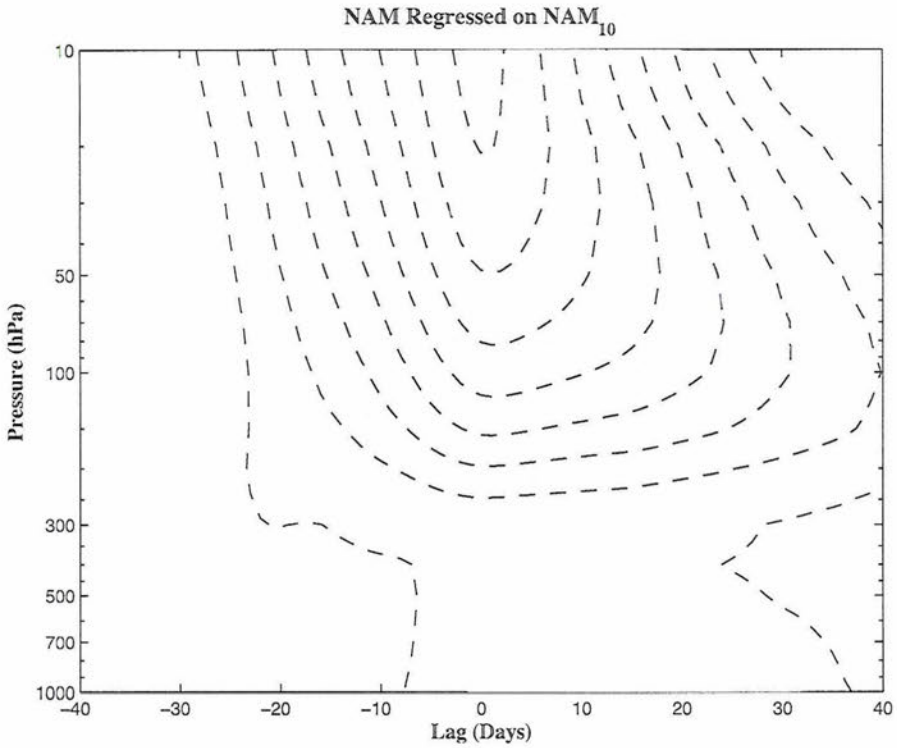

FIG. 3.1. Regression of the NAM time series at every pressure level, standardized for all calendar days, onto standardized and inverted JFM values of NAM_{10}. Contour interval 0.2. Solid contours denote positive values; dashed negative. The zero contour is omitted. Shading indicates corresponding correlations that exceed the 95% confidence interval. In this and all remaining plots, positive lags indicate NAM_{10} leads.

changes in the tropospheric NAM), consistent with the results in, for example, Baldwin and Dunkerton (2001).

All figures in this chapter except one (that one being a schematic) display lag regressions of anomalous data onto standardized and inverted JFM values of NAM_{10}. Lag regression coefficients are calculated by extending the anomalies earlier or later in the NH winter season as needed. For example, the regression value for zonal-mean zonal temperature anomalies at lag +10 is calculated by regressing zonal-mean zonal temperature anomalies from January 11 – April 10 onto standardized and inverted JFM values of NAM_{10}. Then, by construction, positive lags will correspond to times when NAM_{10} leads the variable and vice versa.

3.1 The Anomalous Mean Meridional Circulation and Its Role in Driving the Zonal-Mean Zonal Wind and Temperature Fields

As we explore the momentum and thermodynamic equations that govern the large scale atmospheric circulation, the eddy fluxes of momentum and heat will appear in the equations as forcing terms on the zonal-mean circulation. In this section, we highlight the impacts of each eddy flux term on the atmospheric circulation and the type of anomalous mean meridional circulation expected in response to each anomalous flux.

Figure 3.2 presents a schematic of the balanced response of the atmosphere to anomalous eddy heat and momentum fluxes in the NH stratosphere. Let us start with the anomalous heating case (Fig. 3.2a). Suppose there is anomalous heating of the polar stratosphere caused by meridional convergence of eddy heat fluxes. To balance the

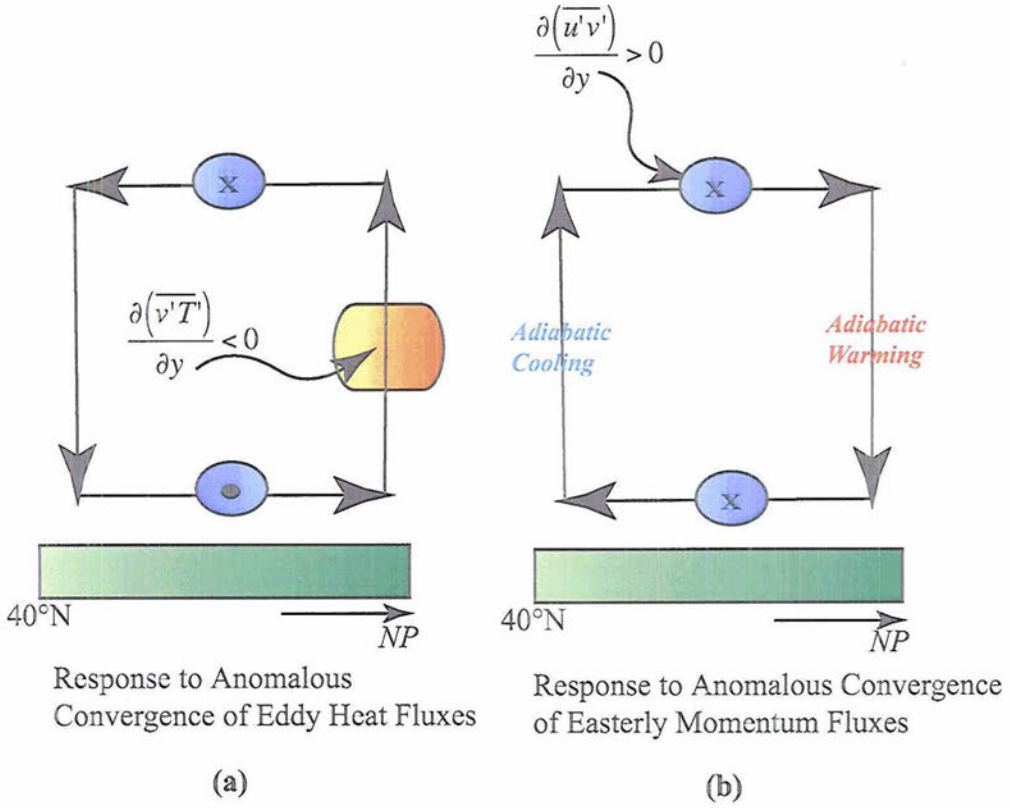

FIG. 3.2. (a) The balanced response to anomalous meridional convergence of eddy fluxes in the NH extratropical atmosphere. Large red ellipse denotes source of anomalous heating caused by the convergence of eddy heat fluxes. Direction of the anomalous mean meridional circulation indicated by arrows. "x" denotes anomalous easterly acceleration; dot anomalous westerly acceleration. (b) Same as (a), except for the balanced response to anomalous meridional convergence of easterly eddy momentum fluxes in the NH extratropical atmosphere. Maximum momentum forcing co-located with region of anomalous easterly acceleration denoted in the upper branch of the cell. Rising and sinking branches of the cell are annotated with the corresponding temperature response to adiabatic motions. In both figures, "NP" stands for "North "Pole."

anomalous heating at the high latitudes, upward motion is induced across the axis of heating, adiabatically cooling the air as it rises. While there is convergence of eddy heat fluxes in the polar stratosphere, the mid-latitude stratosphere will experience a *divergence* of eddy heat fluxes, inducing cooling and hence descending motion to adiabatically warm the air and counter the cooling. By continuity, equatorward motion is induced in the upper branch of the cell and poleward motion in the lower branch. The Coriolis force acting on the meridional motion will generate easterly acceleration in the upper branch and westerly acceleration in the lower branch of the anomalous mean meridional circulation. Hence, anomalous heating of the polar stratosphere generates opposite-signed accelerations of the zonal-mean zonal wind in the stratosphere and troposphere.

Now suppose there is anomalous meridional convergence of easterly momentum fluxes (or, equivalently, meridional divergence of westerly momentum fluxes) in the NH polar stratosphere (Fig. 3.2b). The convergence will act as a body force on the atmosphere and generate anomalous easterly acceleration of the zonal-mean zonal wind directly at the location of maximum forcing. The Coriolis force will then act upon the imposed easterly anomalies and induce poleward motion across the axis of maximum forcing. As mass converges in the polar latitudes and diverges in the sub-polar latitudes, conservation of mass dictates that air must sink in the polar regions and rise in the sub-polar latitudes, adiabatically warming and cooling the surrounding air, respectively. To complete the circulation, equatorward flow must exist below the level of the initial forcing. However, because of the Coriolis torque, this equatorward flow will be deflected westward, generating easterly acceleration on the zonal-mean zonal wind at that level.

Hence, the anomalous convergence of eddy momentum fluxes will create *same-signed* zonal-mean zonal wind accelerations throughout the atmospheric column.

Fig. 3.2 distinguishes the different effects that anomalous eddy momentum and heat fluxes have on the zonal-mean flow. Mechanical forcing via eddy momentum forcing creates a local response on the zonal-mean flow at the level of maximum forcing and then induces same-signed anomalies via the anomalous mean meridional circulation and the Coriolis torque. However, anomalous eddy heat fluxes rely on the Coriolis torque to affect the zonal-mean circulation.

3.2 Diagnostics in the EM Framework

3.2.1 The Zonal Momentum Equation

We begin our exploration of stratosphere/troposphere dynamical coupling by examining the individual terms in the QG zonal momentum equation in the EM framework. The EM QG zonal momentum equation may be written as

$$\frac{\partial \bar{u}}{\partial t} = -\frac{\partial\left(\overline{u'v'}\cos^2\varphi\right)}{a\cos^2\varphi\,\partial\varphi} + f\bar{v} + \bar{F}, \tag{3.1}$$

where an overbar $\left(\bar{}\right)$ denotes a zonal average, u is the zonal-mean zonal wind, $\overline{u'v'}$ is the eddy momentum flux, v is the meridional wind, a is the radius of Earth, φ is latitude, f is the Coriolis parameter ($= 2\Omega\sin\varphi$, where $\Omega = 7.292\times10^{-5}s^{-1}$, the angular speed of rotation of Earth), and F represents the frictional force. In (3.1) we have moved the EM Coriolis term $\left(\text{i.e.}, f\bar{v}\right)$ to the RHS of the equation for the purposes of this discussion.

The term $-\frac{\partial\left(\overline{u'v'}\cos^2\varphi\right)}{a\cos^2\varphi\partial\varphi}$ will be referred to as the "eddy momentum flux term" throughout this chapter. We ignore the effects of friction in this discussion since friction is most important only near the surface.

Figure 3.3 shows the regression of the first two terms on the RHS of (3.1), averaged 55-75°N, onto standardized and inverted JFM values of NAM_{10} (line contours) along with shading to denote where the corresponding correlations exceed the 95% confidence interval based on a two-tailed test of the *t*-statistic. In the stratosphere, $\partial\bar{u}/\partial t$ (Fig. 3.3a) behaves as expected – a weakening of the circumpolar flow prior to day 0 followed by strengthening of that flow. The maximum weakening occurs at 10 hPa on ~day -5. $\partial\bar{u}/\partial t$ then reverses sign at day 0 with a rapid rate of westerly acceleration between days +5 and days +20. After day +20, $\partial\bar{u}/\partial t$ decreases slightly as the stratospheric circulation returns to its equilibrium state. In the troposphere, similar behavior occurs but the acceleration is an order of magnitude less. To show the weaker tropospheric values of $\partial\bar{u}/\partial t$, extra contours (in red) are added to Fig. 3.3a at a contour interval of 0.01 m/s/day. Notice that between days -10 and 0, anomalous westward acceleration is evident throughout the entire atmospheric column to the surface. The extension of anomalous $\partial\bar{u}/\partial t$ to the surface occurs near the same time the tropospheric NAM takes on same-signed changes as the stratospheric NAM (Fig. 3.1). Though the tropospheric regressions are not indicated significant in Fig. 3.3a, the presence of the significant changes in the tropospheric NAM over the same time offers credibility to this

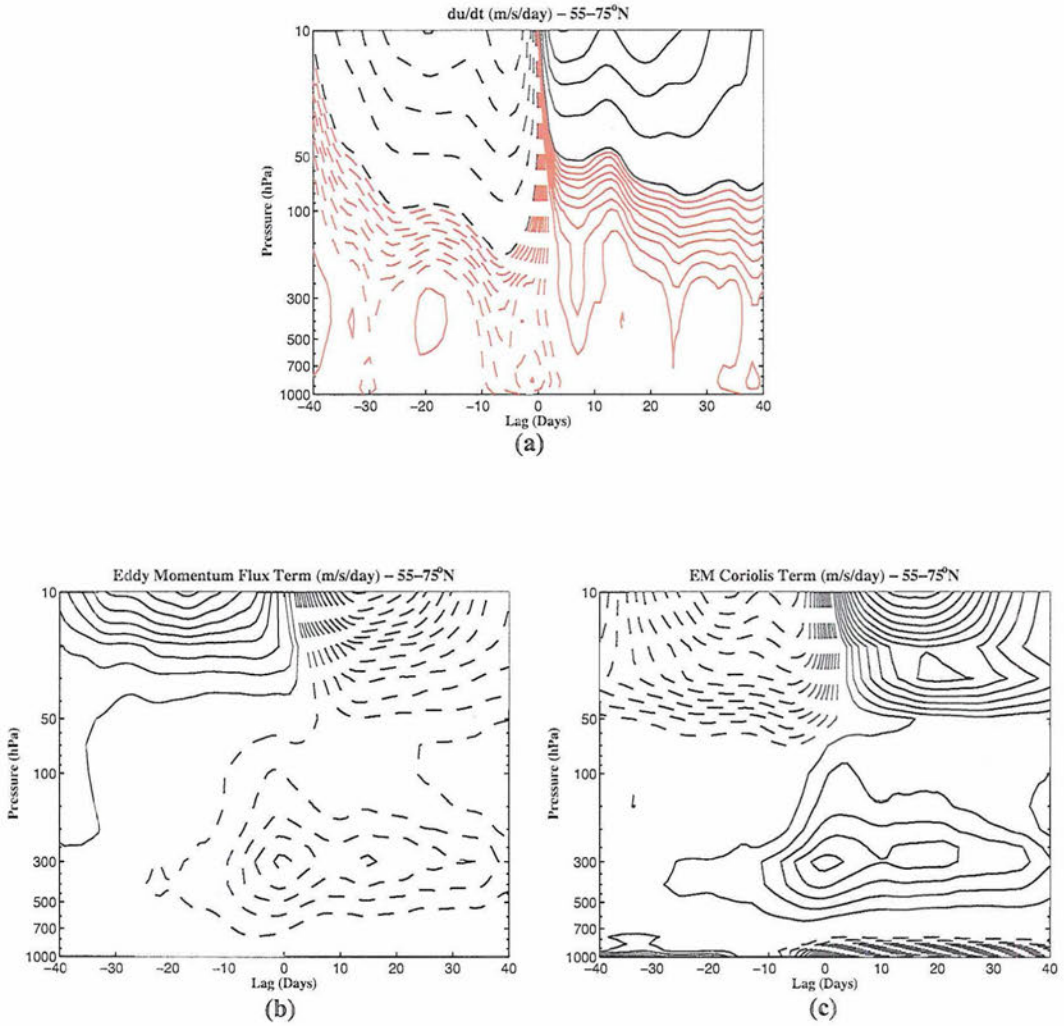

FIG. 3.3. (a) Zonal-mean zonal wind tendency anomalies averaged 55-75°N and regressed onto standardized and inverted JFM values of NAM_{10}. Contour interval 0.1 m/s/day for black contours; 0.01 m/s/day for red contours. (b) Same as (a), but contours are eddy momentum flux term anomalies, averaged 55-75°N and regressed onto standardized and inverted JFM values of NAM_{10}. (c) Same as (a), but contours are for EM Coriolis term anomalies, averaged 55-75°N and regressed onto standardized and inverted JFM values of NAM_{10}. Contour interval in (b) and (c) 0.1 m/s/day. Solid contours denote positive values; dashed negative. The zero contour is omitted. Shading indicates corresponding correlations that exceed the 95% confidence interval. Refer to the text for definitions of terms.

feature. After day 0, $\partial\bar{u}/\partial t \approx 0$ or weakly positive throughout the troposphere, suggesting the earlier induced weak zonal-mean zonal wind anomalies persist to ~day +40 and likely beyond.

Figs. 3.3b and 3.3c are the same as Fig. 3.3a except the contours represent the eddy momentum flux and EM Coriolis terms, respectively. These terms are largest at 10 hPa, and the sign of the two terms reverses after day 0, similar to $\partial\bar{u}/\partial t$. Focusing on the troposphere, there are two local minima in the eddy momentum flux term located near 300 hPa – one occurs on ~day -3 and the other local maximum on day +15. The minimum near day -3 is coincident with the extension of $\partial\bar{u}/\partial t$ anomalies throughout the troposphere (Fig. 3.3a), with the changes in the tropospheric NAM, and also with a maximum in the EM Coriolis term near the same time (Fig. 3.3c). The latter minimum, however, does not coincide well with apparent changes in $\partial\bar{u}/\partial t$ but does compliment the broad maximum in the EM Coriolis term. Fig. 3.3c also clearly illustrates the induced anomalous mean meridional circulation in the troposphere at positive lags with strong equatorward flow at the surface underneath poleward flow in the upper and middle troposphere.

Figure 3.4 shows the time series of the regression coefficients of $\partial\bar{u}/\partial t$ (red line), the eddy momentum flux term (solid black line), and the EM Coriolis term (dashed black line) from Fig. 3.3 at three distinct pressure levels: 10 hPa (representative of the middle stratosphere), 100 hPa (representative of the lower stratosphere), and 300 hPa (representative of the upper troposphere). At 10 hPa, the EM Coriolis term dominates the

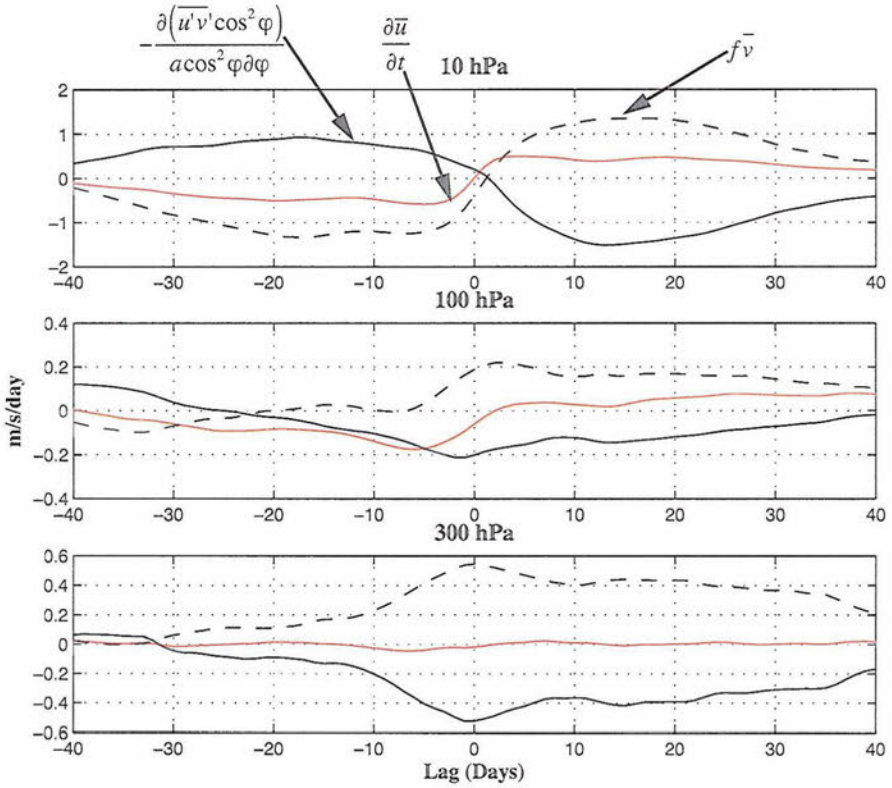

FIG. 3.4. Plots of zonal-mean zonal wind tendency anomalies (red), eddy momentum flux term anomalies (solid black), and EM Coriolis term anomalies (dashed black), each averaged 55-75°N and regressed onto standardized and inverted JFM values of NAM_{10}, at three pressure levels: 10 hPa (top), 100 hPa (middle), and 300 hPa (bottom). Units are m/s/day.

observed $\partial\bar{u}/\partial t$ signal. In the lower stratosphere (100 hPa), $\partial\bar{u}/\partial t$ tracks the EM Coriolis term at positive lags, but at negative lags, $\partial\bar{u}/\partial t$ generally has the same sign as the eddy momentum flux term. This relationship continues into the upper troposphere, where the eddy momentum flux term dominates the response in $\partial\bar{u}/\partial t$ at negative lags, especially between days -10 and 0. At positive lags in the upper troposphere, the two terms nearly cancel each other.

Figs. 3.3 and 3.4 suggest that different terms dominate the changes in the zonal-mean circulation in the troposphere and the stratosphere. In the stratosphere, the EM Coriolis term drives the observed $\partial\bar{u}/\partial t$ in agreement with previous studies (e.g., Matsuno 1971; O'Neill and Taylor 1979). In the troposphere, the eddy momentum flux term works to balance the EM Coriolis torque during both negative and positive lags so that $\partial\bar{u}/\partial t$ is nearly zero, except between days -10 to 0 when the eddy momentum flux term dominates in the upper troposphere and generates easterly acceleration (Fig. 3.4 bottom). This finding implies that mechanical forcing in the form of the eddy momentum fluxes primarily drives the tropospheric wind anomalies.

3.2.2 The Thermodynamic Equation

Although not explicitly listed in the EM QG zonal momentum equation, the thermodynamic profile of the stratosphere and troposphere also works to drive circulation anomalies through eddy heat fluxes and adiabatic motions. The EM QG thermodynamic equation can be written as

$$\frac{\partial \overline{T}}{\partial t} = -\frac{\partial\left(\overline{v'T'}\cos\varphi\right)}{a\cos\varphi\partial\varphi} - N^2 HR^{-1}\overline{w} + \overline{Q}, \qquad (3.2)$$

where T is temperature, $\overline{v'T'}$ is the eddy heat flux, N is the Brunt-Väisällä frequency, R is the ideal gas constant, H is the scale height, w is vertical velocity, and Q represents diabatic effects (e.g., radiation and latent heat release). For the remainder of this chapter, we will refer to the first term on the RHS of (3.2) as the "eddy heat flux term," and the second term on the RHS (3.2) will be called the "EM adiabatic term." We will reserve our discussion of $\overline{Q}$ for the TEM framework.

Figure 3.5 shows the regression of $\partial\overline{T}/\partial t$ (Fig. 3.5a), the eddy heat flux term (Fig. 3.5b), and the EM adiabatic term (Fig. 3.5c) onto standardized and inverted JFM values of NAM_{10} and averaged poleward of 60°N. Fig. 3.5a illustrates maximum anomalies of $\partial\overline{T}/\partial t$ occur at 10 hPa on day -20 with apparent downward propagation of these anomalies throughout the stratosphere until day 0. After day 0, rapid cooling begins at 10 hPa on day +6 and again appears to propagate downward to the tropopause. The changes in $\partial\overline{T}/\partial t$ also correspond well with the changes in the eddy momentum flux and EM Coriolis terms (Figs. 3.3b and 3.3c). Fig. 3.5a also demonstrates that the time scale of zonal-mean temperature changes is much longer in the lower stratosphere. In the troposphere, $\partial\overline{T}/\partial t$ is very small and not statistically significant.

When we look at the contributing factors to the observed $\partial\overline{T}/\partial t$, Figs. 3.5b and 3.5c demonstrate that the eddy heat flux and EM adiabatic terms counter each other. The eddy heat flux term abruptly changes sign around day 0 in the stratosphere, with eddy

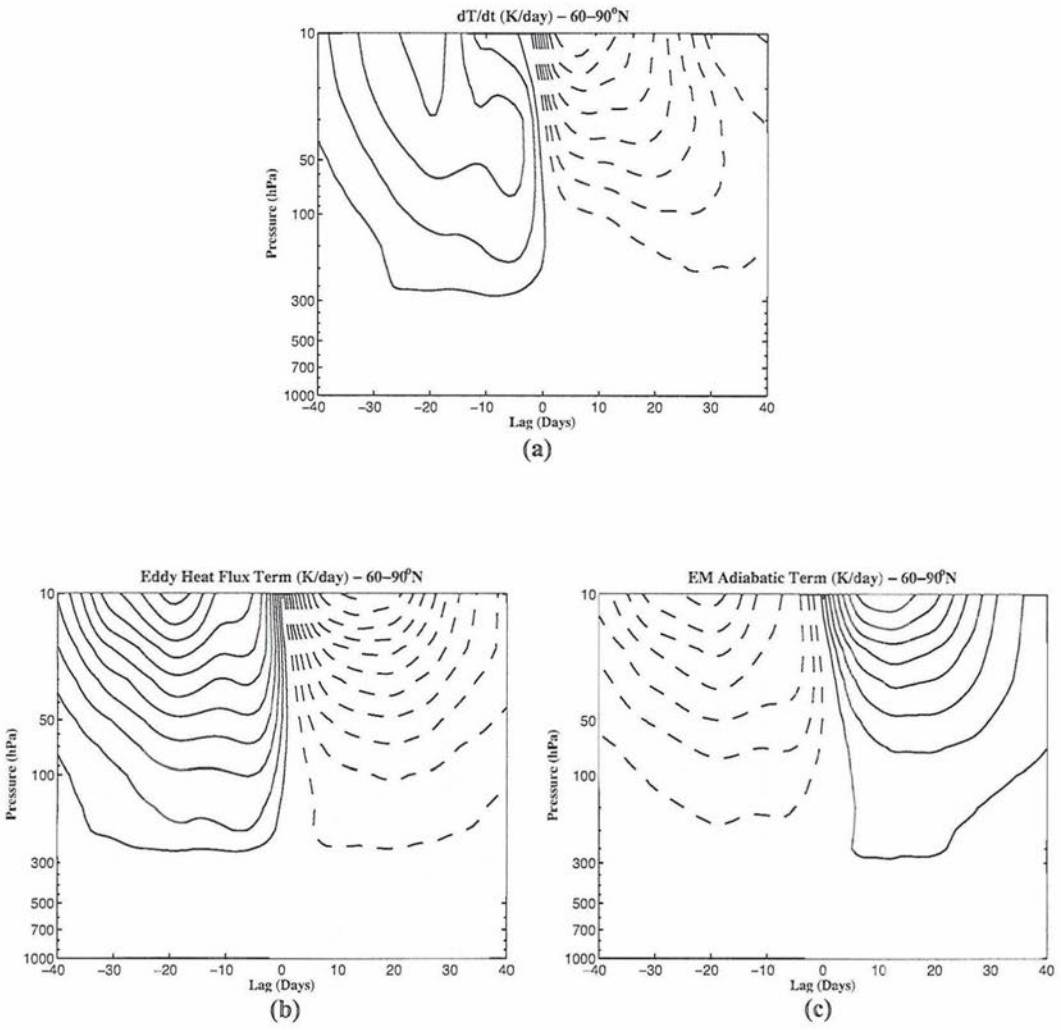

FIG. 3.5. (a) Same as Fig. 3.3, but contours are zonal-mean temperature tendency anomalies averaged 60-90°N and regressed onto standardized and inverted JFM values of NAM_{10}. Contour interval 0.05 K/day. (b) Same as (a), but contours are eddy heat flux term anomalies, averaged 60-90°N and regressed onto standardized and inverted JFM values of NAM_{10}. (c) Same as (a), but contours are EM adiabatic term anomalies, averaged 60-90°N and regressed onto standardized and inverted JFM values of NAM_{10}. Contour interval for (b) and (c) 0.1 K/day. Solid contours denote positive values; dashed negative. The zero contour is omitted. Shading indicates corresponding correlations that exceed the 95% confidence interval. Refer to the text for definitions of terms.

heat flux convergence (i.e., heating) before day 0 but divergence (i.e., cooling) after day 0. The EM adiabatic term (Fig. 3.5c) illustrates upward motion that adiabatically cools the air during negative lags, and vice versa at positive lags. Both terms show downward propagation through the stratosphere into the uppermost troposphere. Moreover, the eddy heat flux and EM adiabatic terms change most rapidly in the middle stratosphere yet change much more slowly in the lower stratosphere, agreeing with the persistence of the $\partial\overline{T}/\partial t$ anomalies in the same region.

Figure 3.6 is similar to Fig. 3.4 except for the terms of the EM thermodynamic equation. Throughout the stratosphere and into the upper troposphere, $\partial\overline{T}/\partial t$ almost exclusively follows the eddy heat flux term. Fig. 3.6 also demonstrates more clearly the compensating effects of the EM adiabatic term on the extratropical zonal-mean temperature response to the effects of the eddy heat flux term.

Though not an explicit term in (3.2), $\overline{w}$ is useful to analyze here because it represents the rising and descending branches of the anomalous mean meridional circulation in the EM framework. Figure 3.7 illustrates rising motion when the polar stratosphere warms (negative lags) and descending motion when the polar stratosphere cools (positive lags). From (3.2), $\overline{w}$ has components associated with the eddy heat flux term (an adiabatic contribution to the zonal-mean temperature) and $\overline{Q}$ (a diabatic contribution to the zonal-mean temperature); i.e., $\overline{w} = \overline{w_{adiabatic}} + \overline{w_{diabatic}}$. Hence, $\overline{w}$ does not exclusively capture the effects of diabatic heating on the zonal-mean circulation. As a result, $\overline{w}$ cannot exclusively diagnose mass fluxes or parcel movement in the atmosphere. In order to isolate the effects of the diabatic circulation (i.e., the circulation

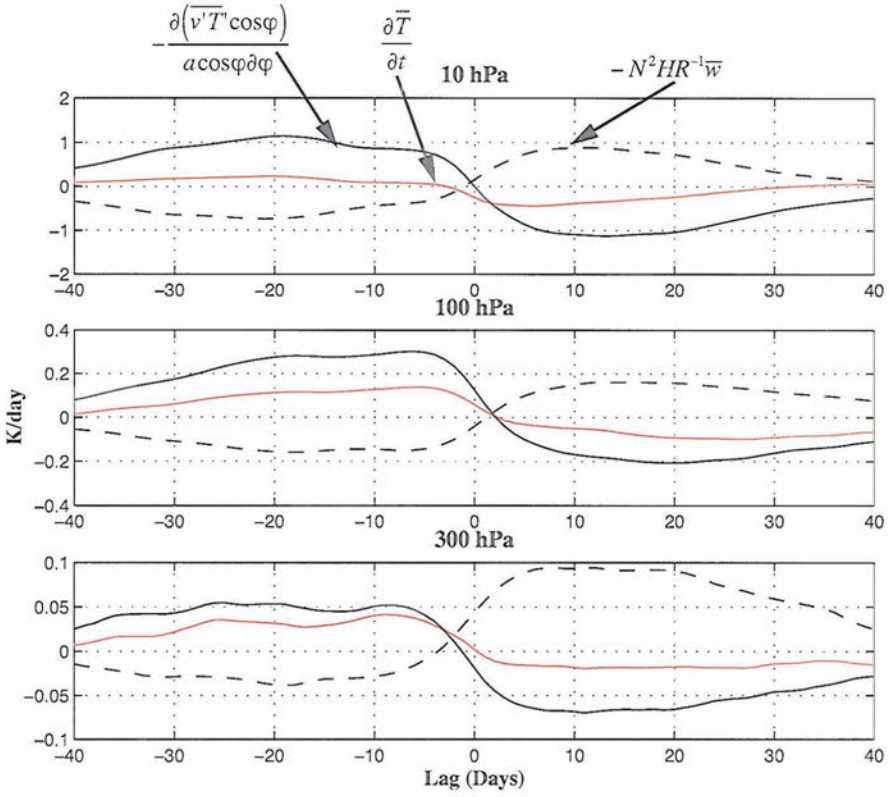

FIG. 3.6 Zonal-mean temperature tendency anomalies (red), eddy heat flux term anomalies (solid black), and EM adiabatic term anomalies (dashed black), each averaged 60-90°N and regressed onto standardized and inverted JFM values of NAM_{10}, at three pressure levels: 10 hPa (top), 100 hPa (middle), and 300 hPa (bottom). Units are K/day.

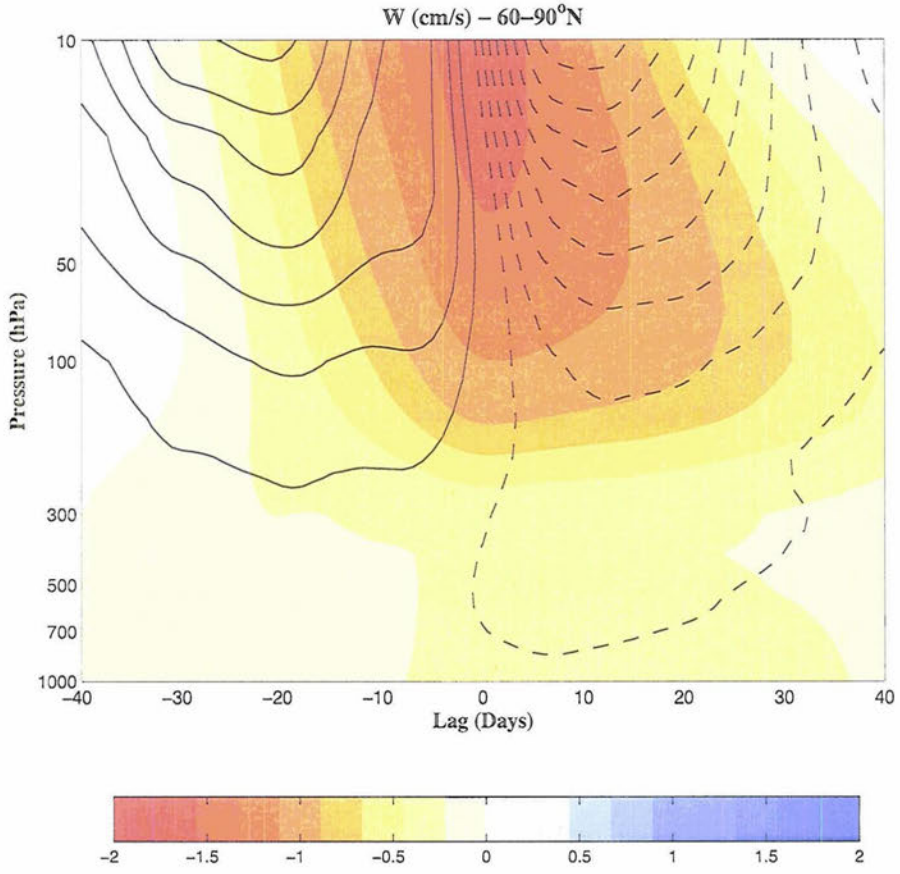

FIG. 3.7. *Shading*: Same as line contours in Fig. 3.1. *Contours*: Vertical velocity anomalies, averaged 60-90°N and regressed onto standardized and inverted JFM values of NAM_{10}. Contour interval 0.01 cm/s. Solid contours denote positive values; dashed contours negative. The zero contour is omitted. Colorbar denotes shaded contour values.

which estimates actual parcel movement) on driving the zonal-mean zonal wind, we must explicitly remove the adiabatic contributions to heating in (3.2).

3.3 Diagnostics in the TEM Framework

Along with the inability of $\overline{w}$ to solely represent diabatic motions (i.e., vertical motion resulting from diabatic heating or cooling of a parcel), the separation of the eddy fluxes in the EM QG zonal momentum equation and the EM QG thermodynamic equation unnecessarily complicates the roles of these fluxes in the stratosphere/troposphere system. In this section, we explore stratosphere/troposphere dynamical coupling in the context of the TEM governing equations in a similar fashion as with the EM equations. The key difference between the two frameworks is in the definition of the anomalous mean meridional circulation. This difference not only alters the interpretation of the results but also changes the forcing terms in the zonal momentum and thermodynamic equations. The anomalous mean meridional circulation in the TEM framework represents a quasi-Lagrangian point of view of the stratosphere/troposphere system (Holton 1997). Since diabatic motions are traditionally viewed as the "residual" to the EM adiabatic and eddy heat flux terms in (3.2), this transformed mean meridional circulation is traditionally named the residual mean meridional circulation (e.g., Holton 1992).

To derive the components of the residual mean meridional circulation, we first recognize that in the steady state, the EM adiabatic term is balanced by the eddy heat flux term and diabatic heating; i.e.,

$$N^2 HR^{-1}\overline{w} = -\frac{\partial\left(\overline{v'T'}\cos\varphi\right)}{a\cos\varphi\partial\varphi} + \overline{Q}\,. \tag{3.3}$$

Solving (3.3) for $\overline{w}$, we obtain an expression for the adiabatic and diabatic contributions to the vertical motion:

$$\overline{w} = \underbrace{-RH^{-1}\frac{\partial}{a\cos\varphi\partial\varphi}\left(\frac{\overline{v'T'}\cos\varphi}{N^2}\right)}_{\overline{w}_{adiabatic}} + \underbrace{\frac{RH^{-1}\overline{Q}}{N^2}}_{\overline{w}_{diabatic}}. \tag{3.4}$$

The last term on the RHS of (3.4) is considered the "residual mean vertical velocity" and is denoted $\overline{w}^*$. Hence, after rearrangement, (3.4) serves as a definition for $\overline{w}^*$:

$$\overline{w}^* = \overline{w} + RH^{-1}\frac{\partial}{a\cos\varphi\partial\varphi}\left(\frac{\overline{v'T'}\cos\varphi}{N^2}\right). \tag{3.5}$$

To derive the meridional component of the residual mean meridional circulation, we substitute (3.5) into the EM continuity equation and solve for the meridional wind. Hence, the residual mean meridional wind, denoted $\overline{v}^*$, represents the meridional motion necessary to conserve mass in the residual mean meridional circulation. $\overline{v}^*$ is explicitly defined as

$$\overline{v}^* = \overline{v} - \frac{R}{H\rho_o}\frac{\partial}{\partial z}\left(\frac{\rho_o\overline{v'T'}}{N^2}\right), \tag{3.6}$$

where z is the log-pressure coordinate.

3.3.1 The Zonal Momentum Equation

Using (3.6) to eliminate $\overline{v}$ from (3.1), the TEM QG zonal momentum equation is

$$\frac{\partial\overline{u}}{\partial t} = \left(\rho_0 a\cos\varphi\right)^{-1}\nabla\cdot\mathbb{F} + f\overline{v}^* + \overline{F}, \tag{3.7}$$

where ρ_0 is density and $\nabla \cdot \mathbf{F}$ is the divergence of the EP flux vector defined in (1.4). The introduction of the EP flux divergence into the TEM QG zonal momentum equation assists in directly examining how wave propagation impacts the zonal-mean circulation. Since EP flux vectors trace wave propagation and regions of EP flux convergence are related to regions of wave breaking (Edmon et al. 1980), plots of the EP flux divergence offer a visual representation of wave motions and their impact on zonal mean dynamics. For the purposes of the following discussion, $(\rho_0 a \cos\varphi)^{-1} \nabla \cdot \mathbf{F}$ will be referred to as the "EP flux divergence term" and $f\bar{v}^*$ as the "TEM Coriolis term."

Figure 3.8 is the same as Fig. 3.3 except for the terms in (3.7) (Fig. 3.8a is exactly the same as Fig. 3.3a but is repeated here for convenience). Fig. 3.8b shows that prior to day 0, the extratropical stratosphere is dominated by strong EP flux convergence, contributing substantially to the easterly acceleration of the zonal-mean zonal wind there. Before day -20, the troposphere experiences no substantial EP flux divergence or convergence, and hence the circulation is unaffected by the stratospheric forcing. However, after day -20, as the stratospheric EP flux convergence term grows in amplitude, a pocket of significant EP flux *divergence* resides in the upper troposphere. This region of divergence complements the strong stratospheric EP flux convergence during the same time. The pocket of EP flux divergence in the upper troposphere likely represents changes in the location of planetary wave breaking; i.e., waves that once could only propagate into the upper troposphere now can propagate further into the stratosphere.

The TEM Coriolis term (Fig. 3.8c) has opposite sign to and is weaker than the EP flux divergence term in the stratosphere. In the troposphere, however, the magnitudes are

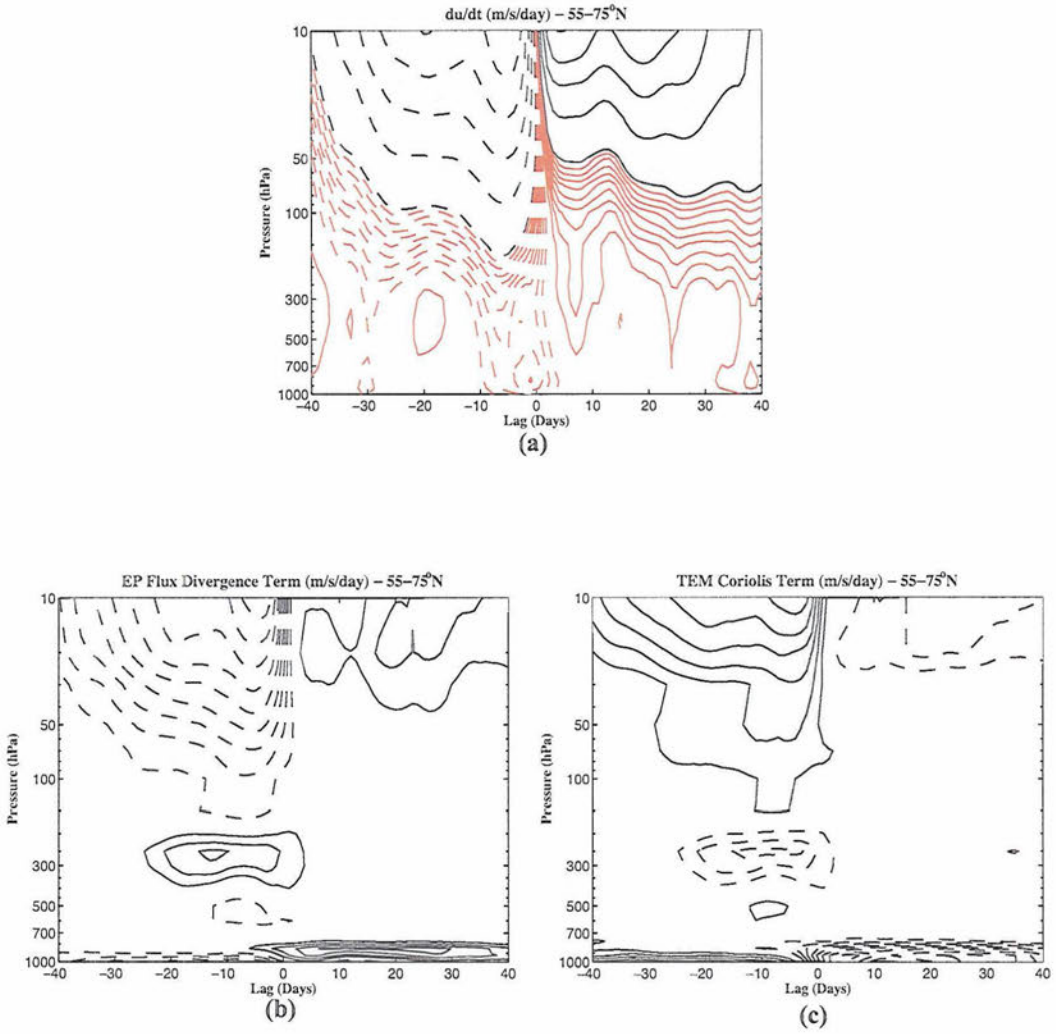

FIG. 3.8. (a) Same as Fig. 3.3a. (b) Same as (a), but contours are EP flux divergence term anomalies, averaged 55-75°N and regressed onto standardized and inverted JFM values of NAM_{10}. (c) Same as (a), but contours are TEM Coriolis term anomalies, averaged 55-75°N and regressed onto standardized and inverted JFM values of NAM_{10}. Contour interval in (b) and (c) 0.2 m/s/day. Solid contours denote positive values; dashed negative. The zero contour is omitted. Shading indicates corresponding correlations that exceed the 95% confidence interval. Refer to the text for definitions of terms.

fairly equal. Hence, while the EP flux divergence term dominates the tendency of the zonal-mean zonal wind in the stratosphere, the two terms are nearly balanced in the troposphere, analogous to the balance between the eddy momentum flux and EM Coriolis terms (Figs. 3.3b and 3.3c). Figure 3.9 shows more clearly the dominance of the EP flux divergence term over the TEM Coriolis term in the stratosphere and the near-cancellation of the two terms in the troposphere. Strong return flow at the base of the mean meridional cells is evident at the surface throughout the period (Fig. 3.8c), though the upper branch in the troposphere is indistinguishable.

Figure 3.10 shows the horizontal part of the EP flux divergence term $\left((\rho_0 a\cos\varphi)^{-1} \frac{\partial (F_\varphi \cos\varphi)}{a\cos\varphi\partial\varphi}; \text{ solid line} \right)$ and the vertical part of the EP flux divergence term $\left((\rho_0 a\cos\varphi)^{-1} \frac{\partial F_z}{\partial z}; \text{ dashed line} \right)$ along with $\partial\bar{u}/\partial t$ (red line) at 10, 100, and 300 hPa. The figure yields two main conclusions: (1) The vertical part of the EP flux divergence term (i.e., the vertical convergence of the meridional eddy heat flux) dominates $\partial\bar{u}/\partial t$ in the stratosphere; and (2) the largest acceleration of the zonal-mean zonal wind occurs when the EP flux is convergent both horizontally and vertically. Both of these conclusions agree with a similar study by O'Neill and Youngblut (1982). In the troposphere (i.e., 300 hPa; Fig. 3.10 bottom), the vertical part of the EP flux divergence term is larger than the meridional part, but $\partial\bar{u}/\partial t$ is nearly zero or weakly follows the meridional part of the EP flux divergence term, reiterating the importance of the eddy momentum flux in the tropospheric response.

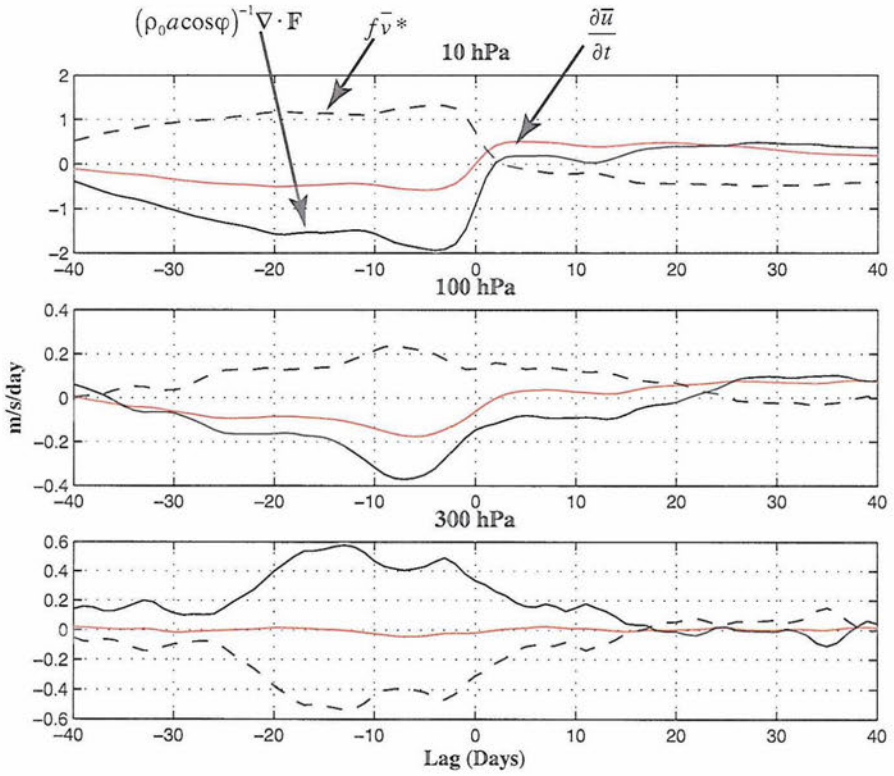

FIG. 3.9. Zonal-mean zonal wind tendency anomalies (red), EP flux divergence term anomalies (solid black) and TEM Coriolis term anomalies (dashed black), each averaged 55-75°N and regressed onto standardized and inverted JFM values of NAM_{10}, at three pressure levels: 10 hPa (top), 100 hPa (middle), and 300 hPa (bottom). Units are m/s/day.

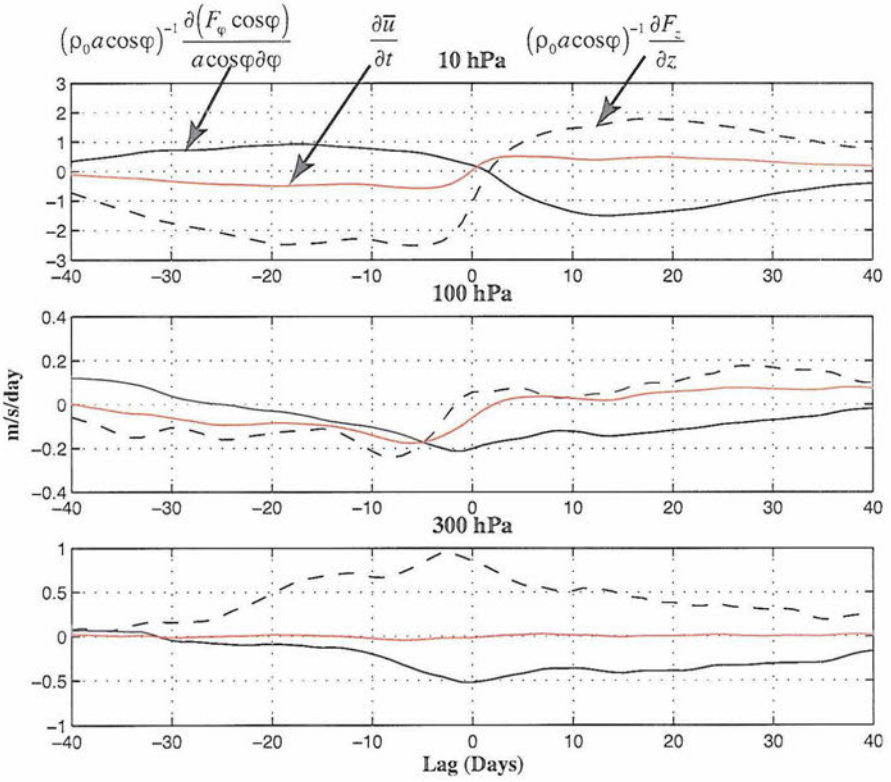

FIG. 3.10. Zonal-mean zonal wind tendency anomalies (red), anomalies of the meridional component of the EP flux divergence term (solid black), and anomalies of the vertical component of the EP flux divergence term (dashed black), each averaged 55-75°N and regressed onto standardized and inverted JFM values of NAM_{10}, at three pressure levels: 10 hPa (top), 100 hPa (middle), and 300 hPa (bottom). Units are m/s/day.

3.3.2 The Thermodynamic Equation

The TEM QG thermodynamic equation is obtained through substitution of (3.5) into (3.2):

$$\frac{\partial \overline{T}}{\partial t} = -N^2 HR^{-1}\overline{w}^* + \overline{Q}. \tag{3.8}$$

Figure 3.11 shows the observed temperature tendency (Fig. 3.11a; same as Fig. 3.4a) the first term on the RHS of (3.8) (named the TEM adiabatic term for purposes of this discussion; Fig. 3.11b), and $\overline{Q}$ (Fig. 3.11c), which is found through simple subtraction of the other two terms. Notice that the TEM adiabatic term is the same sign as the observed $\partial\overline{T}/\partial t$ anomalies, illustrating that parcels descend during the warming and rise as the polar stratosphere cools. Also, Fig. 3.11b shows that the TEM adiabatic term is nearly twice as large as the observed changes in the zonal-mean temperature field. Compensation for the heating from the TEM adiabatic term comes from $\overline{Q}$ (Fig. 3.11c). As the polar stratosphere warms at negative lags, $\overline{Q}$ acts to damp the warming through radiative cooling. This radiative cooling continues past day 0 as well, where now $\overline{Q}$ and the TEM adiabatic term actually have the same sign for a few days and are of comparable magnitude. Hence, for this short time, both terms work in tandem to restore the stratosphere to its equilibrium state. However, at later times (days +30 and beyond), $\overline{Q}$ becomes positive, indicating radiative warming that competes with the continued cooling of the polar stratosphere. Similar relationships hold in the lower stratosphere but are not so defined in the upper troposphere (Fig. 3.12). In fact, during positive lags at 300 hPa, $\partial\overline{T}/\partial t$ anomalies tend to follow $\overline{Q}$.

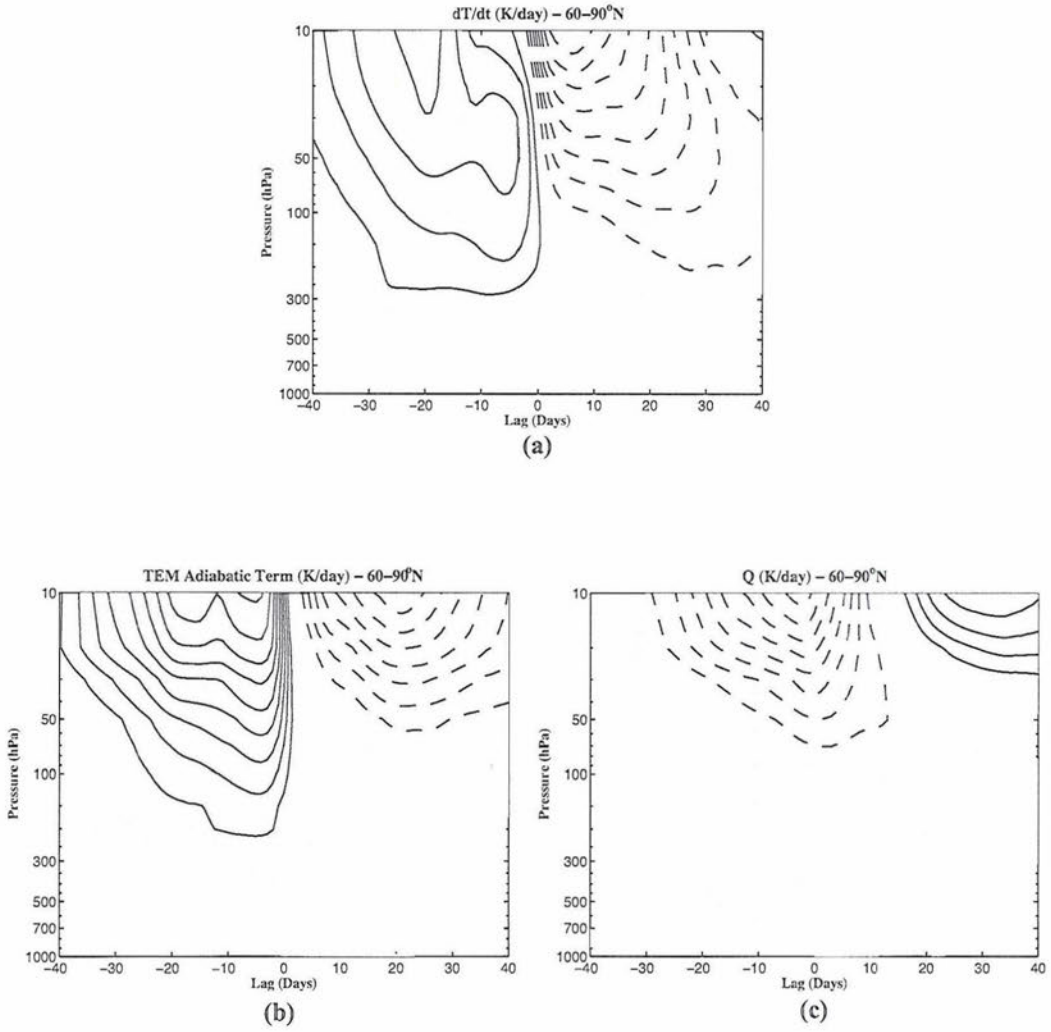

FIG. 3.11. (a) Same as Fig. 3.5a. (b) Same as (a), but contours are TEM adiabatic term anomalies averaged 60-90°N and regressed onto standardized and inverted JFM values of NAM_{10}. (c) Same as (a), but contours are anomalies of Q averaged 60-90°N and regressed onto standardized and inverted JFM values of NAM_{10}. Contour interval 0.05 K/day. Solid contours denote positive values; dashed negative. The zero contour is omitted. Shading indicates corresponding correlations that exceed the 95% confidence interval. Refer to the text for definition of terms.

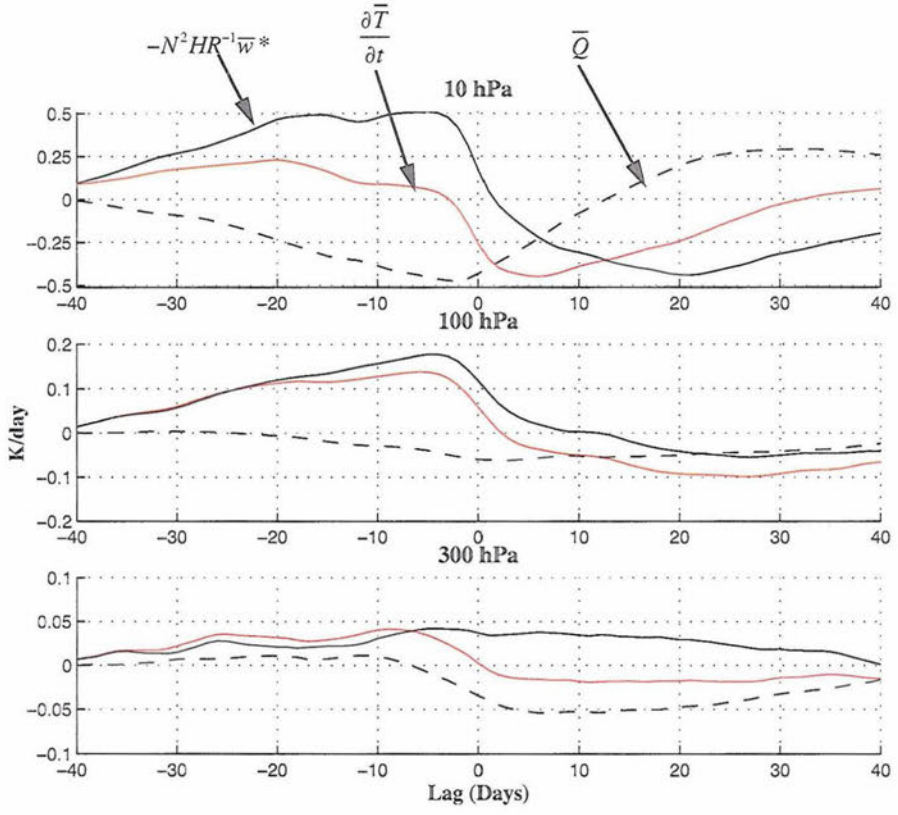

FIG. 3.12 Zonal-mean temperature tendency anomalies (red), TEM adiabatic term anomalies (solid black), and anomalies of Q (dashed black), each averaged 60-90°N and regressed onto standardized and inverted JFM values of $NAM_{10,}$ at three pressure levels: 10 hPa (top), 100 hPa (middle), and 300 hPa (bottom). Units are K/day.

To observe an estimate of the actual motion of air parcels, Figure 3.13 shows the regression of $\overline{w}^*$ onto standardized and inverted JFM values of NAM_{10}. Parcels that ascend and descend in the residual mean meridional circulation still undergo adiabatic heating and cooling via compression and expansion. The point of using $\overline{w}^*$, though, is to isolate the component of the vertical motion that follows parcel motion, which is not possible in the EM framework. $\overline{w}^*$ shows evidence of downward propagation into the upper troposphere, particularly at negative lags and when anomalies in the NAM descend to the surface (Fig. 3.1). At positive lags, the vertical branch to the residual mean meridional circulation appears to be confined nearly entirely to the stratosphere.

3.4 Summary

To summarize the results of the observations, we answer the precipitating questions at the start of this chapter.

(1) *To what extent are changes in the stratospheric circulation associated with anomalies in the circulation of the troposphere and lower stratosphere?*

Increasing wave drag in the stratosphere alters the zonal-mean circulation throughout the atmospheric column, especially shortly before day 0. Same-signed wind anomalies cross the tropopause at nearly the same time that the tropospheric NAM experiences same-signed anomalies as the stratospheric NAM (Fig. 3.1). The tropospheric circulation anomalies are induced below the level of maximum forcing by the anomalous mean meridional circulation depicted in Fig. 3.2. Changes in the

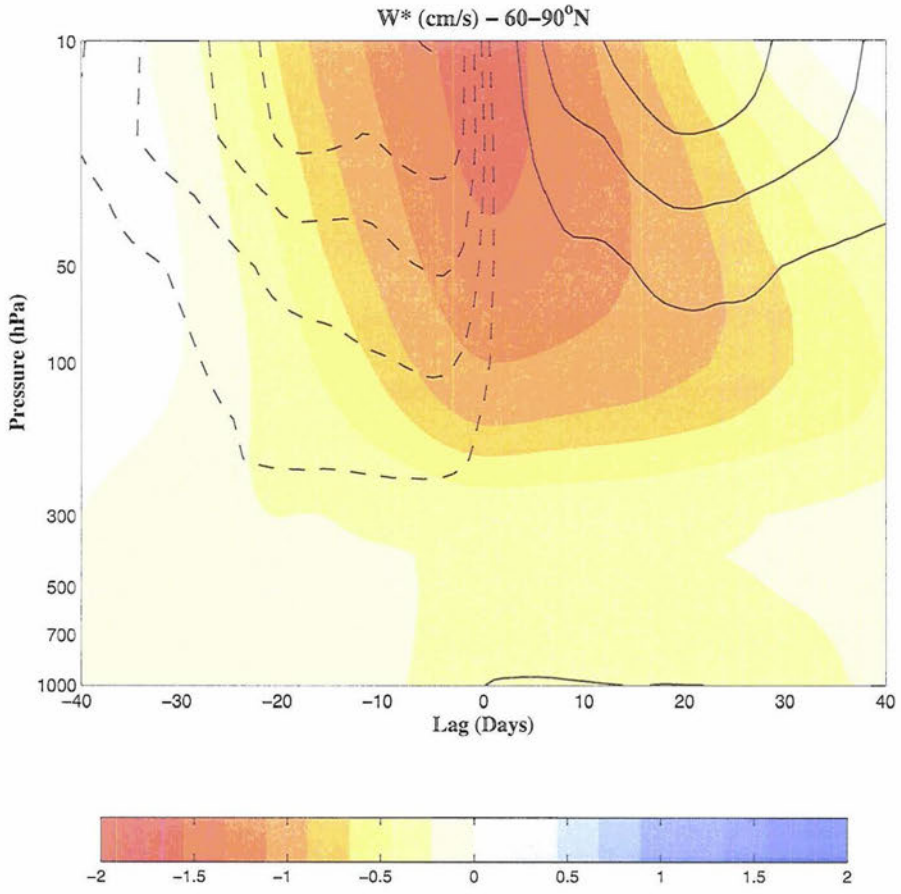

FIG. 3.13. Same as Fig. 3.7, but contours are residual vertical velocity anomalies, averaged 60-90°N and regressed onto standardized and inverted JFM values of NAM_{10}. Contour interval 0.01 cm/s. Solid contours denote positive values; dashed negative. The zero contour is omitted. Colorbar denotes shaded contour values.

stratospheric wave drag may also affect tropospheric eddy momentum fluxes, implied by the burst of horizontal momentum flux convergence in Fig. 3.3b.

(2) *Which terms in the QG zonal momentum equation and the QG thermodynamic equation dominate the observed tendencies in the zonal-mean zonal wind and temperature fields in the stratosphere? In the troposphere?*

In the EM framework, the EM Coriolis term drives the observed zonal-mean zonal wind tendency anomalies in the stratosphere, while in the TEM framework, the EP flux divergence term dominates. In the troposphere, both frameworks imply the effect of the Coriolis torque on the lower branch of the anomalous mean meridional circulation and the respective momentum forcing terms nearly balance, resulting in a small contribution to the tropospheric zonal-mean zonal wind. Thermodynamically, $\partial\overline{T}/\partial t$ anomalies track the eddy heat flux term in the EM framework. In the TEM framework, $\partial\overline{T}/\partial t$ anomalies follow the TEM adiabatic term throughout the stratosphere, but $\overline{Q}$ counters the stratospheric temperature anomalies related to the TEM adiabatic term and reduces the total response. In the troposphere, $\partial\overline{T}/\partial t$ weakly follows the TEM adiabatic term during negative lags, but then follows $\overline{Q}$ during positive lags.

(3) *How do physical interpretations of the resulting coupling differ between the EM and TEM frameworks?*

Here are a couple of major differences between the EM and TEM viewpoints.

(a) The primary difference between the two frameworks is the definition and workings of the anomalous mean meridional circulations in the balanced response. The anomalous mean meridional circulation in the EM framework represents a combined response to adiabatic and diabatic motions, masking actual movement of parcels. In the TEM framework, the anomalous mean meridional circulation physically represents the component of the circulation not balanced by eddy heat fluxes and thus estimates the actual movement of parcels. Hence, the TEM framework emphasizes the importance of diabatic heating in driving the zonal-mean circulation.

(b) (3.1) and (3.2) separate the effects of the eddy momentum and heat fluxes on the zonal-mean circulation, suggesting that both work separately to alter the circulation. Fig. 3.2 rebuts this notion and shows that both fluxes work together to influence the zonal-mean circulation. In the TEM framework, the definition of the residual mean meridional circulation allows us to incorporate the effect of the heat fluxes into the momentum equation via the EP flux. The EP flux divergence term easily allows us to explore the effects that anomalous wave propagation and wave breaking have on the zonal-mean circulation. Hence, the TEM framework offers more physical insight on wave dynamics and its role in driving the zonal-mean circulation.

CHAPTER 4

QUANTIFYING THE BALANCED RESPONSE OF THE ATMOSPHERE TO ANOMALOUS STRATOSPHERIC FORCING IN A SIMPLE NUMERICAL MODEL

In this chapter, we explore the instantaneous response of the stratosphere and troposphere to anomalous stratospheric momentum forcing, stratospheric heating, and friction (i.e., the balanced response) in a numerical model and compare the calculated tropospheric response to the observed response as shown in ERA-40. As described in Chapters 1 and 3, the balanced response is associated with an anomalous mean meridional circulation induced by anomalous forcing that works to redistribute momentum and heat throughout the atmospheric column.

Previous studies examined the contribution of the balanced response to observed tropospheric circulation anomalies. Song and Robinson (2004) calculated that for a unit of anomalous stratospheric wave drag, the near-surface zonal-mean zonal wind anomaly associated with the balanced response to the wave drag is ~0.5 m/s, approximately ten times smaller than the observed anomaly reported in Hartmann et al. (2000). Consequently, Song and Robinson (2004) concluded that the balanced response of the atmosphere to stratospheric wave drag inadequately explains the observed tropospheric response. The authors further argued that the remainder of the observed tropospheric

anomalies (~4.5 m/s) arises via tropospheric eddy feedbacks induced by stratospheric circulation anomalies.

However, Song and Robinson's conclusions hinge on observed anomalies from composites based on changes in the NAM time series at 1000 hPa (NAM_{1000}), which is dominated by internal tropospheric dynamics. An example of a tropospheric process that can affect NAM_{1000} is baroclinic eddy feedbacks on the tropospheric zonal winds (e.g., Robinson 2000; Lorenz and Hartmann 2003). If we instead use NAM_{10}, which describes fluctuations in the stratospheric circulation, as the basis for regressions or composites, then the near-surface zonal-mean zonal wind anomalies associated with stratospheric circulation changes are closer to 0.5 m/s, *not* 5 m/s (Figure 4.1). Therefore, assuming the validity of Song and Robinson's (2004) calculations, Fig. 4.1 implies that (1) the near-surface wind anomaly associated with the balanced response is relatively small; but more importantly, (2) the balanced response *can* sufficiently explain the observed tropospheric zonal wind anomalies.

The persistence of the circulation anomalies in the lower stratosphere and the troposphere for weeks following the incipient stratospheric wave drag anomalies may also be attributed to the balanced response. Figs. 4.1 and 4.2, the latter of which shows zonal-mean temperature anomalies averaged poleward of 60°N and regressed onto standardized and inverted JFM values of NAM_{10}, clearly illustrate this persistence. During positive lags, zonal-mean temperature anomalies quickly decay in the middle stratosphere as the polar vortex recovers, but in the lower stratosphere and upper troposphere, positive anomalies persist, coincident with persistent easterly zonal-mean zonal wind anomalies in the underlying troposphere (Fig. 4.1). The persistent zonal-

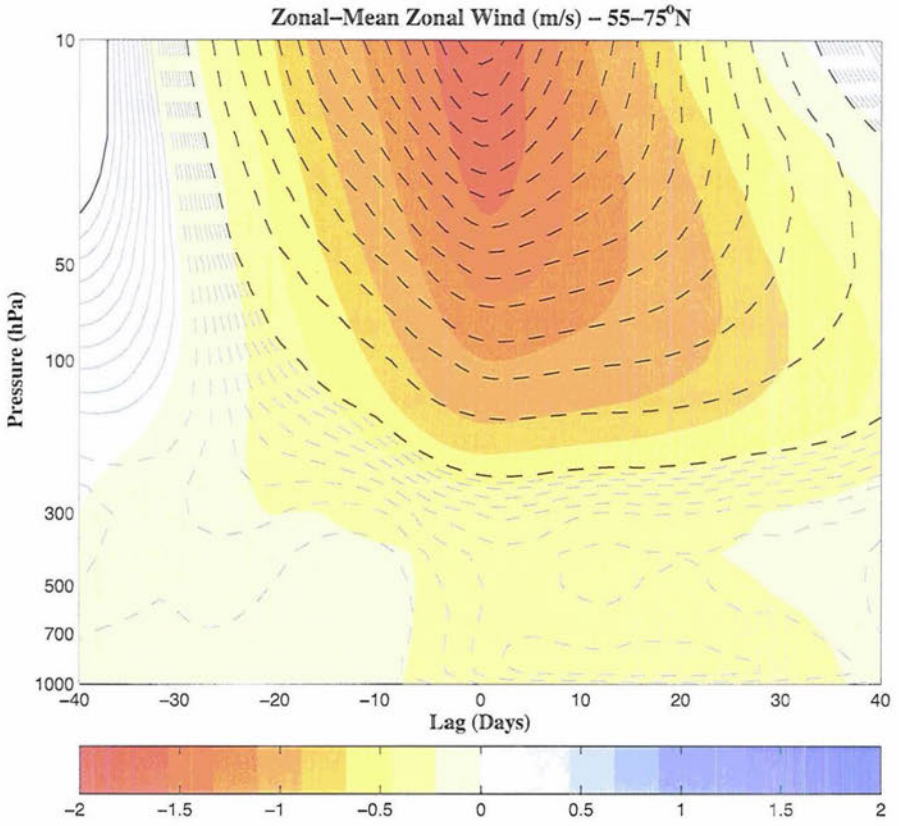

FIG. 4.1. *Shading:* Regression of the NAM time series, standardized for all calendar days, at each pressure level onto standardized and inverted JFM values of NAM_{10}. *Contours:* Zonal-mean zonal wind anomalies, averaged 55-75°N and regressed onto standardized and inverted JFM values of NAM_{10}. Black contour interval 1 m/s; 0.1 m/s for gray contours. Solid contours denote positive values; dashed negative. The zero contour is omitted. Colorbar denotes shaded contour values.

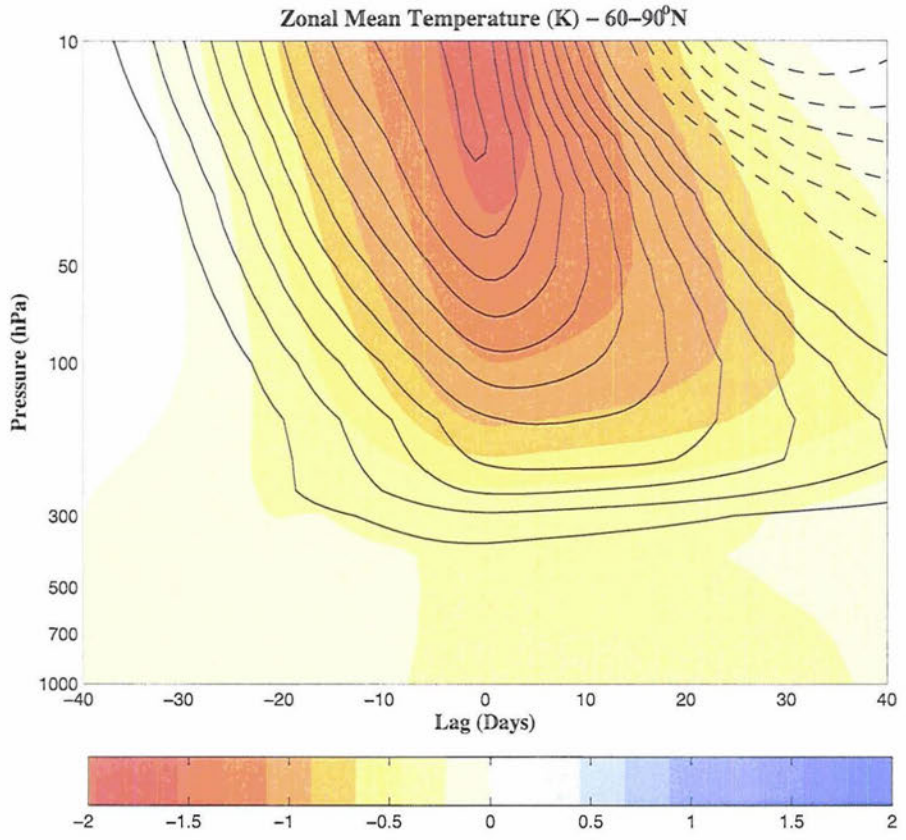

FIG. 4.2. *Shading:* Same as Fig. 4.1. *Contours:* Zonal-mean temperature anomalies, averaged 60-90°N and regressed onto standardized and inverted JFM values of NAM_{10}. Contour interval 0.5 K. Solid contours denote positive values; dashed negative. The zero contour is omitted. Colorbar denotes shaded contour values.

mean zonal wind and temperature anomalies appear related to each other, though Figs. 4.1 and 4.2 do not conclusively indicate why they would be.

In this chapter we quantify the effects of the balanced response using a simple two-dimensional (2-D) numerical model. We will argue that the balanced response explains the amplitude of the observed tropospheric anomalies, contrary to previous works. Additional results will provide a link between persistent lower stratospheric warm temperature anomalies and the persistence of the tropospheric zonal-mean zonal wind anomalies. All model results will be compared to observed zonal-mean zonal wind anomalies (linearly regressed onto standardized and inverted JFM values of NAM_{10}) to assess agreement. We also conduct a sensitivity study to determine whether the heating parameterization in the model impacts the conclusions drawn from the primary runs.

4.1 Hypotheses

Before we outline the numerical experiments, we summarize how tropospheric zonal-mean circulation anomalies related to stratospheric circulation anomalies evolve in the observations. Fig. 4.1 illustrates that the tropospheric zonal-mean zonal wind response to stratospheric anomalies can be divided into three phases:

- The preconditioning phase (days -30 to -15): During this phase, stratospheric zonal-mean zonal wind anomalies amplify in response to growing stratospheric wave drag (Fig. 3.8b), but the tropospheric zonal-mean zonal winds are virtually unchanged.

- The growth phase (days -10 to 0): During this ten-day period, tropospheric zonal-mean zonal wind anomalies intensify as the anomalous stratospheric wave drag reaches a maximum.
- The decay phase (days +5 to +30): This phase is marked with the decay of the tropospheric wind anomalies over a time scale much slower than the ~10 day tropospheric time scale (e.g., Feldstein 2000).

Next we examine a schematic of the balanced response to anomalous stratospheric wave drag and stratospheric radiative cooling (Figure 4.3). The figure demonstrates two important points about the balanced response: (1) The atmospheric response to anomalous stratospheric wave drag creates easterly anomalies at the level of maximum forcing and throughout the underlying atmospheric column (Fig. 4.3a); and (2) anomalous radiative cooling in the polar stratosphere induces westerly zonal-mean zonal wind anomalies above the level of heating, but easterly anomalies below the level of heating (Fig. 4.3b).

Based on Fig. 4.3 and the evolution of the tropospheric circulation anomalies, we test two specific hypotheses with our model.

(1) *The balanced response to anomalous stratospheric wave drag sufficiently accounts for the amplitude of the tropospheric response.* Apparent validation for this hypothesis exists when comparing Fig. 4.1 with the value of the near-surface zonal-mean zonal wind anomaly calculated by Song and Robinson (2004). In this chapter, we show that the calculated near-surface zonal-mean zonal wind anomaly associated with the balanced response agrees in amplitude with the observations.

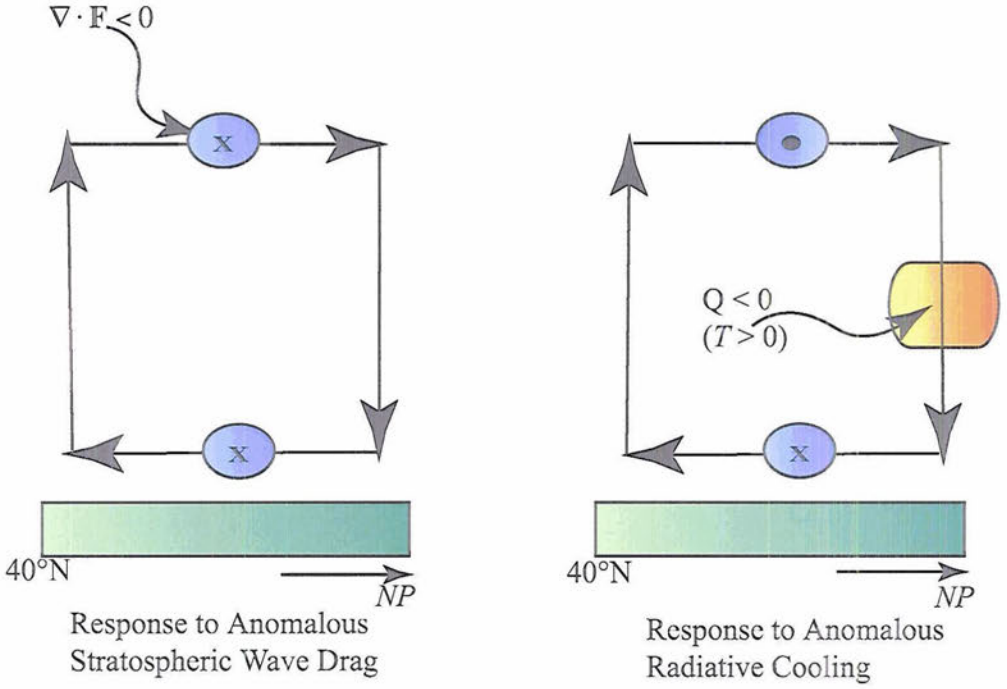

FIG. 4.3. (a) The balanced response to anomalous EP flux convergence in the NH extratropical atmosphere. Direction of the induced mean meridional circulation indicated by arrows. "x" denotes anomalous easterly acceleration; dot anomalous westerly acceleration. (b) Same as (a), except for the resulting balanced response to anomalous radiative cooling ($Q < 0$). Large red ellipse denotes warm temperature anomaly. In both figures, "NP" stands for "North Pole."

(2) *Persistent lower stratospheric radiative cooling during the decay phase maintains tropospheric circulation anomalies against frictional effects, slowing the decay rate of the anomalies.* This hypothesis addresses the issue of persistence of the tropospheric anomalies for weeks beyond the incipient stratospheric wave drag anomalies. Fig. 4.3b illustrates that lower stratospheric radiative cooling will induce easterly anomalies in the troposphere. Meanwhile, friction generates an anomalous mean meridional circulation that imposes westerly anomalies on the overlying tropospheric circulation and damps the easterly anomalies. Conceptually, the countering effects of the two anomalous mean meridional cells should slow the rate of decay of the tropospheric anomalies.

4.2 Model Description

4.2.1 Model Grid

The numerical model employed in this study is a 2-D (latitude and height) zonally-symmetric model with 300 grid points in the horizontal and 164 grid points in the vertical. The horizontal coordinate is $\mu = \sin\varphi$, where φ is latitude, while pressure (p) is used for the vertical coordinate. The domain is equally spaced in the horizontal coordinate and extends from -90° to 90°, while the vertical coordinate ranges from $p = 0$ to the surface of the model, $p_o = 1000$ hPa. There is no topography in the model. The vertical spacing is non-uniform and is described in more detail in the appendix. All model variables reside at grid points. This choice simplifies finite-differencing schemes in the model without sacrificing much numerical accuracy.

4.2.2 Governing Equations and Boundary Conditions

The system of equations for the model, linearized about a basic state of rest, is identical to that used in Haynes and Shepherd (1989). The general forms of the equations written in the TEM framework are listed below.

Momentum equation:
$$\frac{\partial \overline{u}}{\partial t} - f\overline{v}^* = \overline{G} + \overline{F}, \tag{4.1}$$

Thermal wind balance:
$$f\overline{u} = -\frac{\sqrt{1-\mu^2}}{a}\frac{\partial \overline{\Phi}}{\partial \mu}, \tag{4.2}$$

Hydrostatic equation:
$$\frac{\partial \overline{\Phi}}{\partial p} = -\rho^{-1} = -\frac{R\overline{T}}{p}, \tag{4.3}$$

Thermodynamic equation:
$$\frac{\partial \overline{T}}{\partial t} - \Gamma\overline{\omega}^* = \overline{Q}, \tag{4.4}$$

Continuity equation:
$$a^{-1}\frac{\partial}{\partial \mu}(\overline{v}^*\sqrt{1-\mu^2}) + \frac{\partial \overline{\omega}^*}{\partial p} = 0, \tag{4.5}$$

where $\overline{G} = \left(\rho_o a\sqrt{1-\mu^2}\right)^{-1}\nabla\cdot\mathbb{F}$, $\Gamma = -\frac{\overline{T}}{\overline{\theta}}\frac{\partial \overline{\theta}}{\partial p}$ is a measure of static stability, Φ is the geopotential, and all other variables have the same definitions as in Chapter 3.

Assuming $\overline{G}$, $\overline{F}$, Γ, and $\overline{Q}$ are known, (4.1) – (4.5) are a closed system of five equations with five unknowns ($\overline{u}$, $\overline{v}^*$, $\overline{\omega}^*$, $\overline{\Phi}$, and $\overline{T}$). One acceptable method of solution would be to eliminate four of the variables and condense the system to one equation with one unknown. Our study employs a slightly different method of solution, which is detailed in the appendix.

The resulting diagnostic equation to solve in the model (see the appendix) is a second-order elliptic partial differential equation. This equation can be solved

numerically provided proper boundary conditions are given. Lateral boundary conditions are set as

$$\bar{v}^* = 0 \text{ at } \mu = \pm 1, \tag{4.6}$$

i.e., there is no mass flux into or out of the poles. At the top of the model,

$$\bar{\omega}^* = 0 \text{ at } p = 0, \tag{4.7}$$

i.e., no mass crosses the top of the atmosphere. The lower boundary condition is written as

$$\frac{D\bar{\Phi}}{Dt} = 0 \text{ at } p = p_o, \tag{4.8}$$

where D/Dt is the Lagrangian derivative operator. Common practice approximates (4.8) by $\bar{\omega} = 0$, but Haynes and Shepherd (1989) argued using this approximation neglects any possible contribution from surface pressure changes to the zonal-mean circulation. Instead, the authors rewrote (4.8) as

$$\frac{\partial\bar{\Phi}}{\partial t} + \bar{\omega}\frac{\partial\Phi_o}{\partial p} = 0 \text{ at } p = p_o. \tag{4.9}$$

where Φ_o is the geopotential field of the basic state.

4.2.3 Prescribed Fields

Below we detail how the prescribed fields are calculated for input into the model. All prescribed fields except Γ are linearly regressed onto standardized and inverted JFM values of NAM_{10}. In this way, the calculated tropospheric response will be that which is linearly related to changes in the stratospheric circulation.

(a) ***Static Stability Parameter*** (Γ): In the model, Γ is calculated only for the basic state. In order to calculate Γ, we define a basic state vertical temperature profile similar to that of the 1976 United States Standard Atmosphere (NOAA, 1976). The lapse rate $\gamma(p)$ is defined as

$$\gamma(p) = 3.25\left[1 + \tanh\left(\frac{p-250}{25}\right)\right], \tag{4.10}$$

where p is in hPa. The lapse rate is close to 6.5 K/km from the surface up to 250 hPa. Above there, a small layer (50 hPa thick) exists where we transition to an isothermal atmosphere above 200 hPa. The temperature of the basic state depends only on pressure; hence, meridional temperature gradients do not exist in the basic state.

(b) ***Anomalous Stratospheric Wave Drag*** ($\overline{G}$)**:** Because we want to isolate the effects of only stratospheric wave drag on the tropospheric zonal-mean zonal winds, we set $\overline{G} = 0$ below 200 hPa. The vertical profile of $\overline{G}$ is also smoothed between 100-200 hPa to avoid discontinuities at the edge of the transition from nonzero wave drag to zero wave drag. Mathematically, the prescribed anomalous wave drag in the model is

$$\overline{G}(\mu,p) = \begin{cases} \left(\rho_0 a\sqrt{1-\mu^2}\right)^{-1}\nabla\cdot\mathbf{F} & 0 < p \le 100 \text{ hPa} \\ \tan\left(\frac{\pi}{4}\left(\frac{200-p}{100}\right)\right)\left(\rho_0 a\sqrt{1-\mu^2}\right)^{-1}\nabla\cdot\mathbf{F} & 100 \text{ hPa} \le p \le 200 \text{ hPa}. \\ 0 & p \ge 200 \text{ hPa} \end{cases} \tag{4.11}$$

(c) ***Anomalous Stratospheric Radiative Cooling*** ($\overline{Q}$)**:** In this numerical model, we approximate $\overline{Q}$ using the Newtonian cooling approximation. The Newtonian cooling

approximation assumes diabatic processes ($\overline{Q}$) are linear and physically representative of radiative cooling and heating (Andrews et al. 1987).

Because we are interested in effects from anomalous stratospheric $\overline{Q}$ only, anomalous tropospheric $\overline{Q}$ is set to zero. Fig. 4.2 shows coherent downward propagation of temperature anomalies through the stratosphere and into the upper troposphere (to ~350 hPa). The downward propagation of $\overline{Q}$ appears as well in Fig. 3.11c, though the values are small in the lower stratosphere likely due to a higher thermal damping timescale. Using Figs. 3.11c and 4.2 as guides, the anomalous radiative cooling profile in the model is prescribed as

$$\overline{Q}(\mu,p)=\begin{cases} -\alpha\overline{T} & 0 < p \le 250 \text{ hPa} \\ -\alpha\overline{T}\tan\left(\frac{\pi}{4}\left(\frac{350-p}{100}\right)\right) & 250 \text{ hPa} \le p \le 350 \text{ hPa}, \\ 0 & p \ge 350 \text{ hPa} \end{cases} \tag{4.12}$$

where α is the Newtonian cooling coefficient or thermal damping time scale (in day^{-1}).

Choosing the appropriate value of α is not straightforward because both radiative and photochemical processes affect its value. A number of studies (e.g., Dickinson 1968, 1973) empirically calculated α from available data, but these values were for the middle stratosphere and above. Limited studies have investigated α in the lower stratosphere or in the troposphere. Oftentimes, α is approximated by either a constant value throughout the atmosphere (e.g., Song and Robinson 2004) or a more varied structure to try to account for different constituents and their thermal properties in the atmosphere (e.g., Reichler et al. 2005). In this study, the profile for α is a modified version of that used in Reichler et al. (2005):

$$\alpha(p) = \begin{cases} k_{st} & 0 < p \le 95 \text{ hPa} \\ k_{st} + (k_a - k_{st})\left(\dfrac{p-95}{155}\right) & 95 \text{ hPa} \le p \le 250 \text{ hPa}, \\ k_a + (k_s - k_a)\max\left[0, \dfrac{p-700}{p_o - 700}\right] & 250 \text{ hPa} \le p \le p_o \end{cases} \tag{4.13}$$

where k_{st} = 1/(20 day), k_a = 1/(40 day), and k_s = 1/(4 day).

(d) ***Anomalous Frictional Effects*** ($\overline{F}$)**:** To parameterize the effects of friction, we use the following function:

$$\overline{F}(\mu, p) = -k_s \overline{u}_{sfc} \exp\left[\frac{p - p_o}{h}\right], \tag{4.14}$$

where $k_s = 1 \text{ day}^{-1}$ is the kinetic coefficient of friction, $\overline{u}_{sfc}$ is the surface (1000 hPa) zonal-mean zonal wind, and $h = 50$ hPa.

4.3 Idealized Stratospheric Wave Drag and Radiative Cooling Profiles

Before testing the model with observations, we conduct two test runs to ensure that the model produces physically consistent results with the balanced response. We construct ideal profiles for stratospheric wave drag ($\overline{G}$) and radiative cooling ($\overline{Q}$) and force the model with each profile separately. The idealized profiles are given by

$$\overline{G}(\varphi, p) = -\exp\left[-\left(\frac{\varphi - 65°}{20}\right)^2 - \left(\frac{p-10}{100}\right)^2\right] \text{ [m/s/day]}, \tag{4.15}$$

$$\overline{Q}(\varphi, p) = -\frac{1}{2}\exp\left[-\left(\frac{\varphi - 80°}{15}\right)^2 - \left(\frac{p-70}{100}\right)^2\right] \text{ [K/day]}, \tag{4.16}$$

where φ is in degrees and p is in hPa.

Figure 4.4 shows the resulting streamfunction (contours) when (4.15) (Fig. 4.4a) and (4.16) (Fig. 4.4b) are used in the numerical model. Positive values of the streamfunction indicate clockwise motion. Both figures show a clockwise meridional cell that is centered below and slightly equatorward of the maximum of each respective forcing. The direction of the streamfunction agrees with the schematics presented in Fig. 4.3, showing the model does in fact accurately capture the balanced response to anomalous stratospheric forcing.

4.4 Results

The objective of this section is to test and quantify the hypotheses put forth in Section 4.1. To accomplish this goal, we analyze the zonal-mean zonal wind anomalies in the stratosphere and troposphere during the growth and decay phases. The preconditioning phase is discussed separately. We will also show the individual contributions to the circulation anomalies from each prescribed term ($\overline{G}, \overline{Q}$, and $\overline{F}$) and, because the model is linear, then sum the individual contributions to receive the total response, which then can be compared to the observations.

4.4.1 Vertical Profiles of $\partial\bar{u}/\partial t$

All figures in this section show $\partial\bar{u}/\partial t$ averaged between 55-75°N and also time averaged during the respective phases (growth: days -10 to 0; decay: days +5 to +30).

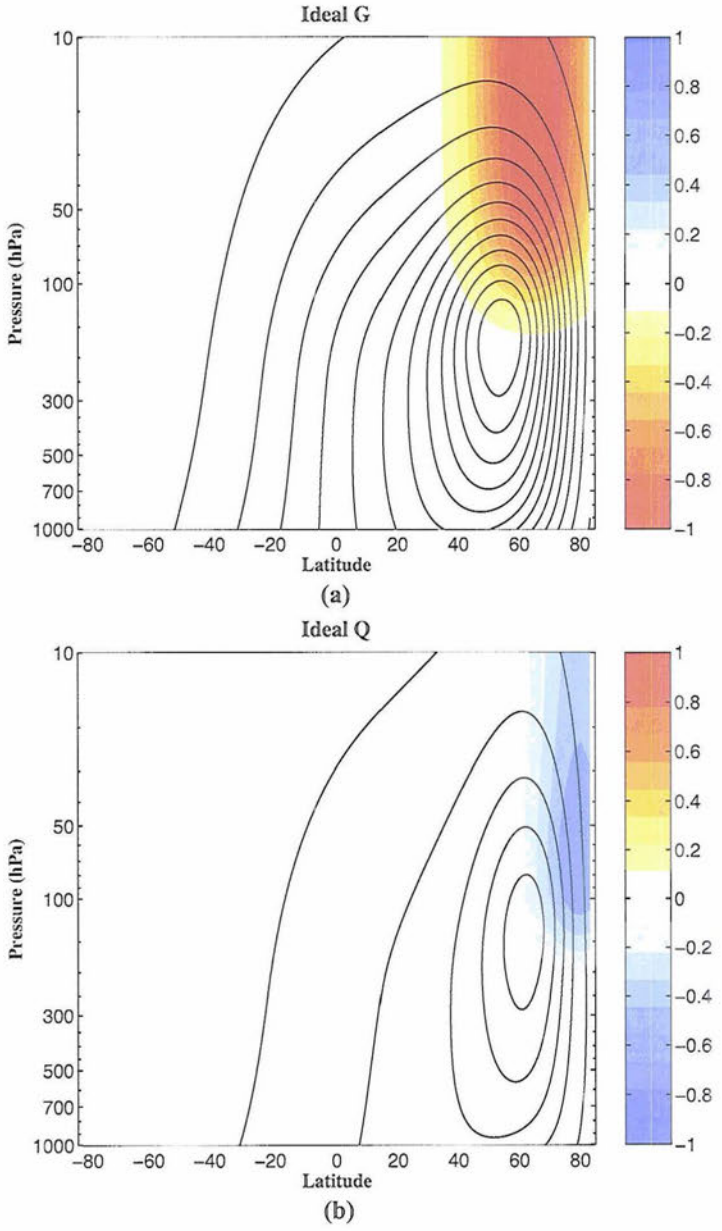

FIG. 4.4. (a) The streamfunction (contours) resulting from the idealized profile of G (m/s/day; shading). (b) Same as (a) except for the idealized profile of Q (K/day; shading). Contour interval 0.2 hPa m s^{-1}. Solid contours denote positive values (i.e., clockwise), starting at 0.2 hPa m s^{-1}. Colorbars denote shaded contour values. See text for definitions of idealized profiles.

The figures have four panels. The top panels show $\partial\bar{u}/\partial t$ from 10-1000 hPa, while the bottom panels highlight the troposphere (250-1000 hPa). Furthermore, the left panels of each figure show the contributions to $\partial\bar{u}/\partial t$ calculated with each prescribed term individually, and the right panels show the total response and the observed $\partial\bar{u}/\partial t$ during that phase.

During the growth phase (Figure 4.5), the simulated and observed $\partial\bar{u}/\partial t$ profiles show easterly acceleration throughout the middle stratosphere and the troposphere (Fig. 4.5 top right). In the stratosphere, the wave drag ($\overline{G}$; solid line) dominates the observed easterly acceleration there, while radiative cooling ($\overline{Q}$; dashed line) opposes the effects of $\overline{G}$ (Fig. 4.5 top left). In the troposphere, $\overline{G}$ dominates the tropospheric response, with added contributions from $\overline{Q}$, while $\overline{F}$ (dot-dashed line) barely impacts the tropospheric zonal-mean zonal wind (bottom left). The total easterly acceleration of the simulated zonal-mean zonal wind (black curve; bottom right) is actually slightly larger than the observed easterly acceleration (red line), not an order of magnitude smaller as suggested by earlier works. Hence, the model suggests that the balanced response can explain the amplitude of the tropospheric response to stratospheric anomalies. Moreover, the model also implies that $\overline{G}$ is responsible for most of the observed tropospheric anomalies during the growth phase.

As we transition to the decay phase (Figure 4.6), the zonal-mean zonal wind anomalies become more westerly with time in the middle and lower stratosphere as the polar stratosphere returns to the basic state (top right). Two physical processes are

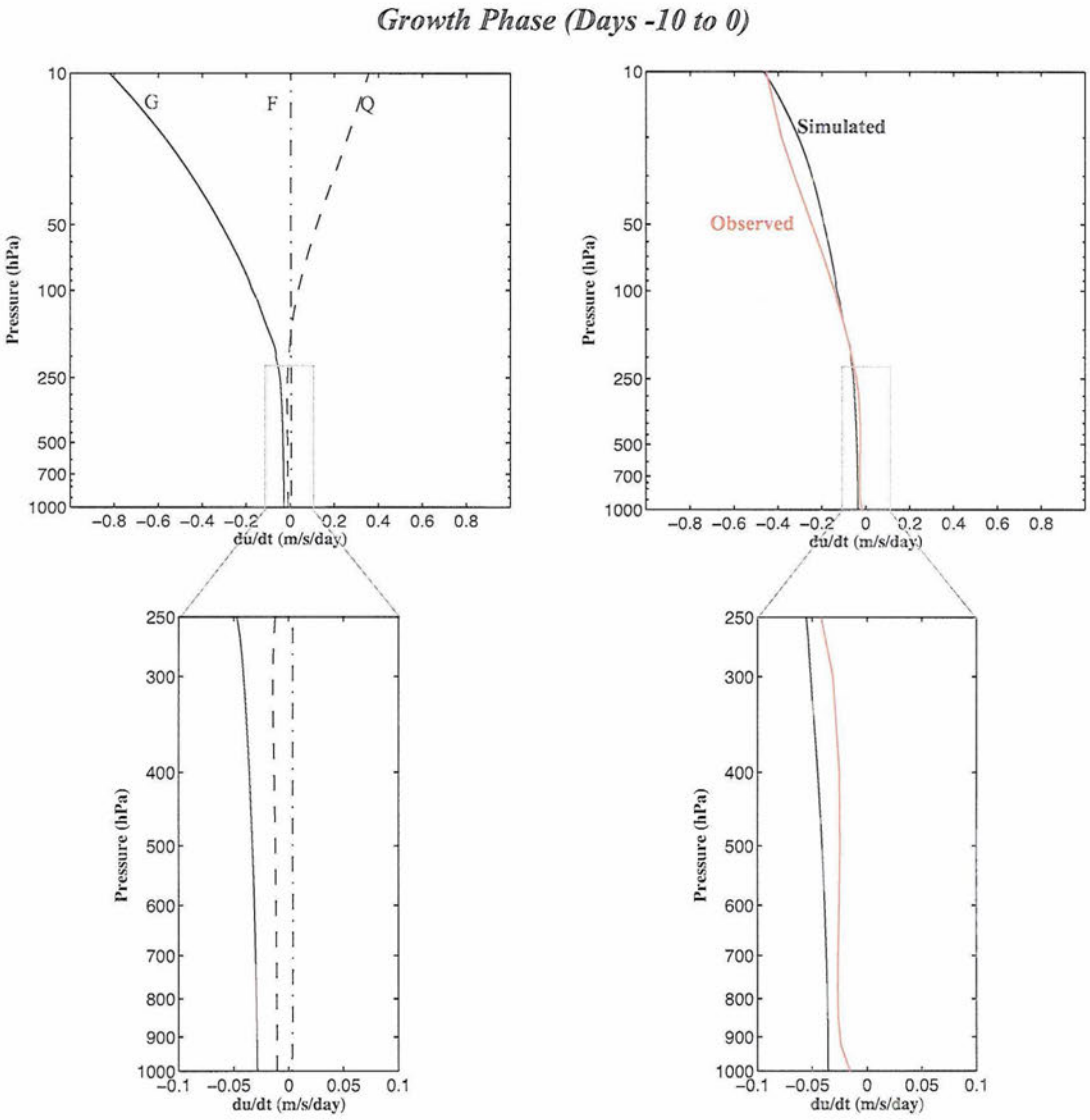

FIG. 4.5. *Left*: Vertical profiles of the model derived zonal-mean zonal wind tendencies, averaged 55-75°N and averaged over the growth phase (days -10 to 0). Solid lines denote the response to stratospheric wave driving, dashed lines the response to stratospheric radiative cooling, and dot-dashed lines the response to friction. *Right*: The sum of the model derived tendencies from the left panels (black) and the observed tendencies (red). Bottom panels highlight the tropospheric portion of the response. Units are m/s/day.

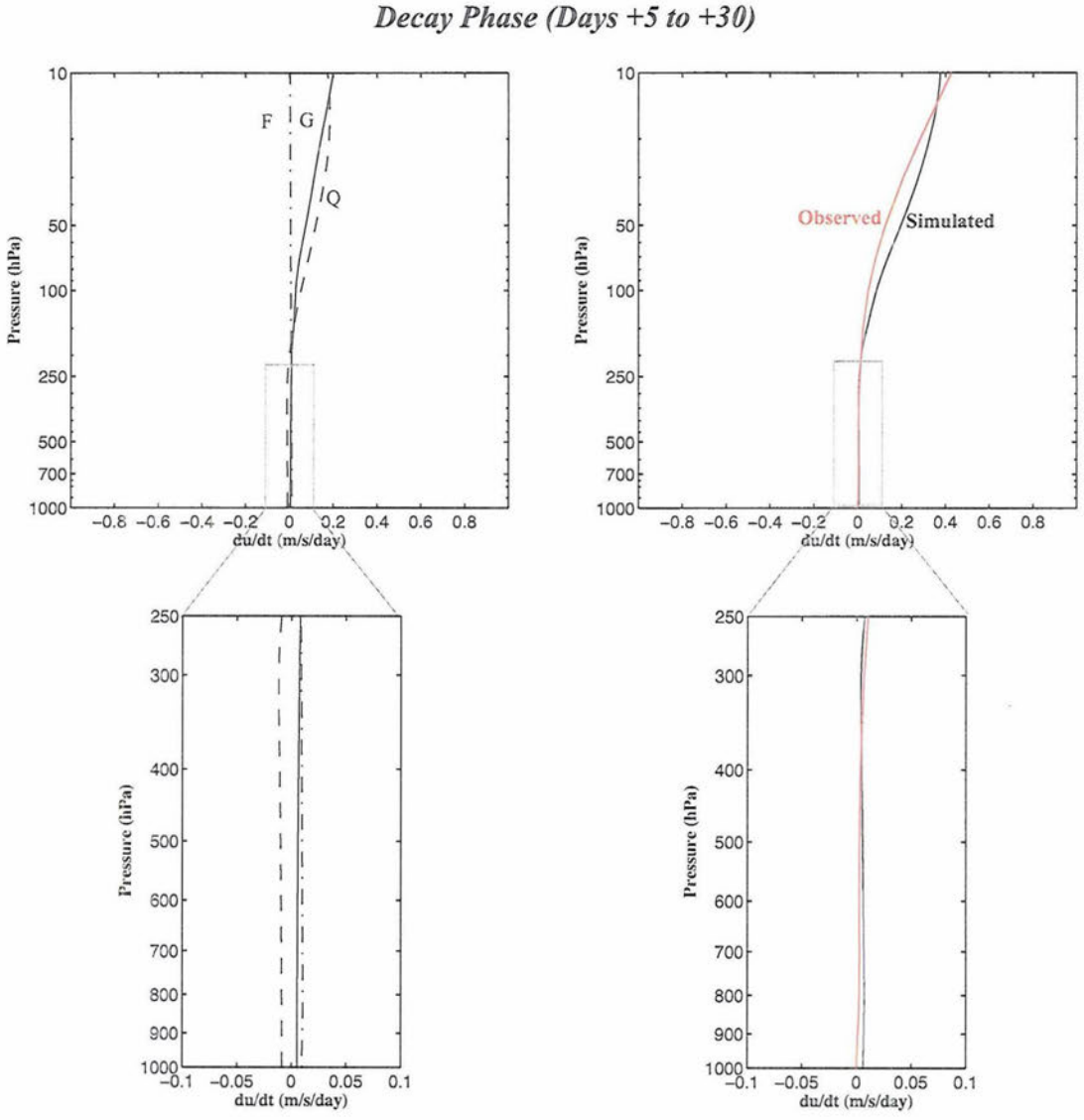

FIG. 4.6. As in Fig. 4.5, but for results averaged over the decay phase (days +5 to +30).

responsible for this recovery: (1) Waves are no longer breaking in the polar stratosphere, creating a weak area of EP flux divergence and hence local westerly acceleration of the zonal-mean zonal wind, and (2) the anomalous mean meridional circulation from the persistent positive temperature anomalies in the lowermost stratosphere drives westerly anomalies above. In the troposphere (Fig. 4.6 bottom), $\overline{F}$ generates westerly anomalies to damp the tropospheric easterlies, but those westerly anomalies are closely opposed by *easterly* anomalies still imposed by the anomalous mean meridional circulation driven by $\overline{Q}$ in the lower stratosphere. The cancellation of the anomalous westerlies induced by $\overline{F}$ and the easterlies induced by stratospheric $\overline{Q}$ results in little net change (mainly from $\overline{G}$) in the existing easterly anomalies in the troposphere. In other words, $\overline{Q}$ directly contributes to the persistence of the zonal-mean zonal wind anomalies in the troposphere by negating the effects of $\overline{F}$.

4.4.2 Tropospheric Zonal-Mean Zonal Wind Anomalies

Figure 4.7 shows the near-surface (925 hPa) zonal-mean zonal wind anomalies for days -10 to day +40. The anomalies are shown with respect to their value at day -10. Fig. 4.7a illustrates the zonal-mean zonal wind anomalies associated with each individual prescribed term in the model. The impacts of $\overline{Q}$ and $\overline{F}$ are near mirror images, with $\overline{Q}$ generating easterly anomalies on the near-surface flow and $\overline{F}$ generating westerly anomalies. $\overline{G}$ generates strong easterly acceleration until just after day 0, with westerly acceleration thereafter but at a slower rate than the westerly acceleration due to $\overline{F}$.

The total simulated response (black line; Fig. 4.7b) is remarkably similar to the observed zonal-mean zonal wind anomalies at 925 hPa (red line). The simulated

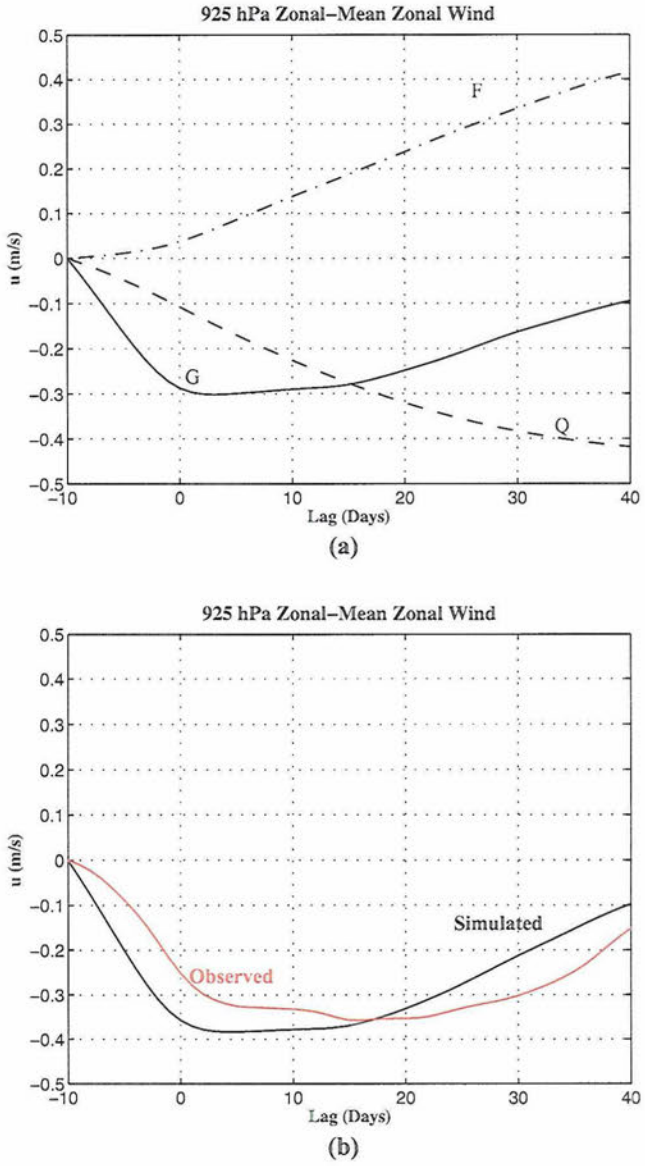

FIG. 4.7. (a) Zonal-mean zonal wind anomalies, averaged 55-75°N at 925 hPa, associated with the balanced response to G (solid), F (dot-dashed), and Q (dashed). (b) The total simulated response (black) and the corresponding observed zonal-mean zonal wind anomalies (red), averaged 55-75°N, at 925 hPa. All values are shown with respect to their value at day -10. Units are m/s.

anomalies are of the same amplitude as the observed anomalies, as seen in the vertical profiles. In fact, during the growth phase, the simulated zonal-mean zonal winds anomalies from the balanced response are *larger* in amplitude than the observations. The rate of decay of the tropospheric anomalies is faster in the calculations versus the observations. This quicker decay rate may be due to a number of factors including our parameterizations of $\overline{Q}$ and $\overline{F}$ or unresolved tropospheric dynamics in the model. Similar findings hold for the zonal-mean zonal wind anomalies at 500 hPa (Fig. 4.8), with even larger anomalies predicted by the model at this level versus the observations.

4.4.3 Comments on the Preconditioning Phase

The results shown so far reflect the growth and decay phases of the tropospheric zonal-mean zonal wind. Prior to day -10, while significant EP flux convergence grows in the stratosphere, observed tropospheric zonal-mean zonal wind anomalies do not respond as the balanced response suggests. The apparent shielding of the tropospheric flow from stratospheric influences ceases after ~day -15, when the troposphere suddenly experiences a growth of easterly anomalies. What conditions change between the preconditioning and the growth phases that eliminate the "shielding effect" (Shepherd and Shaw 2004) and promote growth of tropospheric anomalies?

One possible answer involves changes in meridional wave propagation in the troposphere between the preconditioning and growth phases. Figure 4.9 shows latitude-height plots of the EP flux divergence anomalies (divided by $\rho_o a$; contours) along with anomalous EP flux vectors, both regressed onto standardized and inverted JFM values of NAM_{10} and averaged over the preconditioning (Fig. 4.9a) and growth (Fig. 4.9b) phases.

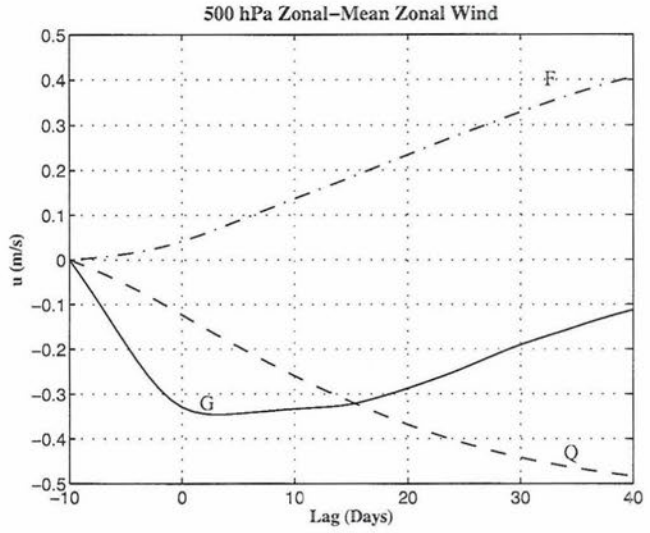

(a)

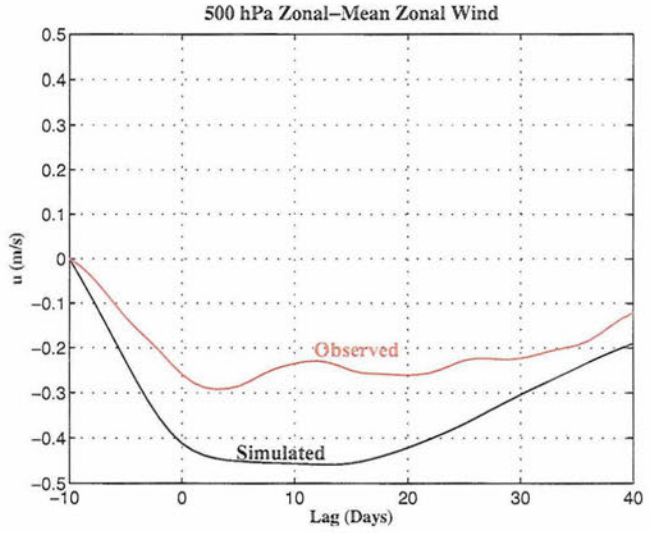

(b)

FIG. 4.8. As in Fig. 4.7, but for the zonal-mean zonal wind anomalies at 500 hPa.

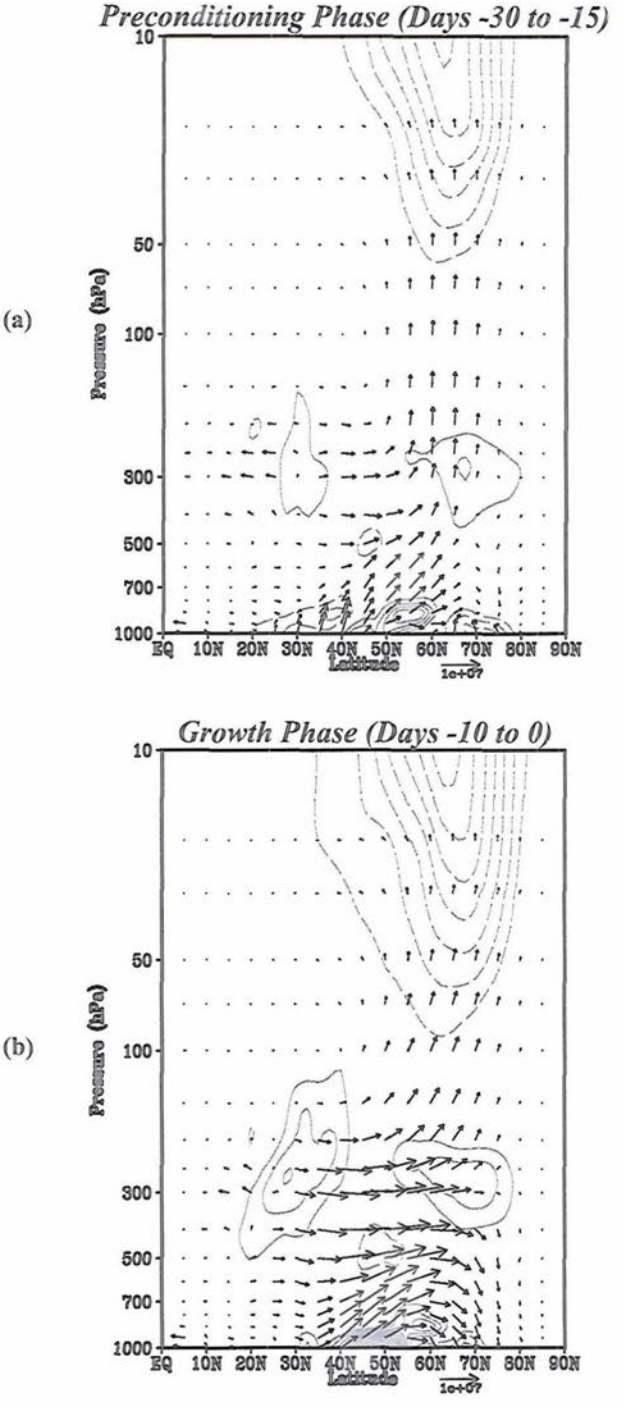

FIG. 4.9. (a) EP flux divergence (divided by $\rho_o a$; contours;) anomalies and anomalous EP fluxes (J/m^2; vectors), averaged over the preconditioning phase (days -30 to -15) and regressed onto standardized and inverted JFM values of NAM_{10}. (b) Same as (a) but averaged over the growth phase (days -10 to 0). Contour interval 0.1 m/s/day. Solid contours denote positive values; dashed negative. The zero contour is omitted.

During the preconditioning phase, vertical wave propagation dominates, introducing strong heating into the extratropical stratosphere. In the troposphere, relatively small meridional wave propagation anomalies exist in the troposphere; thus, since meridional wave propagation is associated with eddy momentum fluxes, small local changes in the tropospheric zonal-mean zonal winds occur. During the growth phase (Fig. 4.9b), strong vertical wave propagation remains in the high latitudes, but now the troposphere also exhibits strong anomalous poleward wave propagation. These wave propagation anomalies imply that westerly momentum is exported equatorward, or conversely that easterly momentum is transported poleward, generating easterly anomalies in the high latitude troposphere. However, the *net effect* on the tropospheric zonal-mean zonal wind at high latitudes is actually a local westerly anomaly, as suggested by the area of EP flux divergence there.

Fig. 4.9 suggests that anomalous poleward wave propagation is related to the sudden cessation of the tropospheric shielding and subsequent commencement of growing tropospheric circulation anomalies. By contrast, the model results suggest that stratospheric wave drag alone explains the tropospheric response during the growth phase. This dilemma likely arises because the prescribed wave drag in the model only includes the EP flux convergence in the stratosphere and neglects the compensating EP flux *divergence* in the upper troposphere, as shown in Figs. 3.8b and 4.9. By neglecting this area of EP flux divergence, we effectively neglect changes in tropospheric wave propagation in the model and thus cannot resolve any effects that those changes will have on the tropospheric circulation. Ignoring the tropospheric EP flux divergence also causes the simulated tropospheric easterly anomalies during the growth phase to be too large as

there is no compensating westerly forcing in the troposphere in the model. Attempts were made to include portions of the tropospheric wave drag into the model, but the results were inconclusive. Exploring tropospheric wave propagation changes and also why these changes occur is beyond the scope of this study and left for future work.

4.5 Sensitivity of the Results to the Value of the Newtonian Cooling Coefficient

The results presented in Section 4.4 demonstrate that the balanced response can explain the observed changes in the tropospheric zonal-mean zonal winds related to variability in the extratropical stratosphere. The relative simplicity of this numerical model and the approximations made in its formulation naturally raise questions about robustness of the model results. In this section we explore one of the parameterizations in the model - $\overline{Q}$ - and how changing the vertical profile of α affects the model results.

Three different profiles for α are chosen for comparison in this sensitivity study. The first profile is the one used throughout this study already (i.e., (4.13)). We will refer to (4.13) as the RPK-like profile. The other two profiles are constant with height - $\alpha(p) = 1/(20\text{ day})$ and $\alpha(p) = 1/(40\text{ day})$.

Figure 4.10 shows the 925 hPa zonal-mean zonal wind anomalies associated with each profile of α (Fig. 4.10a) only and the total (i.e., $\overline{G}+\overline{Q}+\overline{F}$) wind anomaly for each different α profile (black line), along with the observations (red line; Fig. 4.10b). The largest difference between the three profiles lies in the rate of westerly acceleration during the decay phase. The zonal-mean zonal wind anomalies associated with the RPK-like profile (solid line) are in between the anomalies generated by the other two profiles.

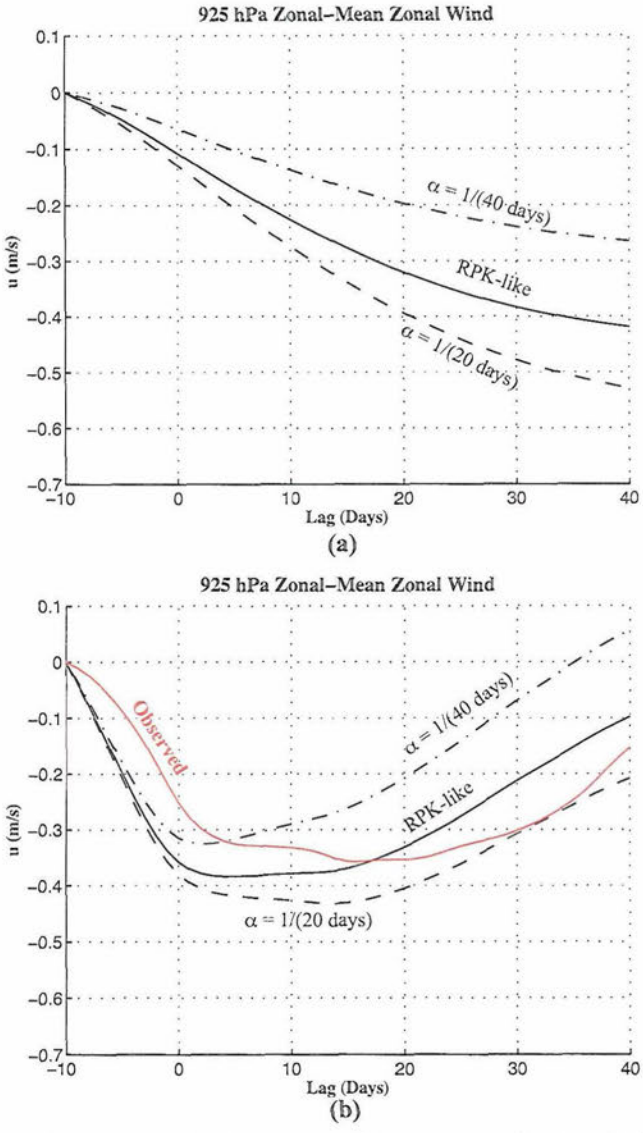

FIG. 4.10. (a) Zonal-mean zonal wind anomalies, averaged 55-75°N at 925 hPa, associated with the balanced response to Q for three different profiles of α: the profile defined in (4.13) (labeled RPK-like; solid line), $\alpha(p)$ = 1/(20 days) (dashed), and $\alpha(p)$ = 1/(40 days) (dot-dashed). (b) The total simulated response (G+Q+F) for each Q profile (RPK-like - solid black; $\alpha(p)$ = 1/(20 days) - dashed; $\alpha(p)$ = 1/(40 days) - dot-dashed) along with the observed anomalies (red), averaged 55-75°N, at 925 hPa. All values are shown with respect to their value at day -10. Units are m/s.

The tropospheric response to the $\alpha(p) = 1/(20\ \text{day})$ profile shows the greatest easterly acceleration during the growth phase and a slow decay rate of the total anomaly (dashed line; Fig. 4.10b). The easterly anomalies generated by the $\alpha(p) = 1/(40\ \text{day})$ profile during the growth phase are weak (dot-dashed line; Fig. 4.10a), leading to the most rapid elimination of the easterly anomalies during the decay phase (dot-dashed line; Fig. 4.10b). The same general results hold for middle and upper tropospheric zonal-mean zonal wind anomalies (not shown).

In conclusion, the prescribed profile for α primarily impacts the rate of decay of the tropospheric anomalies. The longer the thermal damping timescale in the lower stratosphere (i.e., the smaller α is), the smaller $\overline{Q}$ will be, thus inducing a weaker anomalous mean meridional circulation. This weaker circulation in turn does not generate strong enough easterly anomalies in the troposphere to counter the effects of friction, allowing the tropospheric easterly anomalies to damp quickly. However, the general structure of the calculated profiles in this sensitivity study still agrees with previous results and the underlying hypotheses.

4.6 Concluding Remarks

A simple numerical model of the balanced response supports the two hypotheses presented about the amplitude and evolution of the tropospheric zonal-mean circulation in response to stratospheric anomalies.

(1) Based on the numerical model results, the balanced response to anomalous stratospheric wave drag sufficiently accounts for the amplitude of the tropospheric response, contradicting conclusions drawn in previous works. Moreover, the results suggest that the balanced response creates anomalies that are greater than those observed, implying that other tropospheric processes may be at work to temper the anomalies associated with the balanced response. As highlighted in Section 4.4.3, neglecting the tropospheric component of $\overline{G}$ may result in an overestimation of the tropospheric response.

(2) Fig. 4.6 (bottom left) supports the hypothesis that persistent lower stratospheric heating counters frictional effects during the decay phase, resulting in a slower decay rate of tropospheric anomalies than that expected with friction alone. The figure shows nearly equal magnitude but opposite-signed contributions to the tropospheric response from $\overline{Q}$ and $\overline{F}$. The decay rate of the tropospheric zonal-mean zonal wind anomalies is sensitive to α, as shown in Section 4.5.

The results presented in this chapter do not specifically address the dynamics of the preconditioning phase, and the subsequent transition to the growth phase still lacks understanding. Moreover, the model does not resolve contributions from internal tropospheric dynamics to the tropospheric zonal-mean zonal winds. Nonetheless, the model isolates the balanced response as capable of explaining a large fraction of the observed tropospheric circulation anomalies induced by changes in the stratospheric circulation.

CHAPTER 5

CONCLUSIONS

5.1 Summary and Discussion

Variability in the extratropical stratosphere arises primarily through wave-mean flow interactions. Historically, the viewpoint on stratosphere/troposphere dynamical coupling involved the extratropical stratosphere merely responding to wave breaking from vertically propagating tropospheric waves with no feedback onto the troposphere. However, observational evidence in the late 1970s and again in the 1990s challenged this idea and suggested that changes in the tropospheric circulation are related to anomalous stratospheric flow generated by wave breaking. The balanced response of the atmosphere to stratospheric wave drag and heating describes qualitatively how the tropospheric circulation can respond to variability in the extratropical stratosphere, but previous studies discredited this explanation because of the relative small mass of the stratosphere compared to the troposphere. Hence, studies advocated other mechanisms such as tropospheric eddy feedbacks as necessary to explain the observed tropospheric response. This thesis offers evidence to the contrary; i.e., the balanced response alone can explain the amplitude of tropospheric circulation anomalies induced by stratospheric anomalies.

We examined the balanced response in two ways. The first way was by using observations to learn what dynamical relationships exist in the stratosphere/troposphere

system and what terms in the governing equations drive the observed circulation changes. Using NAM_{10} as the base index for the linear regression analyses allows for the results to be linearly related to fluctuations in the stratospheric circulation. This idea differs from previous works, which used, for example, NAM_{1000} as the base index for regressions and composites. The choice of NAM_{10} versus NAM_{1000} as the base index for observational analyses explains the difference in the conclusions reached in this thesis versus, for example, Song and Robinson (2004).

In the EM framework, the EM Coriolis term dominates the zonal-mean zonal wind tendencies in the stratosphere (Figs. 3.3c and 3.4), while mechanical forcing via the convergence of eddy momentum fluxes and the EM Coriolis term nearly balance in the troposphere, resulting in small changes in the tropospheric zonal-mean zonal wind. Though the EM QG zonal momentum equation and the EM QG thermodynamic equation ((3.1) and (3.2), respectively) separate the eddy momentum and heat fluxes between the two equations, the two fluxes work together to drive the zonal-mean zonal wind (see Fig. 3.2). Thermodynamically, zonal-mean temperature changes are driven by the eddy heat flux term in the EM framework (Fig. 3.5b), with substantial compensation from adiabatic cooling via vertical motions (Fig. 3.6).

The TEM framework incorporates the effects of the eddy heat and momentum fluxes on the zonal-mean circulation via the divergence of the EP flux. With the EP flux divergence term as an explicit forcing term in the TEM QG zonal momentum equation, we explored stratosphere/troposphere dynamical coupling in terms of wave breaking and its impacts on the zonal-mean circulation. The residual mean meridional circulation induced by wave breaking and diabatic heating physically represents the component of

the mean meridional circulation not balanced by the eddy heat fluxes, emphasizing the role of diabatic processes in the coupled system. In the TEM framework, stratospheric wave drag contributes substantially to the observed zonal-mean zonal wind tendencies in the stratosphere, and the heating associated with the rising and sinking of parcels in the residual mean meridional circulation (i.e., the TEM adiabatic term) drives the observed stratospheric temperature changes.

The second part of this thesis used a simple numerical model to quantify how much of the tropospheric response to extratropical stratospheric variability can be attributed to the balanced response. Prescribed forcings in the model included stratospheric wave drag, stratospheric radiative cooling (based on the Newtonian cooling approximation) and friction, all of which were regressed on standardized and inverted JFM values of NAM_{10}. In this way, the resulting anomalous zonal-mean zonal wind in the model represented the linear response to changes in the stratospheric circulation. The results clearly illustrated that the balanced response can sufficiently account for the amplitude of the observed tropospheric response during the growth (days -10 to 0) and decay phases (days +5 to +30). In fact, the simulated tropospheric response overestimated the observed response during the growth phase.

Additionally, we explored the observed persistence of tropospheric anomalies during the decay phase. The results suggested that persistent positive temperature anomalies in the lower stratosphere during the decay phase counter the effects of friction in the troposphere and maintain the tropospheric anomalies imposed during the growth phase. This result offers a new way of looking at the persistence of tropospheric anomalies and suggests a need to appropriately parameterize $\overline{Q}$ in modeling studies. The

latter point was well illustrated in the sensitivity study on the vertical profile of the Newtonian cooling coefficient (Section 4.5).

The numerical model results were not able to capture the observed tropospheric response during the preconditioning phase. The model did not resolve the apparent shielding of the troposphere to the effects of stratospheric wave drag during the preconditioning phase because no tropospheric component of wave drag was included in the prescribed field to counter the influence of the stratospheric wave drag. The shielding effect is explained further in Shepherd and Shaw (2004) who concluded that in the steady state, the downward influence of the mean meridional cell induced by the planetary wave drag extends to a certain level only when the vertical mass-weighted integral of $\nabla \cdot \mathbf{F}$ above that level is nonzero. In other words, the downward influence of planetary wave drag is only felt at a level through changes in vertical wave reflection and meridional propagation of planetary waves above that level (Shepherd and Shaw 2004). During the preconditioning phase, stratospheric levels experience easterly acceleration locally and remotely from the added wave energy into the region via enhanced vertical wave propagation (Fig. 4.9a). But, at levels in the middle and lower troposphere, essentially the same amount of wave energy exists in the overlying column (assuming the wave energy is conserved) since the anomalous wave activity is primarily vertical. Hence, the troposphere should experience little change in the zonal wind because of the shielding effect.

The overestimated simulated tropospheric anomalies during the growth phase may also result because of the lack of tropospheric wave drag in the model. Unlike the preconditioning phase, during the growth phase the troposphere contains both anomalous

vertical and poleward wave propagation. The anomalous poleward propagation in the troposphere physically represents waves that once moved equatorward but are now breaking in the high latitude troposphere and/or stratosphere. The change in meridional wave propagation likely arises because the weakened westerly flow in the stratosphere increases the QG index of refraction at high latitudes and provides a new channel of propagation for low and high wavenumber waves. Although the troposphere still contains a region of anomalous EP flux divergence (Fig. 4.9b), the addition of the anomalous poleward wave propagation weakens this region of divergence relative to the growth rate of the overlying stratospheric wave drag; i.e., the meridional part of the EP flux divergence is opposite-signed to the vertical component. Hence, in the upper troposphere, the net wave energy in the overlying column is no longer near zero, meaning the tropospheric zonal winds experience a net easterly acceleration from the downward influence of the stratospheric wave drag. Yet, because the model does not contain information about the tropospheric wave dynamics, the simulated response only accounts for the large stratospheric wave drag and thus overestimates the tropospheric response.

5.2 Avenues For Future Work

This thesis presents evidence that the balanced response adequately accounts for much of the response of the NH troposphere to extratropical stratospheric variability. Yet, more studies need to be done to determine how tropospheric eddy activity is impacted by stratospheric anomalies and how it contributes to the observed tropospheric anomalies. Do the effects of tropospheric wave activity in fact explain the remainder of

the difference between the observed and simulated circulations presented in Chapter 4? Also, how do the dynamics at work in NH stratosphere/troposphere coupling compare to those at work in analogous coupling in the SH? Are the same terms in the governing equations dominant in the NH also dominant in the SH stratosphere/troposphere system? The answer to these last two questions will gage how much about the future climate system in the NH we can derive by observing changes in the stratosphere/troposphere coupled system in the SH.

Below are ideas for future work to address the questions listed above.

(1) *Perform the same analyses (both in observations and with the numerical model) for the SH.* This thesis focused only on the NH primarily because the NH extratropical stratosphere exhibits the most intraseasonal variability. However, interest in the SH extratropical stratosphere heightened following the unprecedented SH SSW in 2002. Furthermore, because of the lack of significant land-sea contrasts, the Southern Annular Mode is more zonally-symmetric than its northern counterpart, meaning theories and assumptions about zonal-mean dynamics hold well in the SH extratropics. One slight complication with repeating the analysis for the SH will be data quality in the SH (which has improved mainly after 1979) and the relatively short SH active season (i.e., only November). These factors may lower the significance of the results derived for the SH stratosphere/troposphere system.

(2) *Conduct the same model experiments in the same model but impose a different basic state.* The model used in this study is a simple 2-D zonally-symmetric model with a

basic state at rest. Will the same results and conclusions be reached if the basic state has a nonzero background flow imposed? The basic state temperature profile could also be altered, for example, to reflect average NH winter conditions or a representative temperature profile in the SH. This change will impact the static stability in the model, changing the vertical motion and thus the vertical (and possibly horizontal) extent of the anomalous mean meridional circulations generated in the model.

(3) *Investigate why tropospheric-only model runs did not work.* As mentioned in Chapter 4, we conducted experiments using an entire atmospheric profile of wave drag and also with tropospheric-only components of the EP flux divergence term, but the results were inconclusive. One possible problem with these runs involves the complicated meridional pattern of the EP flux divergence term in the troposphere. Unlike the NH extratropical stratosphere, which shows a broad area of wave breaking during negative lags and then weak divergence during positive lags, the NH troposphere contains multiple regions of EP flux divergence and convergence in the meridional plane (e.g., Fig. 4.9). Imposing a finer horizontal grid in the model may resolve this dilemma.

(4) *Test the conclusions reached in this thesis in a more complex GCM.* The results obtained using the simple model in this thesis provide a great stepping stone for expansion and testing in a more complex GCM with more sophisticated parameterizations of $\overline{Q}$ and meridional temperature gradients to stimulate eddy growth. Some ideas to explore using GCM runs would be (a) to replicate the experiments done in this study and test the robustness of the results to other parameterizations of radiative

cooling and friction; (b) to evaluate the contribution of tropospheric eddy feedbacks to the observed tropospheric response; and (c) to examine the dynamics of the preconditioning phase and the "shielding effect."

The latter point ties into understanding the transition from the preconditioning to the growth phase and elucidating why a change from vertical to meridional wave propagation accompanies this transition. As mentioned earlier, one possible reason for the change in wave propagation is the change in the winds in the lower polar stratosphere, making that region more favorable for wave propagation. Using a GCM, we could produce a series of experiments with the same time-evolving vertical profile of wave drag but different prescribed vertical wind shears for the initial state of the model. The differences in the response in the troposphere among the runs would then be due to any changes that the vertical wind shear profile causes on tropospheric eddies.

References

Andrews, D. G., J. R. Holton, and C. B. Leovy, 1987: *Middle Atmosphere Dynamics.* International Geophysical Series. Vol. 40. Academic Press, 489 pp.

Baldwin, M. P., and T. J. Dunkerton, 1999: Propagation of the Arctic Oscillation from the stratosphere to the troposphere. *J. Geophys. Res.*, **104**, 30 937–30 946.

——, and ——, 2001: Stratospheric harbingers of anomalous weather regimes. *Science*, **294**, 581–584.

——, X. Cheng, and T. J. Dunkerton, 1994: Observed correlations between winter-mean tropospheric and stratospheric circulation anomalies. *Geophys. Res. Lett.*, **21**, 1141–1144.

——, D. B. Stephenson, D. W. J. Thompson, T. J. Dunkerton, A. J. Charlton, and A. O'Neill, 2002: Stratospheric memory and skill of extended-range weather forecasts. *Science,* **301**, 636 – 640.

Black, R. X., 2002: Stratospheric forcing of surface climate in the Arctic Oscillation. *J. Climate*, **15**, 268–277.

Boville, B. A., 1984: The influence of the polar night jet on the tropospheric circulation in a GCM. *J. Atmos. Sci.*, **41**, 1132–1142.

Boyd, J. P., 1976: The noninteraction of waves with the zonally averaged flow on a spherical Earth and the interrelationships of eddy fluxes of energy, heat and momentum. *J. Atmos. Sci.,* **33**, 2285–2291.

Bretherton, C. S., M. Widmann, V. P. Dymnikov, J. M. Wallace, and I. Bladé, 1999: The effective number of spatial degrees of freedom of a time-varying field. *J. Climate*, **12**, 1990–2009.

Charney, J. G., and P. G. Drazin, 1961: Propagation of planetary-scale disturbances from the lower into the upper atmosphere. *J. Geophys. Res.*, **66**, 83–109.

Chen, P., and W. A. Robinson, 1992: Propagation of planetary waves between the troposphere and the stratosphere. *J. Atmos. Sci.*, **49**, 2533–2544.

Dickinson, R. E., 1968: On the excitation and propagation of zonal winds in an atmosphere with Newtonian cooling. *J. Atmos. Sci.*, **25**, 269–279.

——, 1973: Method of parameterization of infrared cooling between altitudes of 30 and 70 kilometers. *J. Geophys. Res.*, **78**, 4451–4457.

Edmon, H. J., Jr., B. J. Hoskins, and M. E. McIntyre, 1980: Eliassen-Palm cross sections for the troposphere. *J. Atmos. Sci.*, **17**, 2600–2615.

Eliassen, A., 1951: Slow thermally or frictionally controlled meridional circulation in a circular vortex. *Astrophys. Norveg.*, **5**, 19–60.

——, and E. Palm, 1961: On the transfer of energy in stationary mountain waves. *Geofys. Publ.*, **22**, No. 3, 1 – 23.

Feldstein, S. B., 2000: The timescale, power spectra, and climate noise properties of teleconnection patterns. *J. Climate,* **13**, 4430 – 4440.

Fulton, S. R., P. E. Ciesielski, and W. H. Schubert, 1986: Multigrid methods for elliptic problems: A review. *Mon. Wea. Rev.*, **114**, 943–959.

Hartley, D. E., J. Villarin, R. X. Black, and C. A. Davis, 1998: A new perspective on the dynamical link between the stratosphere and troposphere. *Nature,* **391**, 471–474.

Hartmann, D. L., cited 2005: Chapter 3: Regression. [Available online at http://www.atmos.washington.edu/~dennis/552_Notes_ftp.html]

——, J. M. Wallace, V. Limpasuvan, D. W. J. Thompson, and J. R. Holton, 2000: Can ozone depletion and global warming interact to produce rapid climate change? *Proc. Natl. Acad. Sci.*, **97**, 1412–1417.

Haynes, P., and T. G. Shepherd, 1989: The importance of surface pressure changes in the response of the atmosphere to zonally-symmetric thermal and mechanical forcing. *Quart. J. Roy. Meteor. Soc.*, **115**, 1181–1208.

——, C. J. Marks, M. E. McIntyre, T. G. Shepherd, and K. P. Shine, 1991: On the "downward control" of extratropical diabatic circulations by eddy-induced mean zonal forces. *J. Atmos. Sci.*, **48**, 651–678.

Holton, J. R., 1992: *An Introduction to Dynamic Meteorology.* 3rd edition. Academic Press: 511 pp.

——, 1997: Zonally averaged flow. *The Stratosphere and Its Role in the Climate System.* G.P. Brasseur, Springer, 15–34.

——, and C. Mass, 1976: Stratospheric vacillation cycles. *J. Atmos. Sci.*, **33**, 2218–2225.

Hu, Y., and K. K. Tung, 2002: Interannual and decadal variations of planetary wave activity, stratospheric cooling, and Northern Hemisphere annular mode. *J. Climate*, **15**, 1659–1673.

Kushner, P. J., and L. M. Polvani, 2004: Stratosphere-troposphere coupling in a relatively simple AGCM: The role of eddies. *J. Climate,* **17**, 629–639.

Limpasuvan, V., D. W. J. Thompson, and D. L. Hartmann, 2004: The life cycle of the Northern Hemisphere sudden stratospheric warmings. *J. Climate*, **17**, 2584–2596.

Lorenz, D. J., and D. L. Hartmann, 2003: Eddy-zonal flow feedback in the Northern Hemisphere winter. *J. Climate*, **16**, 1212–1227.

Matsuno, T., 1971: A dynamical model of the stratospheric sudden warming. *J. Atmos. Sci.*, **28**, 1479–1494.

McIntyre, M. E., 1982: How well do we understand the dynamics of stratospheric warmings? *J. Meteor. Soc. Japan,* **60**, 37–65.

——, and T. N. Palmer, 1983: Breaking planetary waves in the stratosphere. *Nature*, **305**, 593–600.

NOAA, 1976. *U.S. Standard Atmosphere, 1976.* 227 pp.

O'Neill, A. and B. F. Taylor, 1979: A study of the major stratospheric warming of 1976/77. *Quart. J. Roy. Meteor. Soc.*, **105**, 71–92.

——, and C. E. Youngblut, 1982: Stratospheric warmings diagnosed using the transformed Eulerian-mean equations and the effect of the mean state on wave propagation. *J. Atmos. Sci.* **39**, 1370–1386.

Perlwitz, J., and H-F. Graf, 1995: The statistical connection between tropospheric and stratospheric circulation of the Northern Hemisphere in winter. *J. Climate*, **8**, 2281–2295.

——, and N. Harnik, 2003: Observational evidence of a stratospheric influence on the troposphere by planetary wave reflection. *J. Climate*, **16**, 3011 – 3026.

Polvani, L. M., and P. J. Kushner, 2002: Tropospheric response to stratospheric perturbations in a relatively simple general circulation model. *Geophys. Res. Lett.*, **29**, 17, doi:10.1029/2001GL014284.

Quiroz, R. S., 1977: The tropospheric-stratospheric polar vortex breakdown of January 1977. *Geophys. Res. Lett.*, **4**, 151–154.

——, 1979: Tropospheric-stratospheric interaction in the major warming even of January–February 1979. *Geophys. Res. Lett.*, **6**, 645–648.

Reichler, T., P. J. Kushner, and L. M. Polvani, 2005: The coupled stratosphere-troposphere response to impulsive forcing from the troposphere. *J. Atmos. Sci.*, in press.

Robinson, W. A., 2000: A baroclinic mechanism for the eddy feedback on the zonal index. *J. Atmos. Sci.*, **57**, 415–422.

Shepherd, T. G., and T. A. Shaw, 2004: The angular momentum constraint on climate sensitivity and downward influence in the middle atmosphere. *J. Atmos. Sci.*, **61**, 2899 – 2908.

Simmons, A. J., and J. K. Gibson, 2000: *ERA-40 Project Report Series No. 1: The ERA-40 Project Plan.* 61 pp.

Song, Y., and W. A. Robinson, 2004: Dynamical mechanisms for stratospheric influences on the troposphere. *J. Atmos. Sci.*, **61**, 1711–1725.

Thompson, D. W. J., and J. M. Wallace, 1998: The Arctic Oscillation signature in the wintertime geopotential height and temperature fields. *Geophys. Res. Lett.*, **25**, 1297–1300.

——, and ——, 2000: Annular modes in the extratropical circulation. Part I: Month-to-month variability. *J. Climate*, **13**, 1000–1016.

——, and S. Solomon, 2002: Interpretation of recent Southern Hemisphere climate change. *Science*, **296**, 895–899.

——, J. M. Wallace, and G. C. Hegerl, 2000: Annular modes in the extratropical circulation. Part II: Trends. *J. Climate*, **13**, 1018–1036.

——, M. Baldwin, and J. M. Wallace, 2002: Stratospheric connection to Northern Hemisphere wintertime weather: Implications for prediction. *J. Climate*, **15**, 1421–1428.

Wilks, D.S., 1995: *Statistical Methods in the Atmospheric Sciences.* Academic Press: 467 pp.

APPENDIX

MORE DETAILS ON THE NUMERICAL MODEL

In Chapter 4, the reader was presented with a brief description of the numerical model used in this study. In this appendix, many more details about the model, including the methods of grid spacing, finite differencing, and also analytic and numerical solutions of the system of equations, are covered. The intent of this appendix is to assist the reader in reconstructing the results presented in this study and perhaps even extending the model for other studies.

A.1 Vertical Grid Spacing

While the horizontal spacing (in $\mu = \sin\varphi$, where φ is latitude) is uniform, vertical grid spacing (in pressure (p)) is more complicated in the model. The initial concern with the vertical spacing is that we must have enough vertical levels to decently resolve the effects of friction near the surface, yet not have so many levels to make the numerical model computationally expensive. The solution is to design a vertical grid spacing scheme that has large spacing in the stratosphere, but the spacing progressively decreases towards the surface. This task can be accomplished by using a form of log-pressure coordinate spacing (D. A. Randall, personal communication).

Suppose we want to compute the spacing between levels l and l -1, where $p(l-1) < p(l)$. Let m represent the *layer* between l and l-1. Then, the spacing, η, between the two log-pressure levels is defined as

$$\eta(m) \equiv \ln\left(\frac{p(l)}{p(l-1)}\right). \tag{A.1}$$

To solve (A.1) iteratively, we must appropriately define $\eta(m)$ as a smooth function. $\eta(m) = \beta$, where β is a constant, is a solution, but equal spacing in log-pressure will not produce many layers in the lowermost troposphere, defeating our goal. Instead, $\eta(m)$ should be selected as a smooth function such that the function approaches a constant value (β) for small values of p but then approaches zero closer to the surface. One possible function is

$$\eta(m) = \beta\left[1 - \exp\left(\frac{p(l-1) - p_o}{h}\right)\right], \tag{A.2}$$

where h is the e-folding depth. Using (A.2) in (A.1) and rearranging we get

$$p(l) = p(l-1)\exp\left[\beta\left[1 - \exp\left(\frac{p(l-1) - p_o}{h}\right)\right]\right]. \tag{A.3}$$

For this study, we use $\beta = 0.1$ and $h = 750$ hPa.

Using (A.3) is a convenient iterative method of calculating pressure levels in the model, but there are two caveats. Since $p(l=1) = 0$, (A.3) cannot be used to compute $p(l=2)$ and subsequent levels. The user must arbitrarily choose $p(l=2)$ to start the iterative scheme. In this study, we choose $p(l=2) = 0.1$ hPa. Secondly, as we approach p_o in the iterative scheme, $\eta(m) \to 0$, generating infinitely many levels near the surface.

To avoid this problem, we terminate the iterative scheme once the distance between two consecutive pressure levels below 900 hPa is less than 1 hPa. The surface level is then prescribed directly: $p(l = lmax - 1) = p_o$, where $lmax$ = 164, the total number of vertical levels in the model.

A.2 Deriving the Diagnostic Equation Analytically

The model is constructed to solve five TEM QG governing equations, namely:

Momentum equation:
$$\frac{\partial \overline{u}}{\partial t} - f\overline{v}^* = \overline{G} + \overline{F}, \tag{A.4}$$

Thermal wind balance:
$$f\overline{u} = -\frac{\sqrt{1-\mu^2}}{a}\frac{\partial \overline{\Phi}}{\partial \mu}, \tag{A.5}$$

Hydrostatic equation:
$$\frac{\partial \overline{\Phi}}{\partial p} = -\rho^{-1} = -\frac{R\overline{T}}{p}, \tag{A.6}$$

Thermodynamic equation:
$$\frac{\partial \overline{T}}{\partial t} - \Gamma\overline{\omega}^* = \overline{Q}, \tag{A.7}$$

Continuity equation:
$$a^{-1}\frac{\partial}{\partial \mu}(\overline{v}^*\sqrt{1-\mu^2}) + \frac{\partial \overline{\omega}^*}{\partial p} = 0. \tag{A.8}$$

(See Chapter 4, Section 4.2.2 for the definitions of the variables.) Assuming $\overline{G}$, $\overline{F}$, Γ, and $\overline{Q}$ are known, (A.4) – (A.8) are a closed system of five equations with five unknowns ($\overline{u}$, $\overline{v}^*$, $\overline{\omega}^*$, $\overline{\Phi}$, and $\overline{T}$).

First, we eliminate $\overline{u}$, $\overline{\Phi}$, and $\overline{T}$ from (A.4) – (A.8). To do this, differentiate (A.5) with respect to p,

$$f\frac{\partial \overline{u}}{\partial p} = -\frac{\sqrt{1-\mu^2}}{a}\frac{\partial}{\partial \mu}\left(\frac{\partial \overline{\Phi}}{\partial p}\right), \tag{A.9}$$

and then substitute (A.6) into (A.9) to get

$$f\frac{\partial \overline{u}}{\partial p} = \frac{R\sqrt{1-\mu^2}}{ap}\frac{\partial \overline{T}}{\partial \mu}. \tag{A.10}$$

Next, differentiate (A.10) with respect to time,

$$f\frac{\partial}{\partial p}\left(\frac{\partial \overline{u}}{\partial t}\right) = \frac{R\sqrt{1-\mu^2}}{ap}\frac{\partial}{\partial \mu}\left(\frac{\partial \overline{T}}{\partial t}\right), \tag{A.11}$$

and then substitute (A.4) and (A.7) into (A.11) to yield

$$f\frac{\partial}{\partial p}\left(\overline{G}+\overline{F}+f\bar{v}^*\right) = \frac{R\sqrt{1-\mu^2}}{ap}\frac{\partial}{\partial \mu}\left(\overline{Q}+\Gamma\overline{\omega}^*\right). \tag{A.12}$$

(A.12) contains two unknowns, but only one equation. We can rectify this problem by defining $\bar{v}^*$ and $\overline{\omega}^*$ in terms of one other variable. Define the streamfunction, $\psi(\mu, p)$, as

$$\frac{\partial \psi}{\partial \mu} = -a\overline{\omega}^*, \tag{A.13}$$

$$\frac{\partial \psi}{\partial p} = \bar{v}^*\sqrt{1-\mu^2}. \tag{A.14}$$

Differentiate (A.13) with respect to μ and (A.14) with respect to p, and substitute into (A.12) to get

$$f\frac{\partial}{\partial p}\left(\overline{G}+\overline{F}\right)+\frac{f^2}{\sqrt{1-\mu^2}}\frac{\partial^2\psi}{\partial p^2} = \frac{R\sqrt{1-\mu^2}}{ap}\frac{\partial \overline{Q}}{\partial \mu} - \frac{R\Gamma\sqrt{1-\mu^2}}{a^2 p}\frac{\partial^2\psi}{\partial \mu^2}. \tag{A.15}$$

Multiplying through by the factor $p\sqrt{1-\mu^2}$ and rearranging to place all known terms on the RHS of the equation, the diagnostic equation for ψ becomes

$$f^2 p\frac{\partial^2\psi}{\partial p^2}+\frac{R\Gamma\left(1-\mu^2\right)}{a^2}\frac{\partial^2\psi}{\partial \mu^2} = \frac{R\left(1-\mu^2\right)}{a}\frac{\partial \overline{Q}}{\partial \mu} - fp\sqrt{1-\mu^2}\frac{\partial}{\partial p}\left(\overline{G}+\overline{F}\right). \tag{A.16}$$

A.3 Numerical Solution to the Differential Equation

A.3.1 Boundary Conditions

(A.16) is a second-order elliptic partial differential equation in ψ that can be solved numerically as long as proper boundary conditions are provided. Those boundary conditions are

$$\underline{\text{Lateral Boundary Conditions:}} \quad \bar{v}^* = 0 \Rightarrow \frac{\partial \psi}{\partial p} = 0 \text{ at } \mu = \pm 1, \tag{A.17}$$

$$\underline{\text{Top Boundary Condition:}} \quad \bar{\omega}^* = 0 \Rightarrow \frac{\partial \psi}{\partial \mu} = 0 \text{ at } p = 0, \tag{A.18}$$

$$\underline{\text{Lower Boundary Condition:}} \quad \frac{D\bar{\Phi}}{Dt} = 0 \Rightarrow \frac{\partial \bar{\Phi}}{\partial t} + \bar{\omega}\frac{\partial \Phi_o}{\partial p} = 0 \text{ at } p = p_o. \tag{A.19}$$

where Φ_o is the geopotential in the basic state. Note that $\bar{\omega}$, not $\bar{\omega}^*$, resides in (A.19).

To write (A.19) in terms of ψ, first substitute (A.6), evaluated in the basic state, into (A.19),

$$\frac{\partial \bar{\Phi}}{\partial t} - \rho_o^{-1}\bar{\omega} = 0 \text{ at } p = p_o, \tag{A.20}$$

then differentiate (A.20) with respect to μ,

$$\frac{\partial}{\partial t}\left(\frac{\partial \bar{\Phi}}{\partial \mu}\right) - \rho_o^{-1}\frac{\partial \bar{\omega}}{\partial \mu} = 0 \text{ at } p = p_o, \tag{A.21}$$

and then substitute (A.5) into (A.21) to yield

$$\frac{fa}{\sqrt{1-\mu^2}}\frac{\partial \bar{u}}{\partial t} + \rho_o^{-1}\frac{\partial \bar{\omega}}{\partial \mu} = 0 \text{ at } p = p_o. \tag{A.22}$$

Using (A.4) in (A.22), we get

$$\frac{fa}{\sqrt{1-\mu^2}}\left(f\bar{v}^* + \bar{G} + \bar{F}\right) + \rho_o^{-1}\frac{\partial \bar{\omega}}{\partial \mu} = 0 \text{ at } p = p_o. \tag{A.23}$$

Before making the substitution of the streamfunction into (A.23), we must change $\overline{\omega}$ to $\overline{\omega}^*$. To do so, we use Equation 3.4b from Edmon et al. (1980):

$$\overline{\omega}^* = \overline{\omega} + \frac{\partial}{a\partial\mu}\left(\frac{\overline{v'\theta'}\sqrt{1-\mu^2}}{\partial\overline{\theta}/\partial p}\right) \tag{A.24}$$

Now substitute (A.24), along with the definitions of ψ in (A.13) and (A.14), into (A.23) to make the boundary condition in terms of ψ alone:

$$\frac{fa}{\sqrt{1-\mu^2}}\left(\frac{f}{\sqrt{1-\mu^2}}\frac{\partial\psi}{\partial p}+\overline{G}+\overline{F}\right)-\left(a\rho_o\right)^{-1}\left[\frac{\partial^2\psi}{\partial\mu^2}+\frac{\partial^2}{\partial\mu^2}\left(\frac{\overline{v'\theta'}\sqrt{1-\mu^2}}{\partial\overline{\theta}/\partial p}\right)\right]=0 \text{ at } p=p_o. \tag{A.25}$$

We can simplify (A.25) in two ways. First, because the numerical model used in this study has no prescribed eddy momentum or heat fluxes at the surface, $\frac{\partial^2}{\partial\mu^2}\left(\frac{\overline{v'\theta'}\sqrt{1-\mu^2}}{\partial\overline{\theta}/\partial p}\right)=0$. Also, we can eliminate $\frac{\partial^2\psi}{\partial\mu^2}$ in (A.25) using (A.16). The final result, after some algebra and rearranging, is

$$f^2\frac{\partial\psi}{\partial p}+f\sqrt{1-\mu^2}\left(\overline{G}+\overline{F}\right)-\left(R\Gamma\rho_o\right)^{-1}\left(\Im-f^2p\frac{\partial^2\psi}{\partial p^2}\right)=0 \text{ at } p=p_o, \tag{A.26}$$

where $\Im$ is the RHS of (A.16).

A.3.2 Finite Differencing Schemes

(A.16) contains first- and second-order derivatives that we need to approximate numerically. In this study we use first-order centered differencing for second derivatives and second-order centered differencing for first derivatives.

Suppose we have a one-dimensional grid (e.g., along the x-axis) with a finite number of points, possibly non-uniformly spaced. Let j be an integer index for the points on the grid, increasing from left to right. Given an arbitrary smooth continuous function $f(x)$, the general form of the second-order centered finite-differenced form of the first derivative of $f(x)$ at the point x_j is

$$\left(\frac{df}{dx}\right)_j \approx b_{-1} f\left(x_{j-1}\right) + b_0 f\left(x_j\right) + b_1 f\left(x_{j+1}\right) \tag{A.27}$$

where

$$b_1 = -\frac{\left(x_{j-1} - x_j\right)}{\left(x_{j+1} - x_j\right)\left(x_{j+1} - x_{j-1}\right)} \tag{A.28}$$

$$b_{-1} = \frac{1 - b_1\left(x_{j+1} - x_j\right)}{x_{j-1} - x_j}, \tag{A.29}$$

$$b_0 = -\left(b_{-1} + b_1\right), \tag{A.30}$$

and $j-1$ and $j+1$ are the grid points directly to the left and right of x_j, respectively.

Similarly, the general form of the first-order centered finite-differenced form of the second derivative of $f(x)$ at x_j is

$$\left(\frac{d^2 f}{dx^2}\right)_j \approx c_{-1} f\left(x_{j-1}\right) + c_0 f\left(x_j\right) + c_1 f\left(x_{j+1}\right), \tag{A.31}$$

where

$$c_1 = \frac{2}{\left(x_{j+1} - x_j\right)\left(x_{j+1} - x_{j-1}\right)}, \tag{A.32}$$

$$c_{-1} = -\frac{c_1\left(x_{j+1} - x_j\right)}{x_{j-1} - x_j}, \tag{A.33}$$

$$c_0 = -(c_{-1} + c_1). \tag{A.34}$$

The second derivative is only calculated to first-order accuracy for computational simplicity. A second-order accurate scheme for the second derivative would involve using a four-point stencil and further complicate the finite-differenced form of the equations. In practice, using a first- or second-order spatial differencing scheme does not significantly alter the results, particularly when no time stepping is used.

A.3.3 Finite Differenced Forms of the Diagnostic Equation and Boundary Conditions and Method of Solution

Using the finite differencing schemes highlighted in the last section, we can rewrite (A.16) and (A.26) as

$$\begin{aligned} & f^2 p\left[c_{-1}\psi_{k,l-1} + c_0\psi_{k,l} + c_1\psi_{k,l+1}\right] + \frac{R\Gamma\left(1-\mu^2\right)}{a^2}\left[c^*_{-1}\psi_{k-1,l} + c^*_0\psi_{k,l} + c^*_1\psi_{k+1,l}\right] \\ & = \frac{R\left(1-\mu^2\right)}{a}\left[b^*_{-1}\overline{Q}_{k-1,l} + b^*_0\overline{Q}_{k,l} + b^*_1\overline{Q}_{k+1,l}\right] \\ & -fp\sqrt{1-\mu^2}\left[b_{-1}\left(\overline{G}_{k,l-1} + \overline{F}_{k,l-1}\right) + b_0\left(\overline{G}_{k,l} + \overline{F}_{k,l}\right) + b_1\left(\overline{G}_{k,l+1} + \overline{F}_{k,l+1}\right)\right] \\ & = \Xi \end{aligned} \quad , \tag{A.35}$$

$$\begin{aligned} & f^2\left[b_{-1}\psi_{k,l-1} + b_0\psi_{k,l} + b_1\psi_{k,l+1}\right] + f\sqrt{1-\mu^2}\left(\overline{G} + \overline{F}\right) \\ & -\left(\rho_o R\Gamma\right)^{-1}\left(\Xi - f^2 p\left[c_{-1}\psi_{k,l-1} + c_0\psi_{k,l} + c_1\psi_{k,l+1}\right]\right) = 0 \end{aligned} \quad \text{at } p = p_o, \tag{A.36}$$

where b, b^*, c, and c^* are the coefficients defined in (A.28) – (A.30) and (A.32) – (A.34) and subscripts k and l refer to index counters for the horizontal coordinate (increasing from south to north) and the vertical coordinate (increasing from the top of the model to the surface), respectively. The other two boundary conditions, (A.17) and (A.18), imply that at the poles, ψ is constant in the vertical, and likewise, at the top of the model, ψ is

also constant. In our study we simply set $\psi = 0$ at the poles (i.e., $k = 1$ and $k = kmax$, where $kmax = 300$, the number of grid points in the horizontal) and at $p(l = 1) = 0$.

An equation like (A.35) lends itself to numerical solution using the successive over-relaxation (SOR) routine. More specific details on the SOR routine can be found in Fulton et al. (1986)[2]. To increase the efficiency of the SOR routine, we can use the lower boundary condition to couple the surface to the nearest interior points (D. J. Lorenz, personal communication). Once a convergent solution for ψ is found using the SOR routine, the solutions can then be placed into finite-differenced forms of (A.13) and (A.14) to solve for $\overline{\omega}^*$ and $\overline{v}^*$, respectively. With those values, then we can use (A.4) and (A.7) to solve for the *tendencies* in $\overline{u}$ and $\overline{T}$. In the model, we do not use time stepping to solve explicitly for $\overline{u}$ and $\overline{T}$, as finite differencing in time introduces more complications to the numerical solution method. To obtain actual values for $\overline{u}$ on a particular day, for example, we simply integrate the instantaneous values of $\partial\overline{u}/\partial t$ from that day and all previous days.

---

[2] In this study, we use *Numerical Recipes in Fortran 77: Second Edition*, published by Cambridge University Press for numerical recipes of the SOR routine and also a tridiagonal solver. The entire book is available online at http://www.library.cornell.edu/nr/bookfpdf.html.